Near Infrared Photoelasticity of Polycrystalline Silicon and it's Relation to In-Plane Residual Stresses

A Thesis
Presented to
The Academic Faculty

by

Shijiang He

In Partial Fulfillment
of the Requirements for the Degree
Doctor of Philosophy

The George W. Woodruff School of Mechanical Engineering
Georgia Institute of Technology
December 2005

Near Infrared Photoelasticity of Polycrystalline Silicon and it's Relation to In-Plane Residual Stresses

Approved by:

Dr. Steven Danyluk
Advisor
School of Mechanical Engineering
Georgia Institute of Technology

Dr. I. Charles Ume
School of Mechanical Engineering
Georgia Institute of Technology

Dr. Jianmin Qu
School of Mechanical Engineering
Georgia Institute of Technology

Dr. Ajeet Rohatgi
School of Electrical and Computer Engineering
Georgia Institute of Technology

Dr. Sergei Ostapenko
University of South Florida

Dr. Shreyes N. Melkote
School of Mechanical Engineering
Georgia Institute of Technology

Date Approved August 05, 2005

This thesis is dedicated to

my mother Fengxiu Yu,

my wife Guoli Li

for their support in my study and research,

my son Kevin L. He

for his sweet smile.

ACKNOWLEDGEMENTS

First, I would like to express my sincere gratitude to my advisor, Prof. Steven Danyluk, of the Georgia Institute of Technology for all the support and guidance throughout this research.

I also wish to acknowledge Prof. Ajeet Rohatgi, Prof. Ajeet Rohatgi, Prof. Jianmin Qu, Prof. Shreyes Melkote and Prof. Charles Ume of Georgia Institute of Technology and Dr. Sergei Ostapenko of University of South Florida for serving as members of my thesis committee and for their helpful technical suggestions. I would like to thank Vijay Yelundur and Ajay Upadhyaya for processing the photovoltaic cells.

I would also like to thank my lab mates for their support and advice. Special thanks go to Inho Yoon for his help in preparing the silicon samples for the calibration, Fang Li for his help in the experiments.

I would like to thank J. Kalejs from RWE-Schott, J. Hanoka from Evergreen, M. Misra from BP Solar and Bayer for providing the wafers.

Finally I am greatly indebted to my mother, my wife, my brothers and many other family members for their endless encouragement, support and love.

TABLE OF CONTENTS

LIST OF TABLES

LIST OF FIGURES

LIST OF SYMBOLS

δ	photoelastic retardation
θ	isoclinic angle
I_m	background light intensity in phase-stepping
I_a	image contrast in phase-stepping
$\sigma_1, \sigma_2, \sigma_3$	principal stresses
$\sigma_x, \sigma_y, \sigma_z$	normal stresses along x, y and z respectively
$\tau_{yz}, \tau_{zx}, \tau_{xy}$	shear stress
n_1, n_2, n_3	principal refractive indices
n	the refractive index
n_0	stress-free refractive index
λ	illumination wavelength in the photoelasticity setup
t	effective thickness
h	beam height
M	moment of four-point bending
I	bending inertia
E	Young's modulus
τ	shear stress
τ_{max}	principal shear stress
$\boldsymbol{T}$	coordinate transformation matrix for rotation
$\boldsymbol{\beta}$	impermeability tensor
$\Delta\boldsymbol{\beta}$	the increment of the impermeability tensor

$\boldsymbol{x}$	cartesian coordinate
x_1, x_2, x_3	x, y and z axes of the cartesian coordinate
$\boldsymbol{x}'$	transformed cartesian coordinate
x_1', x_2', x_3'	x, y and z axes of the transformed cartesian coordinate
ϕ	angle of coordinate rotation
$\boldsymbol{B}$	coordinate transformation matrix
$\boldsymbol{\pi}$	fourth-rank piezo-optic coefficient tensor in (100) (010) and (001) coordinate
$\boldsymbol{\pi}'$	fourth-rank piezo-optic coefficient tensor in new coordinate
$\pi_{11}, \pi_{12}, \pi_{44}$	the elements of the piezo-optic tensor
β_i	elements of the impermeability tensor after the crystal is stressed $i = 1 \cdots 6$
C	isotropic stress-optic coefficient
$C(\theta)$	anisotropic stress-optic coefficient
$C_{(001)}$	stress-optic coefficient of (001) silicon
$C_{(011)}$	stress-optic coefficient of (011) silicon
$C_{(111)}$	stress-optic coefficient of (111) silicon
E_x, E_y	magnitude of the electrical field along x and y axes
δ_x, δ_y	phase of the electrical field
ω	electrical field frequency
$\boldsymbol{S}$	Stokes vector of a light beam
s_i	element of the Stoke vector, $i = 1 \cdots 4$
$\boldsymbol{S}_0$	Stokes vector of randomly polarized light
$\boldsymbol{S}_m$	Stokes vector of the background light
$\boldsymbol{P}(\beta)$	Mueller matrix of a polarizer
$\boldsymbol{M}(\theta, \delta)$	Mueller matrix of a retarder
$\Delta\delta$	error in the retardation
$\Delta\theta$	error in the isoclinic angle

SUMMARY

The goal of this research was to investigate an experimental infrared transmission technique and associated analysis tools that extract the in-plane residual stresses in thin single and poly-crystalline silicon sheet, and try to relate the residual stresses to physical parameters associated with silicon growth and cell processing.

Previous research has suggested this concept, but many engineering and analytical details had not been addressed. In this research, a system has been designed and built. A fringe multiplier was incorporated into the system to increase the sensitivity. The error was analyzed and the resolution of the system was found to be 1.2 MPa. To convert the experimental results to residual stresses, the stress-optic coefficients of (001), (011) and (111) silicon were analyzed analytically and calibrated using a four-point bending fixture. Anisotropy in (001) and (011) silicon was found to be 33%, and the coefficient of EFG silicon is 1.7 times larger than that of (001) silicon.

The polariscope together with other techniques was applied to silicon wafers after various processing steps in the manufacture of photovoltaic cells. The influence of the processing on residual stress was investigated and positive correlations between residual stresses, PL and efficiency were obtained.

CHAPTER I

BACKGROUND

1.1 Summary

The chapter summarizes the literature review of residual stress in thin plates. The measurement techniques for the residual stresses will be reviewed with a concentration on photoelasticity. The approach of this research on the residual stress measurement will also be presented.

1.2 Sources of Residual Stresses in Silicon

Single or polycrystalline crystal silicon is a semiconductor material grown from the melt into ingots by the Czochralski (CZ) method (Figure 1), or into thin sheets by the edge-defined film (EFG) (Figure 2) or string ribbon method (Figure 3). The silicon wafers or blanks are sectioned from the ingots by sawing or the silicon sheet by laser cutting. Microelectronic circuits or photovoltaic devices are fabricated on these substrates through various chemical, physical and thermal processes.

During the growth of EFG and string ribbon silicon, the temperature of the silicon melt is 1450°C, and it drops to room temperature within 0.5 m from the solid/melt interface, therefore, a high thermal gradient is unavoidable at the solid-melt interface. The distribution of the thermal gradient for string ribbon is shown in Figure 4. Significant curvature in the cooling profile is also unavoidable since the gradient must go to zero after the ribbon exists the furnace. This curvature will lead to appreciable thermal stresses. When the thermal stress exceeds the elastic limit at elevated temperature (600°C), thermal plastic deformation occurs [3]. The stresses associated with the plasticity cannot be removed completely by post-growth annealing [4], the remaining part is frozen in the silicon in the form of residual stress.

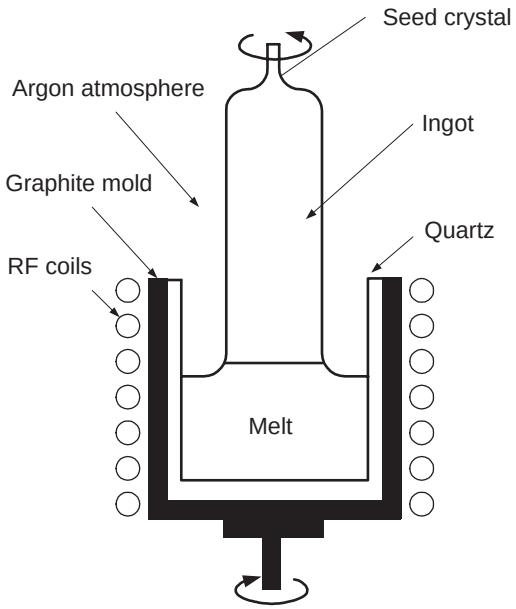

Figure 1: Schematic of CZ growth process

The magnitude of residual stresses is roughly proportional to the curvature of the temperature profile [1, 5]. As shown in Figure 4, to sustain a high growth speed (about 800°C/cm for 25 mm/min), a large interface temperature gradient is required. Excessive residual stresses may lead to the breakage of the ribbon during crystal growth [4, 6]. The following thermal processing in cell manufacturing such as oxidation and diffusion may also introduce non-uniform heating and cooling which results in a substantial thermal gradient and may introduce extra residual stresses or cause the redistribution of the original components.

1.3 Effects of Residual Stress on Silicon

Residual stresses may enhance the performance of a mechanical structure, an example in shot peening where the process induces compressive residual stresses on the surface of metal structures to improve the fatigue life. Surface mechanical treatments are not possible with silicon. Residual stresses in the silicon may cause mechanical failure during processing, affect the geometry stability of silicon-based devices, and change the optical or electrical

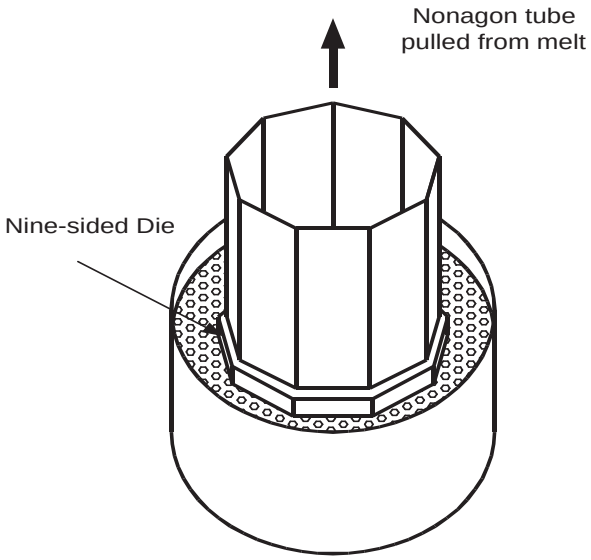

(a) Furnace

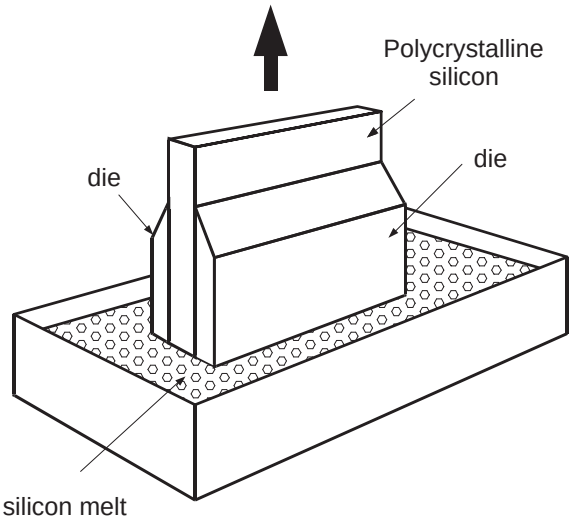

(b) The structure of the die

Figure 2: Schematic of EFG growth process

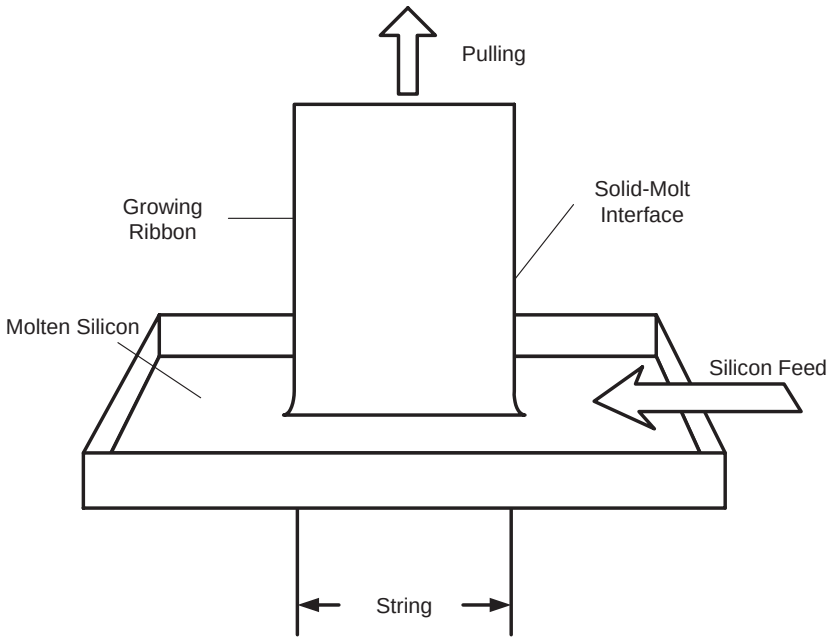

Figure 3: String Ribbon manufacturing process (from www.evergreensolar.com)

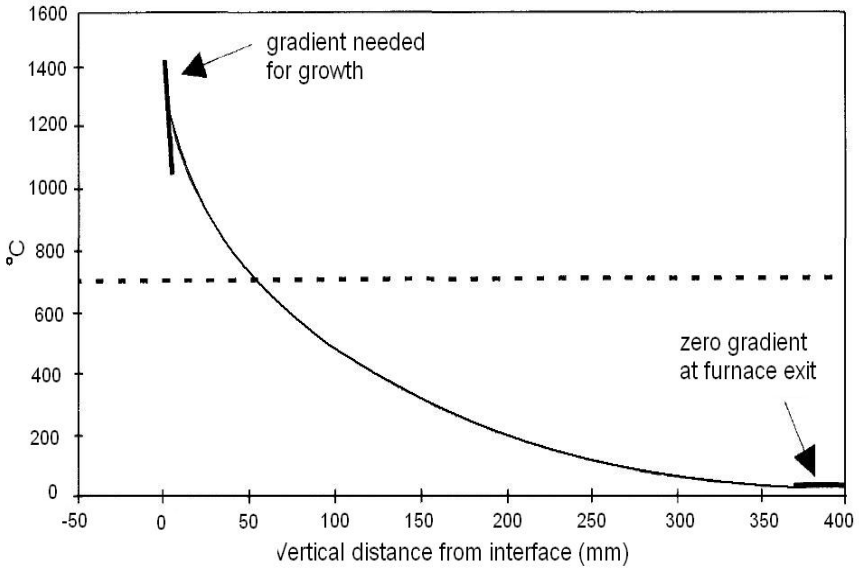

Figure 4: The temperature profile in the melt/solid interface of string ribbon silicon growth [1]

properties of devices. Tensile residual stresses in silicon will eventually lead to degraded mechanical performance, stress corrosion cracking, shortened lifetime and even catastrophic failure. Residual stresses may also cause warpage or buckling when the single crystal ingots, cast blocks or EFG/ribbon tubes are cut to wafers, so that further processing for cell fabrication [7, 8] is difficult. Furthermore, the perimeter of the wafer, and in some cases the front and back surfaces, may also contain micro-cracks which will eventually propagate and fracture the cell in handling during subsequent device fabrication [9] since cracks will propagate in the region of tensile residual stresses.

Besides fracture, residual stresses can also generate and propagate dislocations and it is believed that this will eventually impact the lifetime and thus the efficiency of photovoltaic cells. As sheet becomes thinner, the grown-in residual stresses, coupled with the stresses imposed during manufacturing, presents a formidable challenge.

There has been a significant effort to develop non-contact techniques that expose the in-plane residual stresses [10, 11], but this prior work is not suitable nor sensitive enough to implement in the manufacturing of photovoltaic cells. Our work has focused on developing a robust, non-contact optical method to determine the stress distribution in thin silicon sheet material, validate the technique in a statistically significant set of experiments and apply the techniques to sheet at various stages of photovoltaic cell processing so that the evolution of the stress distribution can be understood and perhaps optimized.

1.4 Overview of Residual Stress Characterization Methods

Residual stresses may be measured by non-destructive techniques, including X-ray diffraction, shadow Morié and ultrasonic microscopy; or by locally destructive techniques, including hole drilling and micro-indentation. Destructive techniques require that the residual stresses are released, usually through a destructive process that will destroy or damage the specimen.

Non-destructive methods are needed for in-situ quality monitoring for photovoltaic processing. Current methods use different principals to measure the residual stresses depending

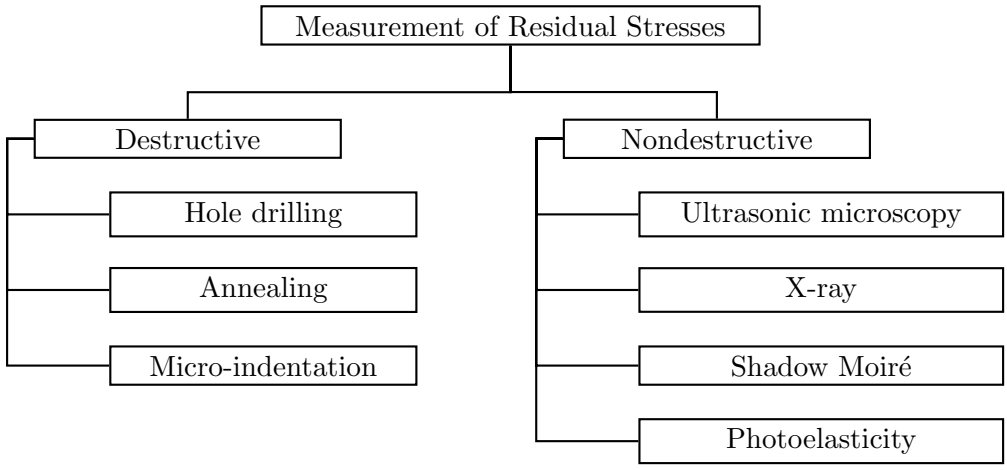

Figure 5: The methods for residual stress characterization

Table 1: Specifications of various techniques for residual stress characterization

Methods	Penetration	Spatial resolution	Accuracy
Hole drilling	$\sim 1.2 \times D_0$ *	50μm depth	$\sim$ 50MPa
X-ray diffraction	$\sim$ 50μm	1mm	20MPa
Ultrasonics	$>$ 10cm	5mm	10%
Raman	$<$ 1μm	1μm	50MPa
Shadow Moir	N/A	$\sim$ 200μm	$\sim$ 1MPa
Photoelasticity	No limit	$\sim$ 200μm	$\sim$ 1MPa

*D_0 The diameter of the drill hole

on the circumstances. X-ray diffraction [12] detects the strain-induced changes in the crystal lattice, which can be differentiated to obtain the residual stresses. The sensitivity of this technique is reported to be around 10 MPa [13,14]. However, this technique penetrates the top 30 μm layer, since x-rays are strongly absorbed within this depth. Therefore it is impossible for x-ray diffraction to obtain the residual stresses through the thickness of solids.

Ultrasonic microscopy [15,16] measures the residual stresses by propagation of acoustic waves with a change in the wave speed of the elastic waves in a medium under different

stresses. The main obstacle of this technique is that the relative change in wave speed is very small, typically of the order of 10^{-5} MPa^{-1}. Initial weak anisotropy and slight inhomogeneity in the material also cause large errors in the stress prediction. Therefore acoustoelastic microscopy essentially is limited to material uniform both in microstructure and composition such as single crystal silicon.

Shadow Morié can detect the residual stresses in circular or rectangular plates. A concentrated load is applied to the sample to deform it into the non-linear region where the in-plane residual stresses interact with the out-of-plane displacement. Danyluk and his group [3, 17–21] has developed the analytical theory for beam, rectangular and circular plate to extract residual stresses from the displacement measured by shadow Moiré. The limitations of this method are that a certain profile needs to be assumed for the residual stresses. For example, an axisymmetrical profile is assumed for circular plate. Since the residual stresses are forced to comply with the assumed profile, this technique is not sensitive to the local stress concentrations.

In the last number of years we have worked on various experimental techniques to obtain the in-plane residual stress in silicon, especially poly-crystalline silicon, with the photovoltaic industry in order to improve the efficiency and reliability of photovoltaic cells. This work is especially important now since the photovoltaic industry is tending toward thinner substrates to reduce the cost of materials, which currently is one-third of the total cost of a PV cell, the residual stresses are generally higher in thin materials and thus affect the production yield and long term reliability.

A near infrared polariscope has been proposed by Danyluk's group as a potential candidate for in-situ residual stress monitoring. This technique measures the stress-induced birefringence, which is proportional to the magnitude of the residual stresses, by probing the change in the polarization state of the transmitted light. The residual stresses are determined from the anisotropic stress-optic law. This technique senses strain directly as opposed to Shadow Morié, whose accuracy is often deteriorated by the differentiation of the measured displacement. Furthermore we propose the phase-stepping technique, which provides a fast and automatic way to extract the principal shear stress and its orientation

by rotating the optical elements in the polariscope.

1.5 Overview of Photoelasticity

Stress-induced birefringence was first discovered in glass by Brewster in 1816 [22]. The first systematical investigation of the complete theory was carried out by Neumann in 1841, who attributed the birefringence to the strain. In 1853, Maxwell related the birefringence to stress directly and developed the stress-optical laws. Coker and Filon [23] applied this technique to structural engineering in 1902.

The birefringence can be measured by a polariscope, which converts the change in the polarization of the transmitted light through the stressed specimen to the form of fringes. Based on the polarization of the input light, polariscopes are catalogued as plane polariscopes and circular polariscopes. The circularly polarized light is achieved by the combination of the polarizer and an extra pair of quarter waveplates. The experimental results obtained from the polariscope are photoelastic parameters, namely isochromatics and isoclinics, which represent the magnitude and direction of the principal stresses respectively. The photoelastic parameters are converted to principal stresses using an isotropic or anisotropic stress-optic law.

Traditional photoelasticity extracts the photoelastic parameters using fringe counting methods [24], which identify integral fringes by locating the center of the photoelastic fringes. The resolution of these methods is usually 0.1 fringe order because the center of the fringes is normally not well defined. Partial fringes can be measured by various compensation methods [25] with an accuracy of up to 0.01 fringe. The methods used for compensation are tension or compression strip, Babinet-Soleil compensator, Friedel's method and Tardy's method. The Friedel and the Tardy methods are more commonly used and are more practical in the sense that they do not require additional equipment. However, all methods of compensation presuppose knowledge of the principal directions at the point and require manual adjustment. Whole field mapping is accomplished by tedious scanning. Post (1955) [26, 27] introduced a fringe multiplier, which consists of two partial mirrors at the front and rear of the specimen, into a traditional polariscope to amplify

the birefringence up to tenfold at the cost of significant loss of spatial resolution and light intensity.

The fringe-counting technique has limited the application of traditional photoelasticity. To overcome these difficulties, a computer-based digital image processing system has been integrated into the polariscope to achieve automatic and more accurate analysis. A number of attempts have been made in 1950's based on point-by-point techniques. Brown and Hickson [28] and Frocht et al [29] first fitted a photo detector to their polariscopes in the 1950's to facilitate the location of the skeleton of photoelastic fringes. The automation of the full-field polariscope was made possible by the introduction of CCD camera in 1970's. In 1979 Mueller and Saackel [30] and Seguchi [31] independently integrated a digital camera and computer into the polariscope and used fringe thinning technique to find the fringe skeletons.

The real potential of digital photoelasticity was realized only when the concept of identifying fringe fields as phase maps can into existence when Voloshin and Burger [32] introduced the half fringe photoelasticity technique. This technique can sense full-field continuous phase retardation rather than discrete fringe skeletons. However the fringe order in the field was limited to half a fringe or less and the isoclinics were not obtained. Recent research in digital photoelasticity has focused on three methods: phase stepping, spectral content analysis and Fourier transform.

The phase stepping concept for photoelasticity was first introduced by Hecker and Morche [33] in 1986, who used plane and circular polariscopes to extract isochromatic and isoclinics respectively. This technique records multiple images, normally three to six images, corresponding to different optical arrangements and uses the image intensities to solve for the photoelastic parameters for each pixel. The background light intensity is also consider as a variable to compensate for the non-uniformity of transparency. Patterson and Wang [34–41] simplified the Hecher and Morche approach by using a circular polariscope to extract both photoelastic parameters. However, both their techniques have the major disadvantage that it requires the operator to define the absolute isochromatic fringe order at a point in the field of view, since it only provides relative retardation in the range of [0,

π]. Multiple wavelength [42, 43] and load stepping [44–46] were developed to determine the absolute fringe order and zero order fringe.

Redner [47,48] in 1984 first introduced the spectral content analysis method, which identifies the isochromatic parameters at a point on a sample by its unique spectral signature. This is a point-by-point measurement and needs special calibration of the spectral signature of a particular light source. Haake and Patterson [49] extended this technique to measure complicated fringe patterns with both low and high fringe orders. Carazo-Alvarez et al [38] combined phase stepping with spectral content analysis for the purpose of phase unwrapping to fully automate the polariscope. Full-field measurement was made possible by the technique of three fringe photoelasticity (TFP) [50, 51], which can only extract chromatics within the order of three fringes.

Quan and Morimoto [52] introduced in 1993 the FFT to analyze the photoelastic fringes. In this technique, an optical wedge is used to introduce a carrier fringe into the stress induced fringe pattern. The disturbance of stress on the carrier fringe can be detected by a Fourier transform of the modulated fringe pattern. However, the isolation of the photoelastic spectrum from the background spectrum requires higher carrier frequencies, which may cause aliasing in the FFT when a low sample rates is used. This technique requires further development for it to be suitable for practical applications.

In this research, an infrared polariscope combined with a fringe multiplier and phase-stepping was used to measure the residual stresses in thin silicon plates with an accuracy of 1 MPa. This technique can finish one measurement in several seconds and has the potential for in-situ monitoring.

1.6 Overview of Photoelasticity in Semiconductors

Photoelasticity has been applied to semiconductor materials since the 1950's. Single crystal silicon was the first material to be studied with this technique. Since silicon is transparent to light with a wavelength above 1100 nm, near infrared light (NIR) was used as the light source in the polariscopes. A number of researchers have used polariscopy to study silicon because this is the only non-destructive technique capable of providing information on the

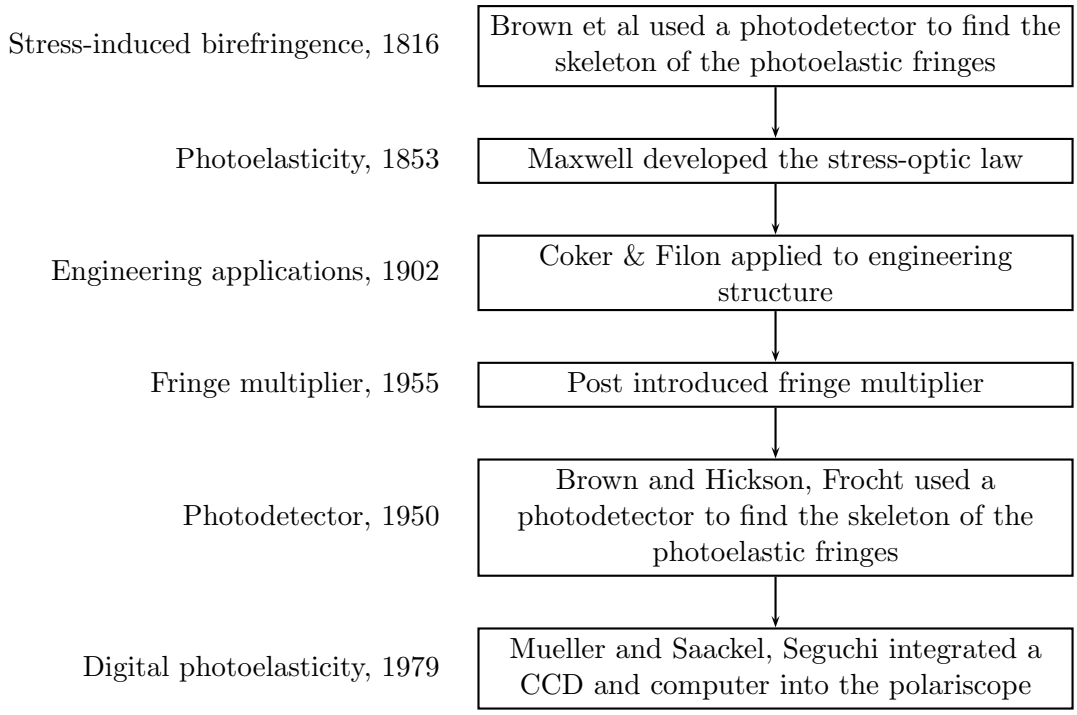

Figure 6: The history of the research on photoelasticity

eventual reliability of electronic devices that use silicon as a substrate.

Bond and Andrus [53] reported the first fringe pattern of residual stresses in silicon in 1955 with infrared illumination (Figure 7). The quantitative measurement of residual stress in silicon was made possible after the piezo-birefringence constants was first measured by Giardini(1958) [54]. Later Lederhandler [55], Denicola and Tauber [56], Kotake and Takasu [57], Wong et al [58] used this technique to characterize the residual stress for the purpose of process control. The photoelasticity of other semiconductor materials such as GaP, GaAs is measured by Dixon in 1967 [59] and Kotake et al [60]. All this prior work has limited applicability because electronic devices are fabricated on silicon wafers with thicknesses less than 0.5 mm, which is not enough to build up a measurable birefringence effect for the prior experimental methods. Zheng [61,62] used a six-step phase-stepping and fringe multiplier techniques that can overcome prior experimental limitations and extract residual stresses in thin samples. A scanning method [63, 64] has also been developed for wafer characterization, but it takes a considerably long time to scan a sample.

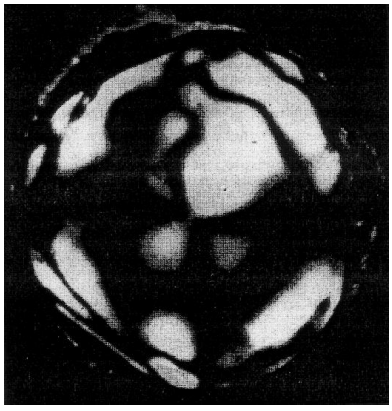

(a) Birefringence patterns of a highly stressed silicon wafer

(b) Birefringence patterns of a silicon (100) wafer

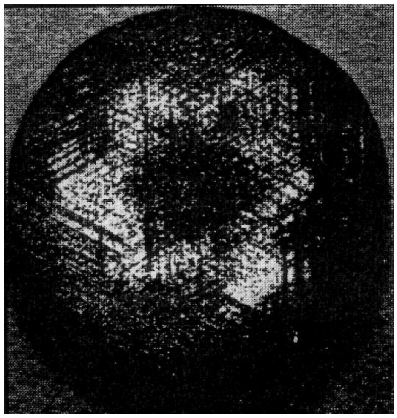

(c) Etched pit picture

Figure 7: Photoelastic fringes in silicon

In addition to the thickness, the extraction of the residual stresses in crystalline silicon samples from the photoelastic parameters also requires a knowledge of the influence of crystal anisotropy on the stress-optic coefficients. Landerhandler [55] and Denicola and Tauber [56] measured the distribution of residual stresses in a Czochralski-grown ingot, and the residual stresses were evaluated qualitatively in terms of fringe order without considering the anisotropy. Quantitative residual stresses were obtained by Kotake et al [60] in as-grown gallium phosphide crystals from a stress-optic law derived by taking into account the crystal anisotropy. However, these authors assumed that the principal stress directions coincided with the optical directions, which has been proven to be not always valid. Yamada [65] studied the anisotropy of the strain-optic coefficient in a (001) gallium-arsenide substrate without experimental verification. Iwaki and Koizumi [66] analyzed the anisotropy of the (001) single crystal silicon with different symmetries, but the stress-optic coefficient was not obtained. Liang and Pan [67] presented an analysis of the stress-optic relationship of the (001) and (111) silicon, but both the illumination and the observation were in-plane only. In the course of our study we will derive the stress-optic laws for the (001) and (111) silicon observed along the normal direction and calibrate them using four-point bending of "plates" sectioned from silicon wafers.

1.7 Conclusions

The specifications of various techniques for residual stress measurement were discussed. A polariscope with a fringe multiplier and phase-stepping was chosen for this research based on the accuracy and the potential for in-situ monitoring.

CHAPTER II

RESEARCH PLAN

2.1 Objective

The objective of this research is to develop a non-destructive method to obtain in-plane residual stress in thin single and poly-crystalline silicon, establish the fundamental principles to convert the experimental results to stresses, correlate the residual stresses to other electronic properties.

2.2 Approach of the Research

In this research, a full-field near infrared (NIR) polariscope was built and calibrated. One of the challenges to characterize thin silicon sheets is the relatively low sensitivity of traditional polariscopy compared with the magnitude of residual stresses. Figure 8 shows the photoelastic fringes of a circular disk under compression. In the image, multiple fringes can be observed. Figure 9 shows typical images of a silicon beam under externally applied stresses. There are no obvious fringes as can be seen in the images. Only a variation in light intensity can be observed. In order to make the system capable of measuring the residual stresses in thin silicon sheets, a fringe multiplier which consists of two partial mirrors has been incorporated into the polariscope, and a six-step phase stepping technique used to extract partial fringes.

The flow chart of the research on the polariscope is show in Figure 10. The objective is to measure the residual stress in crystalline silicon. To ensure the reliability of the polariscope, an error analysis was conducted. As shown in Figure 10 and 12, the experimental results obtained from the polariscope are photoelastic parameters, e.g. retardation and isoclinic angle, which corresponds to the magnitude and orientation of the residual stresses respectively. To convert the photoelastic parameters to residual stresses, the stress-optic law and corresponding coefficients are required. The anisotropic stress-optic law of both

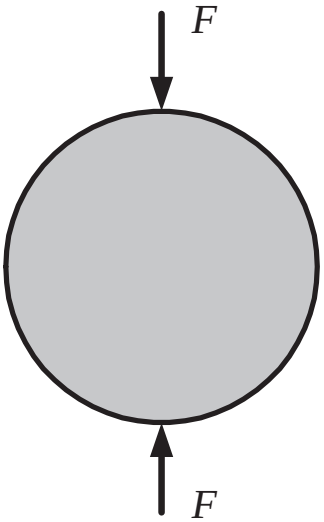

(a) Setup

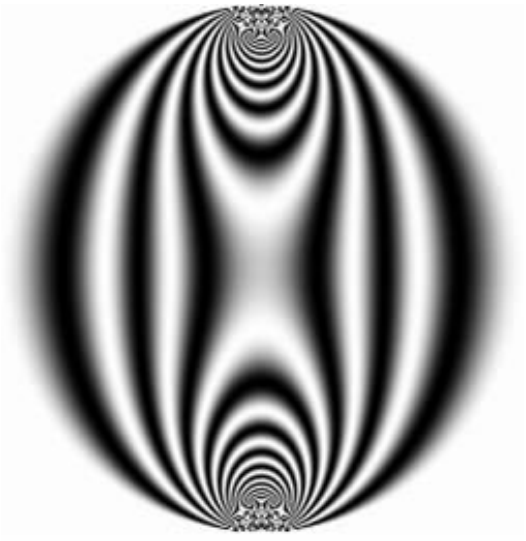

(b) Photoelastic fringes

Figure 8: The photoelastic fringes of a disk under compression

(a) 1st

(b) 2nd

(c) 3rd

(d) 4th

(e) 5th

(f) 6th

Figure 9: The six images of phase-stepping for four-point bending of a silicon beam

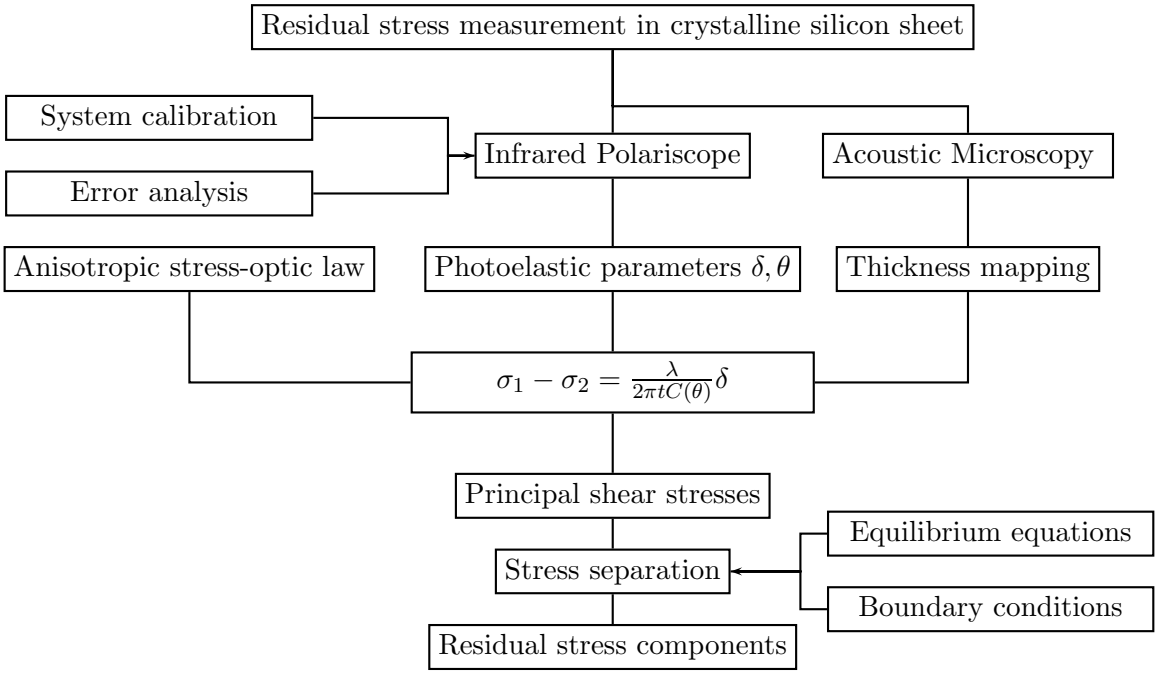

Figure 10: The experimental methods used for residual stress characterization

single and polycrystalline silicon was analyzed. The coefficients of both types of silicon are calibrated by a four-point bending fixture.

The polariscope together with other techniques was applied to characterize the residual stresses in CZ, cast, ribbon and EFG silicon (Figure 11). The evolution of residual stresses and minority lifetime was also monitored in order to provide a fundamental understanding of the mechanism of how silicon growth and cell processing relate to the residual stresses. The correlation between residual stresses and electronic properties was also investigated.

2.3 Outline

The description of this research begins at chapter 3, which summarizes the experimental setup of the polariscope and the analysis of the spatial resolution and light loss of the fringe multiplier. The fringe multiplier is calibrated using a four-point bending fixture. The procedure of the phase-stepping technique, which extracts the photoelastic parameters from experimental results, is also discussed.

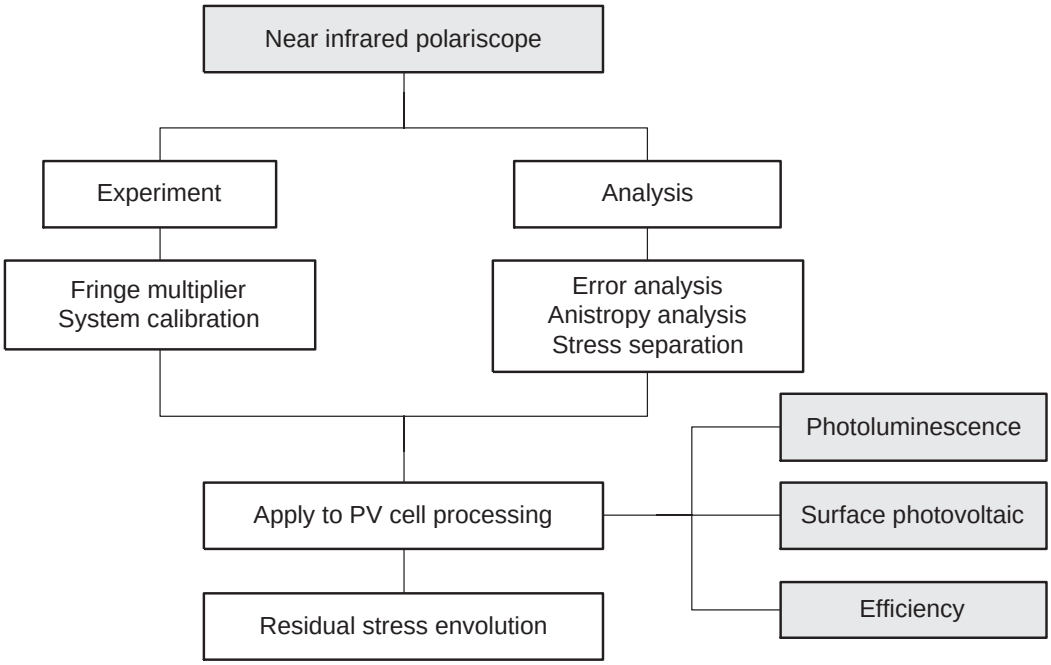

Figure 11: Overview of the research on the infrared polariscope

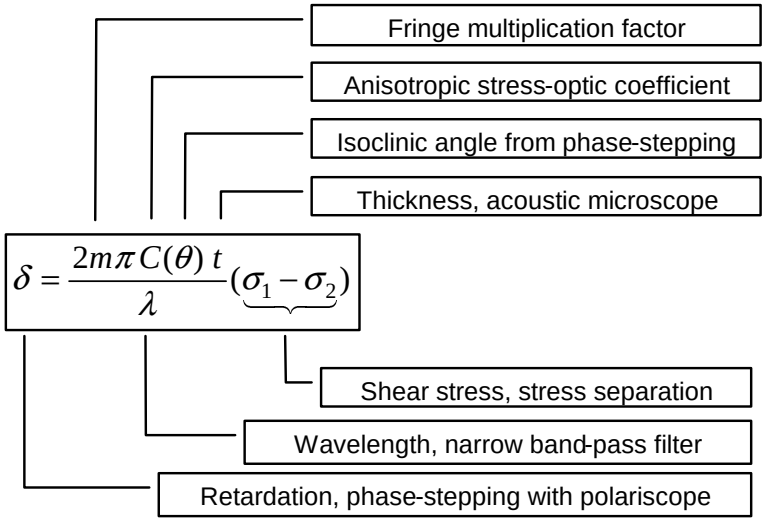

Figure 12: Description of the relationship between the stress-optic law of anisotropic materials and the measurement

Chapter 4 describes the analysis of the systematic and random errors in the circularly polarized phase-stepping polariscope. The sources of error analyzed consist of the misalignment of the optical elements and the error in the image digitization. The results show that the error in stress is approximately 1.0 MPa and the error in the orientation of the stress can be ignored except in the undefined regions. The systematic misalignment in the polarizer and two quarter waveplates was rectified before analysis.

Chapter 5 presents the analysis of the stress-optic coefficients (001), (011) and (111) silicon. The coefficients are obtained analytically in terms of the stress-optic tensor.

Chapter 6 summarizes the calibration of the stress-optic coefficients of the CZ, EFG and cast silicon. A four-point bending fixture is used for the calibration. The samples are silicon beams with various orientations sectioned from the silicon wafers. The experimental data are analyzed using least-square fit.

Chapter 7 summarizes the research on the characterization of residual stresses and lifetime of polycrystalline sheet silicon for photovoltaic application. The full-field polariscope and scanning room temperature photoluminescence (PL) are used to characterize silicon sheet after certain processing steps. The characteristics of the spatial distribution and the quantitative correlation between the residual stresses and the lifetime are presented. The correlations between the residual stress, PL and efficiency are also investigated.

CHAPTER III

INTRODUCTION TO PHOTOELASTICITY

3.1 Summary

This chapter describes the experimental setup of the polariscope. The spatial resolution and light loss of the fringe multiplier will be analyzed. The procedure of the phase-stepping technique will be discussed. A four-point bending fixture will be used to calibrate the fringe multiplier.

3.2 Principles of Photoelasticity

Stresses may change the optic properties of crystals by virtue of the stress-optic effect. When a polarized light passes through a stressed crystal, birefringence occurs. The birefringence changes the polarization state of the emerging polarized beam, and this change can be convert into the form of fringe patterns by a polariscope (Figure 13). Silicon is opaque to visible light but transparent to near infrared light. Stress in silicon can be measured by the near infrared birefringence fringe patterns.

The stress-induced birefringence changes the velocity of a light propagating through the material. The speed in a birefringent material depends on the orientation of the electric field vector relative to the optical axes of the material, or the principal axes of the stresses for an artificial birefringent material. For an arbitrarily polarized wave, the field splits into two components with different propagation velocities, e.g. ordinary and extraordinary waves. After these two waves are recombined, as shown in Figure 14, their relative phase is different from its initial value, so the state of polarization has effectively varied. The speed difference results in a phase lag, R, between the two electrical field components. This phase lag can be detected with the technique known as photoelasticity. After the polarized light travels through the plane specimen with a thickness of t, the relative retardation R is

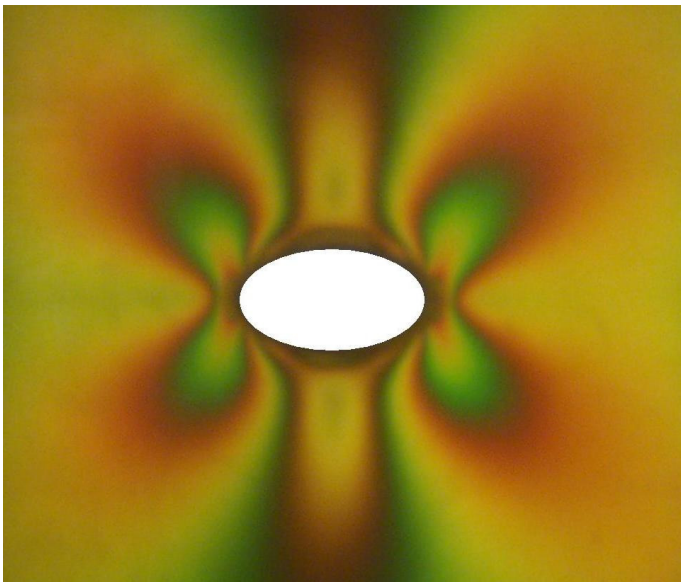

Figure 13: Birefringence of stress concentration around an ellipse hole and its observation with a white light polariscope (from http://www-bsac.eecs.berkeley.edu/)

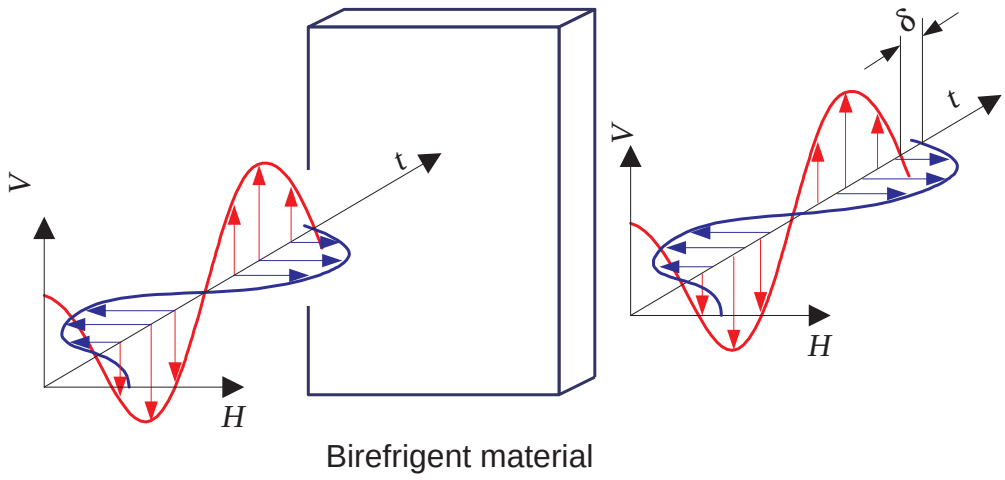

H Horizontally polarized
V Vertically polarized
δ Birefringent retardation

Figure 14: The effect on light propagation of birefringence

expressed as:

$$R = C(\theta)t(\sigma_1 - \sigma_2) \tag{1}$$

where σ_1 and σ_2 are the two in-plane principal stresses in the specimen, and t and $C(\theta)$ are the thickness and the relative stress-optical coefficient of the specimen respectively. The stress-optical coefficient is constant for an isotropic material, but for an anisotropic material such as silicon, it varies with the orientation of the stresses. This will be discussed in detail in Chapter 5. The retardation R is usually expressed by the relative angular retardation δ, which is also known as the isochromatic phase or isochromatics.

$$\delta = R \Big/ \frac{\lambda}{2\pi} = \frac{2\pi C(\theta)t}{\lambda}(\sigma_1 - \sigma_2) \tag{2}$$

where λ is the light wavelength. Equation 2 shows that the sensitivity of photoelasticity is inversely proportional to the illumination wavelength, therefore, the infrared monochrome wavelength should be as short as possible in order to achieve the highest sensitivity. The transmission spectrum curve of silicon in Figure 15 shows that silicon is opaque to the ultraviolet and visible light but the transmission ratio rises sharply to over 50% around 1100 nm, being constant in the whole near infrared spectrum range. A wavelength of 1150 nm, which is close to the edge of the transparent window, was chosen as the light source. This wavelength is obtained using an interference band pass filter with a bandwidth of 10 nm.

3.3 Experimental Setup of the Polariscope

A near infrared (NIR) polariscope with fringe multiplier was designed as shown in Figure 16. The setup includes a white light tungsten-halogen lamp as the light source, two aspherical lenses of 240 mm in diameter, two near infrared linear polarizers of 100 mm in diameter, two first-order quarter waveplates with a wavelength of 1150 nm and 100 mm in diameter, two beam splitters of 240 mm in diameter, a specimen stage, a spatial filter, an interference filter with a wavelength of 1150 nm and half magnitude full width (HMFW) of 10 nm, an imaging lense of 75 mm in diameter, an Electrophysics high-sensitive infrared video camera, a Matrox Meteo II image grabber board and a personal computer. The system is placed on

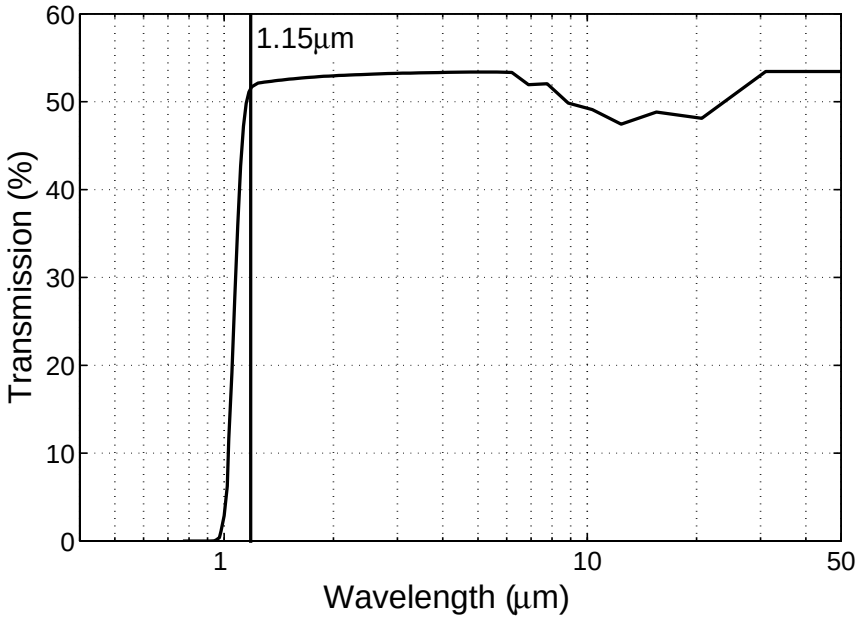

Figure 15: The transmission spectrum of silicon

an optical bench, and accommodate samples with a diameter of up to four inches.

The light emitted from the tungsten-halogen lamp first is collimated by the aspherical lens L_1, then converted from randomly polarized to linearly polarized by the first polarizer P_1. The first quarter waveplate Q_1 is orientated with its axis at 45° after the polarizer, and changes the linearly polarized light to circularly polarized. A fringe multiplier, which consists two beam splitters B_1 and B_2, is located between the two quarter waveplates Q_1 and Q_2. The outside surfaces are coated with an anti-reflection coating to reduce reflection and ghost fringes, and the outside surfaces are coated with a reflection rate of 85% for $\lambda = 1150$ nm to minimize loss in light intensity. The silicon sample is fixed on an adjustable stage located between the two partial mirrors. An opaque window is placed right before the specimen to block any stray light from the perimeter. The birefringence inside the sample further change the circularly polarized light to elliptically polarized, and this change is converted to the form of fringes by the second quarter waveplate Q_2 and polarizer P_2. These two elements will be rotated during the experiment for the purpose of phase stepping. The quarter waveplate Q_2 and polarizer P_2 are usually called output quarter waveplate and analyzer, respectively. The light is focused by the second aspherical

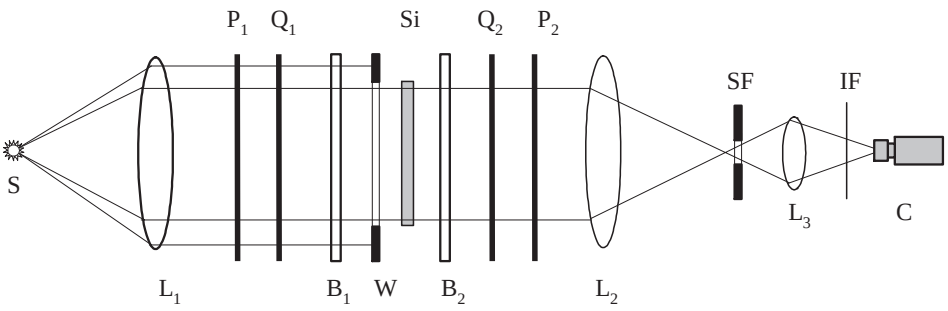

S	Tungsten-halogen lamp
L_1,L_2,L_3	Aspherical lenses
P_1,P_2	Near infrared polarizer and analyzer
Q_1,Q_2	Near infrared quarter waveplate
B_1,B_2	Beam splitter
SF	Spatial filter
IF	Infrared interference filter
C	High sensitivity near infrared camera
Si	Silicon sample
W	Opaque window

Figure 16: The experimental setup of the infrared residual stress polariscope

lens L_2. At the focus plane is located an adjustable spatial filter. The second beam splitter B_2 is tilted an small angle ϕ_i so that the light beam of different fringe multiplication factor is separated at the focus point. By filtering at a specific focusing point, a specific fringe multiplication is selected. An imaging lens is put behind the spatial filter to focus the fringe image on the detector of the video camera. A narrow-band near infrared filter is inserted in front of the detector so that only the image of 1150 ± 5 nm is sensed by the camera.

The light source is a tungsten-halogen lamp, whose spectrum is shown in Figure 17. It covers a broad range in both visible and near infrared regions. As shown in the figure, the band pass filter only selects a bandwidth $\Delta\lambda = 10$ nm, which significantly reduces the light intensity. The lose can be compensated by the high output power of the tungsten-halogen bulbs. With a 150 W bulb, the remaining power after narrow band filtering is over 200 mW, which is acceptable for the full-field measurement. To further compensate for the excessive loss in high fringe multiplication, a broad bandpass filter with a FMHW of 100 nm can be used at the cost of wavelength mismatch in the quarter waveplates. Using an infrared laser is another choice for the light source, especially for the benefit of reducing the loss in

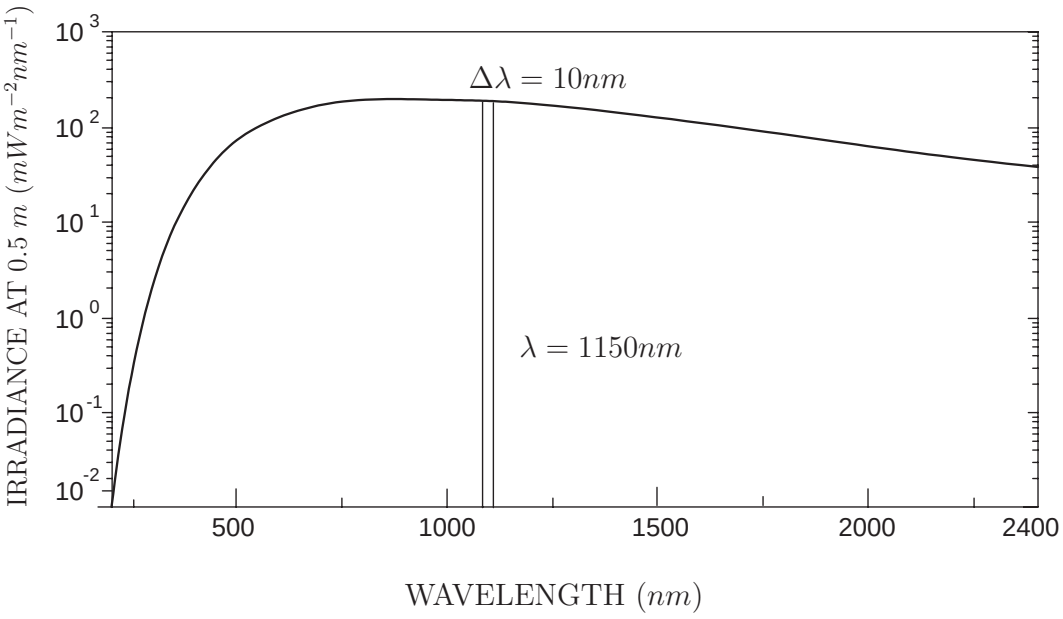

Figure 17: The spectrum of the tungsten light source

spatial resolution in fringe multiplication. But the self-interference normally dominates the photoelastic fringes of low stress. Therefore, the tungsten-halogen bulb was chosen as the near infrared point light source for the system.

The camera is connected to an image grabber board installed on a personal computer. The gray-level images are digitized by the grabber with the size of 640×480 pixels and depth of 8 bits, or 256 gray levels. The digitized images normally contain electronic noise, especially for dark images, which can result in spurious solutions. In order to reduce the noise, time domain filtering, which is realized by averaging 30 to 300 sequentially grabbed images with respect to the same object, is performed on the images. The image grabbing software, *TZGrab*, is implemented in Microsoft Visual C++ with a Windows interface shown in Figure 18. This software is capable of adjusting image contrast and brightness, checking for the saturation, filtering electronic noise and saving images.

The optimal images captured are those with highest maximum allowed brightness and reasonable contrast. The brightness is limited by the 256 gray levels of the digitizer. For low stress, normally the first image in the phase stepping has the highest brightness. The first step is to adjust this image to the maximum brightness, either by adjusting the power

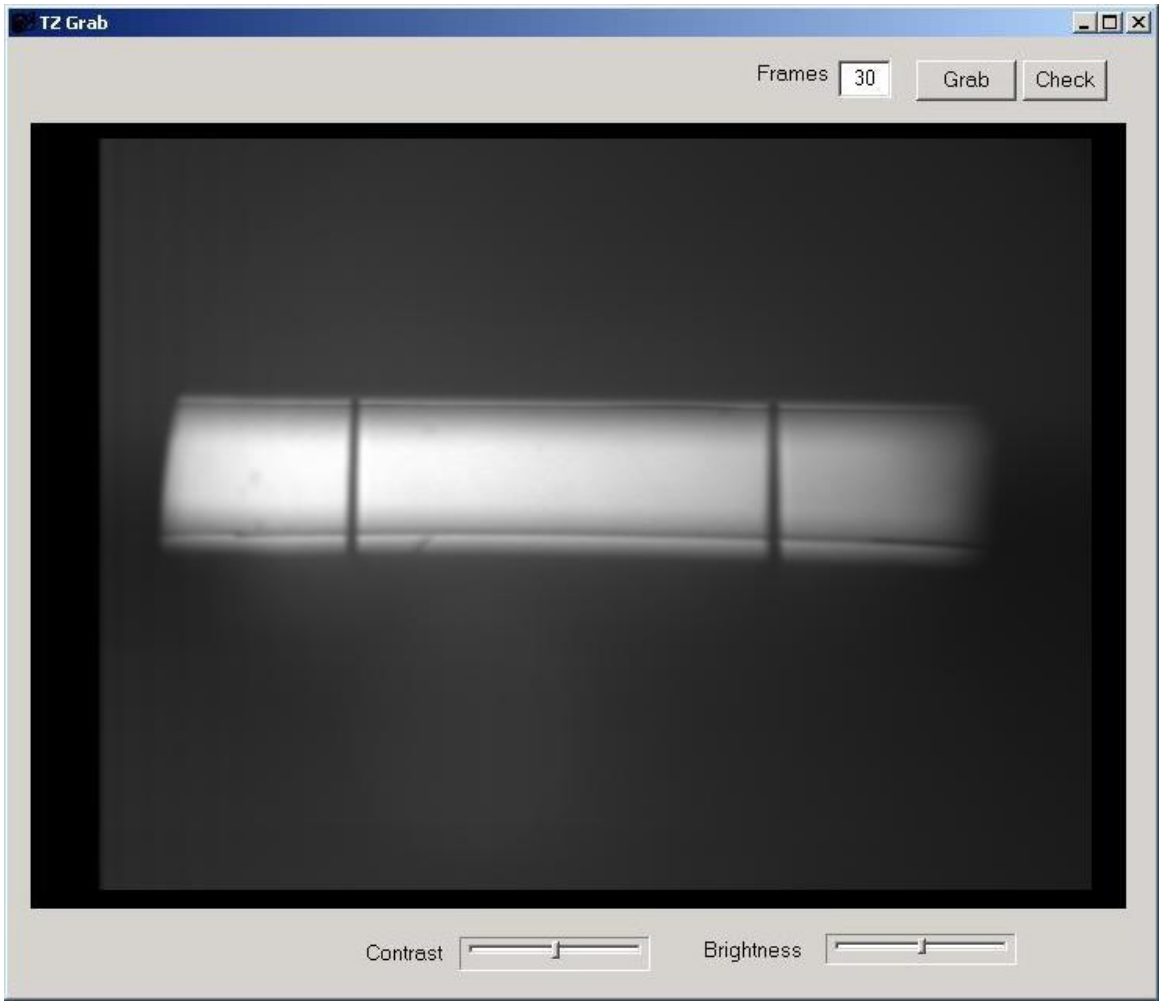

Figure 18: The Windows interface of image grabbing program *TZGrab*

of the light source or "Brightness" slider on the Windows interface. The overflow can be checked by pressing the "Check" button, which detects the percentage of pixels which are saturated. Usually the percentage is controlled at 0.2% to avoid excessive saturation. The adjustment of the brightness and contrast may need to be repeated several times because they may influence each other. It should be pointed out that no further adjustment is needed in the brightness or contrast during phase stepping.

3.4 Fringe Multiplier

The purpose of the fringe multiplier is to increase the sensitivity of the polariscope [27]. As shown in Figure 19, the light passes through the sample and is reflected back and forth by the two splitters and passes through the specimen multiple times, and thus the photoelastic retardation is amplified by this factor. The second splitter is tilted slightly at an small angle of ϕ_i, from 1/2 to 1°, to separate the light beams of the different multiplication factors. With a spatial filter, the desired focus point corresponding to a particular fringe multiplication factor can be selected for analysis. The k-th focus point of the forward rays represents the multiplication factor m, which equals $2k-1$. The physical meaning of the multiplication factor is that it increases the equivalent thickness of the specimen m times, therefore the sensitivity of the polariscope is increased by m times.

$$t = mh \tag{3}$$

where h is the specimen thickness, and t is the effective thickness. The above equation also shows the effective thickness is amplified by the factor of m.

The drawbacks of the fringe multiplier are the significant loss of light intensity and the spatial resolution. Assume the transmission and reflection coefficients of the beam splitters are T_λ and R_λ respectively. Then, $T_\lambda + R_\lambda = 1$ for an ideal mirror with no absorption. The light intensity of the multiplied fringe pattern with the multiplication factor of m, when compared with the intensity without the multiplier, is decreased by the factor of

$$\frac{T}{T_0} = T_\lambda^2 R_\lambda^{m-1} T_{\lambda_{Si}}^{m-1} \tag{4}$$

where $T_{\lambda_{Si}}$ is the transmission ratio of silicon corresponding to wavelength λ, T_0 is the

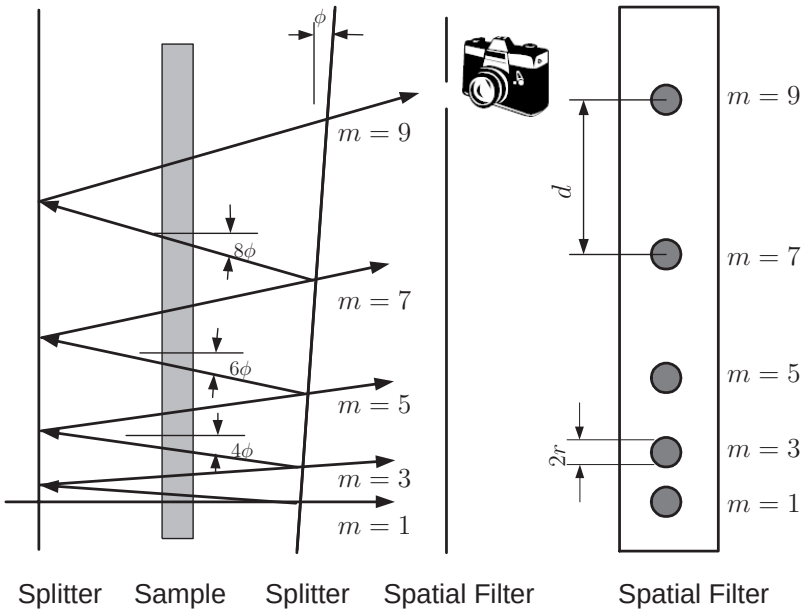

Figure 19: Fringe multiplier with two beam splitters. The right splitter is tilted ϕ (°), m is the fringe multiplication factor

emerging light intensity without the multiplier, and T is the reduced light intensity from the fringe multiplier. The loss in intensity can be minimized by properly selecting the transmission and reflection coefficients, T_λ and R_λ, of the two beam splitters. The reflection coefficient for minimum light intensity loss for a fringe multiplication factor m can be obtained by solving $\frac{d(T/T_0)}{dT_\lambda} = 0$.

$$T_{\lambda max} = \frac{m-1}{m+1} \tag{5a}$$

or

$$R_{\lambda max} = \frac{2}{m+1} \tag{5b}$$

Since $T_{\lambda max} + R_{\lambda max} = 1$. As shown in Equation 5a and 5b, the optimal reflection or transmission coefficient of the beam splitters is a function of the fringe multiplication factor, therefore, it is impossible to optimize the beam splitters for all the different fringe multiplication factors simultaneously. In this research, the objective of the fringe multiplier is to increase the sensitivity by about one order of magnitude, or $m = 9$. The optimal reflection and transmission coefficients obtained from equation 5 are 83% and 17% respectively, so

Table 2: The loss in light intensity in fringe multiplier

m	$R_\lambda = 0.5$	$R_\lambda = 0.85$	$R_\lambda = 0.83$	$R_\lambda = 0.85$ with Si
N/A	1.0000	1.0000	1.0000	1.000000
1	0.2500	0.0250	0.0289	0.022500
3	0.0625	0.0163	0.0199	0.004030
5	0.0156	0.0117	0.0137	0.000722
7	0.0039	0.0085	0.0094	0.000129
9	0.0010	0.0061	0.0065	0.000023
11	0.0003	0.0039	0.0045	0.000004

the reflection coefficient in this setup is chosen as 85%.

Table 2 shows the light loss for different reflection ratios of 50%, 85% and 83%. It can also be found that a low refection partial mirror works far better for the low fringe multiplication factors, but for high multiplication, e.g. $m > 5$, the high reflection mirror works better. For $T_\lambda = 0.85$, only 0.07% and 0.002% of the total light intensity remains in order to improve the sensitivity by half ($m = 5$) and one order ($m = 9$), respectively. As a make-up to the light loss, a powerful light source of 250 W and/or a highly sensitive camera are required.

The loss of light intensity is not the only problem for the fringe multiplier. Because the intensity of $m = 1$ is 5600 times stronger than that of $m = 11$, the stray light of low multiplication factor will overwhelm the images of the higher ones when appropriate measures are not taken. The contamination can be reduced by completely blocking the stray light from the perimeter of the sample with an opaque window. The sample should also be tilted with a small angle to avoid the internal reflection.

Another major drawback of the fringe multiplier is the loss in spatial resolution. This problem is more severe for the sample which has a higher spatial variation in stress, such as EFG and ribbon silicon. The spatial resolution is proportional to the distance of the two partial mirror and the inclination of the second partial mirror. Normally the inclination angle is close to half degree, $\phi_i = 1/2^\circ$, which is dependent on the diameter of the light spot.

Table 3: The loss in spatial resolution in fringe multiplier (mm)

m	Separation $20mm$	Separation $10mm$	Separation $5mm$
N/A	0.0	0.00	0.00
1	0.4	0.02	0.01
3	1.2	0.60	0.03
5	2.8	1.40	0.07
7	5.2	2.60	1.30
9	8.4	4.20	2.10

For smaller light spot, there is less distance required to separate them apart by the spatial filter, and thus a smaller inclination angle can be used. But smaller light spot will reduce the light intensity, which is critical for the fringe multiplier because of the significant loss. Therefore there is trade off between the spot size and inclination angle. Another method to increase the spatial resolution is to minimize the distance between the two partial mirrors. The distance can be reduced to 20 mm for four-point calibration, and 5 mm for photovoltaic samples.

The spatial resolution is list in Table 3 for different separation between the partial mirrors. To reduce to the effect, the spatial resolution can be arranged in particular direction which has less spatial variation, for example, in the horizontal direction for four-point bending, or in the pulling direction for EFG and ribbon samples.

The non-ideal point light is another concern in the experiment. As shown in figure 20, due to the finite dimension of filament and the non-spherical reflector of the Tungsten light source, an ideal collimated light could not be obtained. The light emitted from different parts of the filament will travel through different transverse position in the sample before they are focused by the camera. All stresses along the light path contribute to the phase modulation of the polarized light. Thereafter this transverse shift reduces the spatial resolution of the measurement. The stress result measured from this outgoing light is the average stress along its light path.

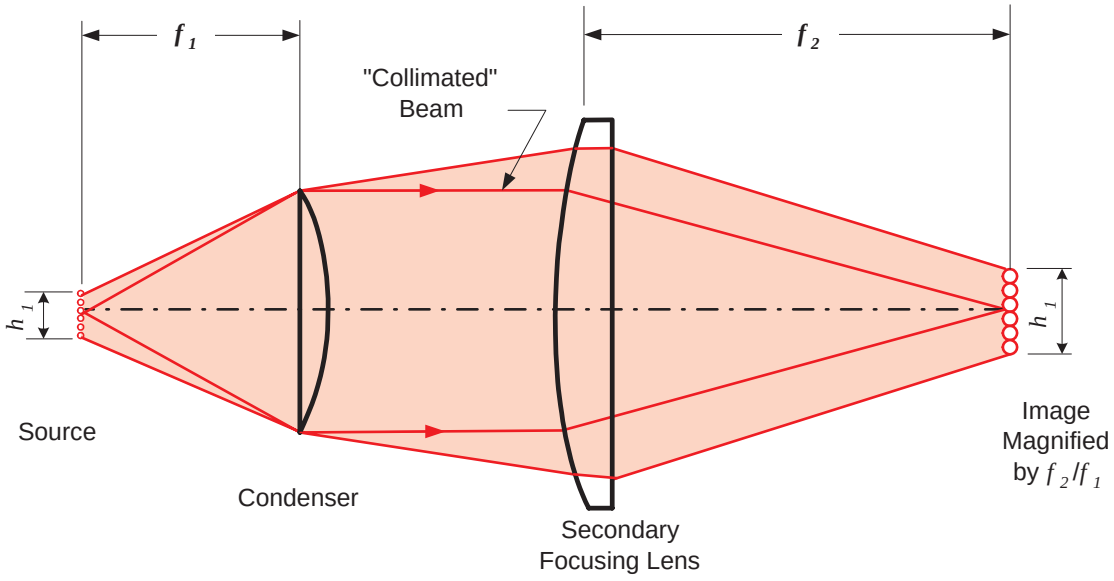

Figure 20: Effect on spatial resolution of finite dimension of light source

3.5 Phase Stepping Photoelasticity

Phase stepping is used to extract photoelastic parameters from the transmitted light automatically. This technique offers rapid, accurate measurements resulting in full-field maps of the isochromatic and the isoclinic parameters. In a polariscope as designed in Figure 16, the light emerging from the analyzer at any point (x, y) takes the general form:

$$I(x,y) = I_m + I_a[\sin 2(\beta - \alpha)\cos\delta - \sin 2(\theta - \alpha)\cos 2(\beta - \alpha)\sin\delta] \tag{6}$$

where I is the image captured by the camera, I_m takes account of stray light; I_a is the contrast of the image, which is the intensity emerging when the axes of the specimen and all the optical elements in the polariscope are parallel; α and β are the orientation angles between the reference axis and the slow axis of the analyzer, output quarter waveplate respectively, and θ is the isoclinic angle. It should be noticed that all the parameters, I_m, I_a, δ and θ, in the equation are functions of position (x, y) on the sample.

There are four unknowns, I_a, I_m, δ and θ, in Equation 6. At least four simultaneous equations are needed to solve for all the unknowns. By rotating the analyzer and/or output quarter-wave plate, a set of equations of the form of Equation 7 are generated to solve for δ and θ. Patterson [33] used increments for both quarter waveplate and analyzer which result

Table 4: Six-step phase stepping of a circular polariscope

No.	Waveplate (α)	Analyzer (β)	Intensity I_i
1	0	$\pi/4$	I_1=$I_b + I_a(1 + \cos\delta)$
2	0	$-\pi/4$	I_2=$I_b + I_a(1 - \cos\delta)$
3	0	0	I_3=$I_b + I_a(1 - \sin 2\theta \sin\delta)$
4	$\pi/4$	$\pi/4$	I_4=$I_b + I_a(1 + \cos 2\theta \sin\delta)$
5	$\pi/2$	$\pi/2$	I_5=$I_b + I_a(1 + \sin 2\theta \sin\delta)$
6	$3\pi/4$	$3\pi/4$	I_6=$I_b + I_a(1 - \cos 2\theta \sin\delta)$

in six independent images.

For $\alpha = 0$ steps, $\beta = \pi/4$ and $\beta = -\pi/4$ result in the following light modulation:

$$I_1 = I_m + I_a \cos\delta \tag{7a}$$

$$I_2 = I_m - I_a \cos\delta \tag{7b}$$

For $\alpha = \beta = 0, \pi/4, \pi/2$ and $3\pi/4$ respectively the intensities result in the following light modulation:

$$I_3 = I_b + I_a(1 - \sin 2\theta \sin\delta) \tag{7c}$$

$$I_4 = I_b + I_a(1 + \cos 2\theta \sin\delta) \tag{7d}$$

$$I_5 = I_b + I_a(1 + \sin 2\theta \sin\delta) \tag{7e}$$

$$I_6 = I_b + I_a(1 - \cos 2\theta \sin\delta) \tag{7f}$$

Then the isoclinic angle θ at any point (x, y) over the specimen can be obtained by using the following equation:

$$\theta = \frac{1}{2} \arctan 2(I_5 - I_3, I_4 - I_6) \tag{8}$$

which gives θ in the range of $[-\pi/2, \pi/2]$. And phase retardation is given by

$$\delta = \arctan 2\big((I_5 - I_3)\sin 2\theta + (I_4 - I_6)\cos 2\theta, I_1 - I_2\big) \tag{9}$$

This Equation extends the range of retardation to $[0, 2\pi]$ from $[0, \pi]$ provided by the equation proposed by Patterson and Wang [34]. This expansion reduces the use of phase unwrapping, which is difficult for multicrystalline silicon because of the non-uniformity in the transmitted light intensity and the potential for highly localized stress concentrations.

After getting the absolute retardation and fringe multiplication, the principal stress difference $\sigma_1 - \sigma_2$ can be calculated with the following equation by substituting the results obtained from equation 8 and 9 into equation 2

$$\sigma_1 - \sigma_2 = \frac{\lambda}{2m\pi hC(\theta)}\,\delta \tag{10}$$

The images of the phase stepping are processing by program *ResidualStress* developed in Matlab. The interface of this program is shown in Figure 21. This program is capable of extracting the photoelastic parameters, residual stresses, probability distribution. The area of interest can be chosen using a rectangle or ellipse area, and the results of the selected area are saved in a Matlab database in "*MAT*" format.

3.6 Calibration of the Polariscope and Fringe Multiplier

The fringe multiplier was calibrated in a separate experiment using the $120 \times 11 \times 0.5$ mm silicon beam sectioned from a 200 mm double-side polished CZ wafer. The background light was blocked by an opaque window placed before the first waveplate, and only the image of the beam is then visible in the camera. The polarizer, quarter waveplates and the sample are tilted at a small angle to avoid the internal reflection which may contaminate the images. The inclination of the splitter is oriented at the horizontal direction so that there is only loss in spatial resolution in the horizontal direction, which will not affect the photoelastic parameters because the stresses are uniform along the horizontal direction for a four-point bending beam. For the calibration, the spatial resolutions are 0.4, 1.3 and 2.7 mm for the fringe multiplication factors of 3, 5 and 7 respectively. This resolution can be improved to 1.0 mm in the measurement of residual stresses in thin wafers by reducing the space between the two partial mirrors. Figure 23 shows the retardation of the fringe multiplication factors of 1, 3, 5 and 7. The experimental result is not available for the fringe multiplication factor greater than 7 due to the excessive loss in the light intensity.

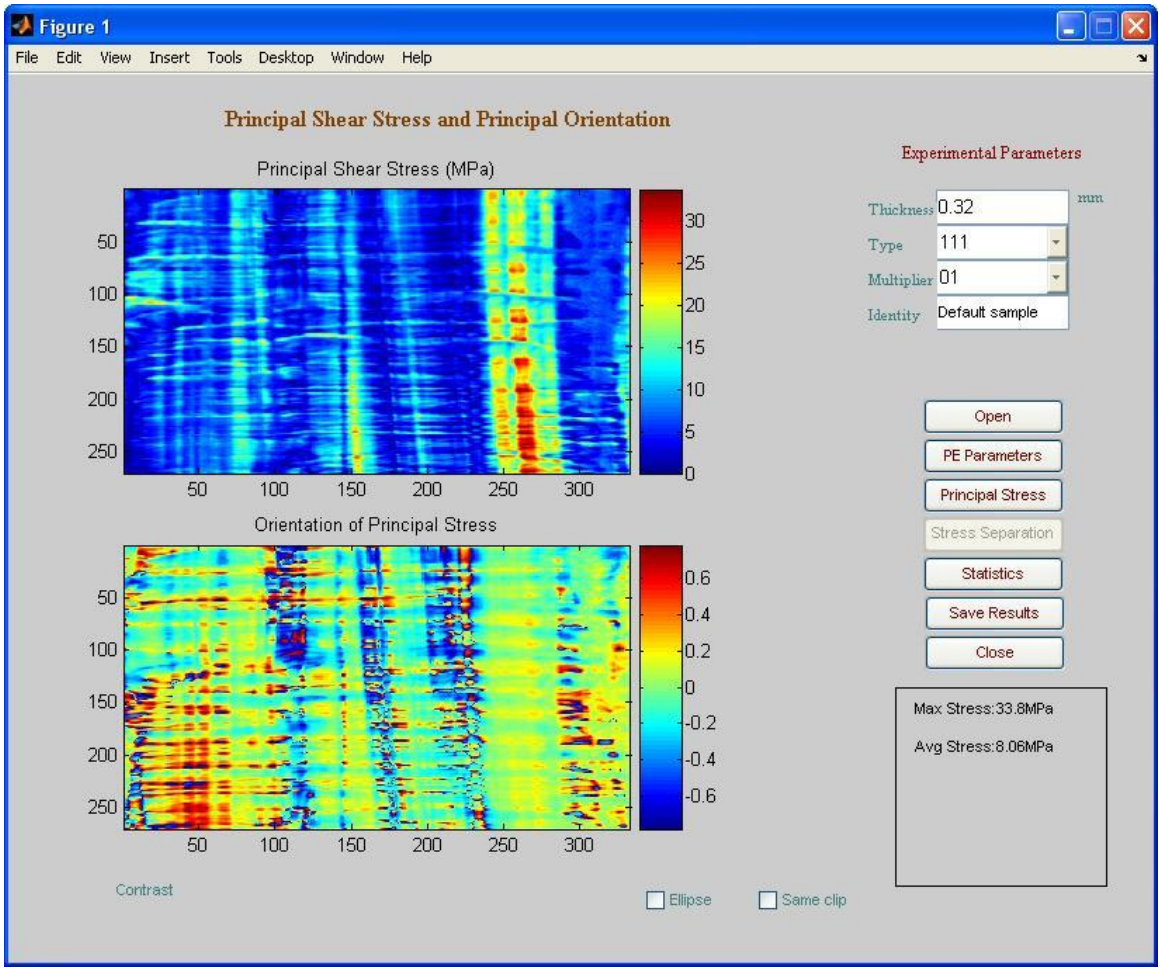

Figure 21: The interface of the program *ResidualStress* for data processing

Table 5: The slope of the retardation of different fringe multiplication factors

Multiplication factor m	Average $d\delta/dy$ (rad/mm)	Standard deviation	Normalized $\frac{d\delta/dy}{m}$
1	0.1022	0.0023	0.1022
3	0.3225	0.0050	0.1075
5	0.5133	0.0104	0.1027
7	0.7451	0.0711	0.1064

As shown in Figure 22, there is no apparent fringe in the retardation of $m = 1$. With the increase of the fringe multiplication, the contrast of the images becomes stronger, and almost one complete fringe is observed in the images of $m = 7$. However, unwrapping is not necessary because the Equation 9 extends the range of retardation to $[-\pi, \pi]$.

The retardation of the four different multiplications, as shown in Figure 23, remains uniform along the horizontal direction and linear along the transverse direction. Figure 24 shows the distribution along the transverse direction at randomly chosen cross section. The linear least-square fit along the transverse direction was used to evaluate the results. Table 5 shows the averages of the slopes and their standard deviations of the four different fringe multiplication factors. The average slope of $m = 1$ is the same as that without the fringe multiplier. The retardation increases with the increase of the fringe multiplication factor. The normalized slopes, $\frac{d\delta/dy}{m}$, of the four different multiplication factors are within an error of 5%. As shown in Figure 25, with the increase of the fringe multiplication factor, the standard deviation of the slope also increases. The main reason for this is that the error and noise in the system are also amplified by the fringe multiplier. However, the normalized deviations are almost the same, which shows that the fringe multiplier does not introduce an extra error to the final results.

3.7 Conclusions

The experimental setup of the polariscope was described. The loss in light intensity and spatial resolution of the fringe multiplier was analyzed. An arrange was introduced to

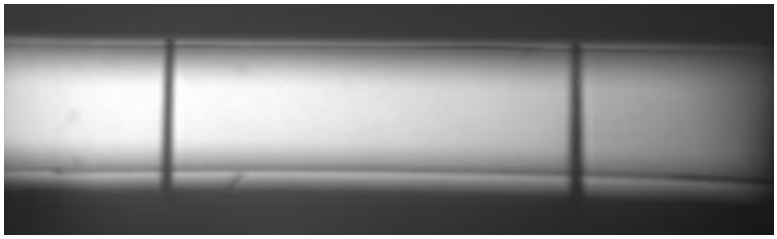

(a) $m = 1$

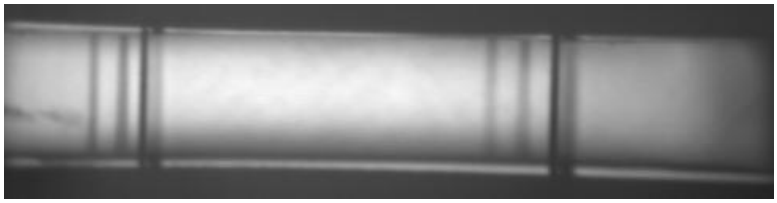

(b) $m = 3$

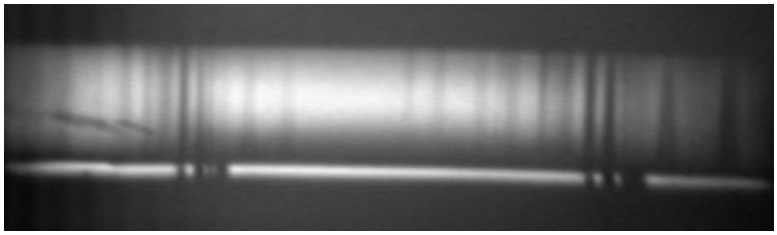

(c) $m = 5$

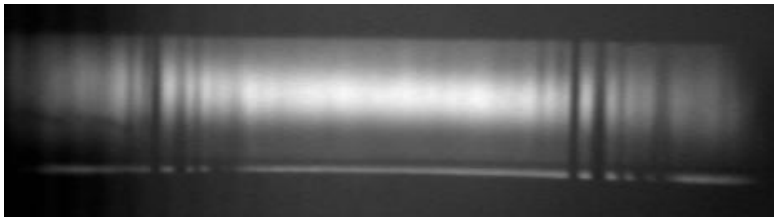

(d) $m = 7$

Figure 22: Images in the phase-stepping of different fringe multiplication factors

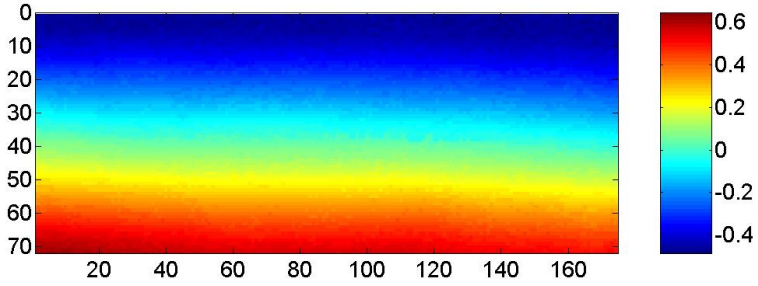

(a) $m = 1$

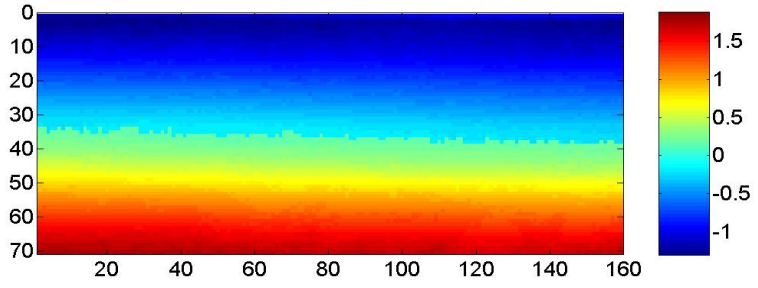

(b) $m = 3$

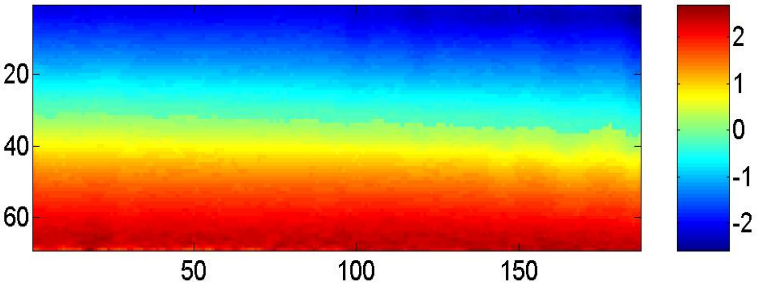

(c) $m = 5$

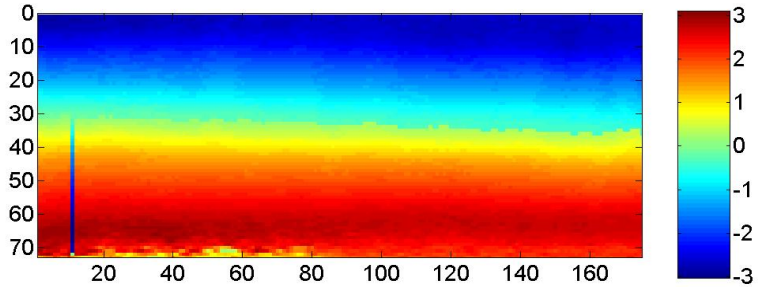

(d) $m = 7$

Figure 23: Phase retardation of different fringe multiplication factors

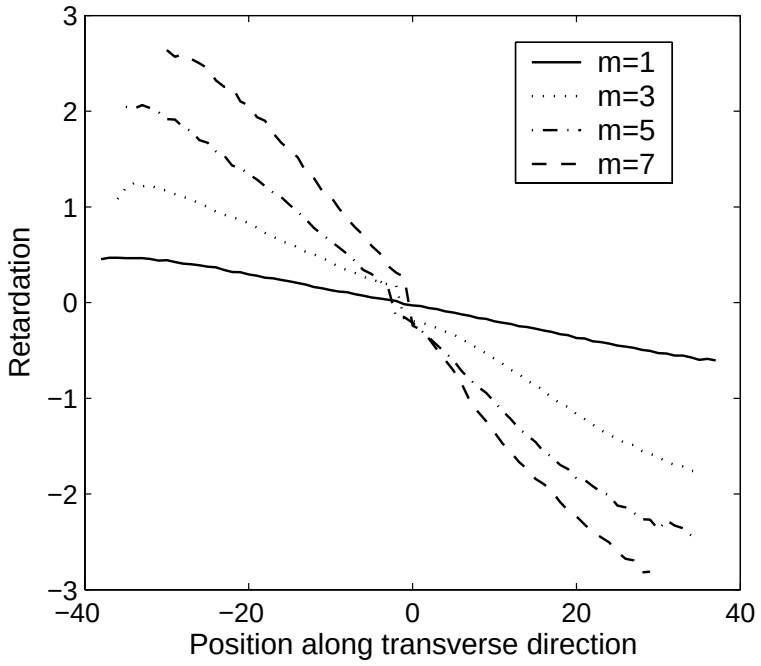

Figure 24: The randomly selected line scans along transverse direction of the retardation of different multiplication factors ($m = 1, 3, 5, 7$)

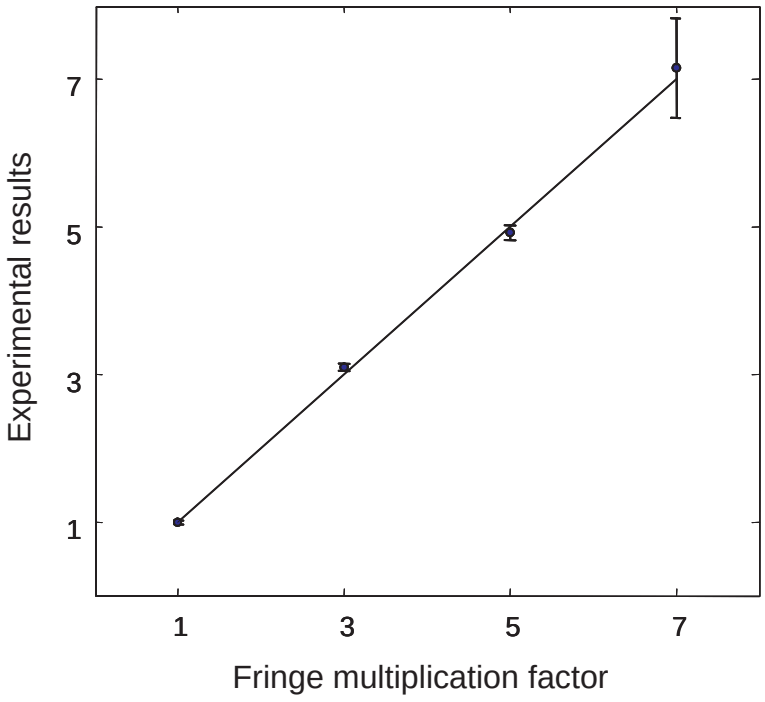

Figure 25: The experimental results for different fringe multiplication factors, solid line shows the ideal fringe multiplier

minimized the loss in the spatial resolution of the four-point bending. The polariscope and fringe multiplier was calibrated. A new algorithm of phase-stepping was introduced to extend the range of the retardation from $[0, \pi]$ to $[0, 2\pi]$ to eliminate the possibility for phase unwrapping in the residual stress measurement.

CHAPTER IV

ERROR ANALYSIS

4.1 Summary

This chapter summarizes the analysis of the systematic and random errors in the circularly polarized phase-stepping polariscope. The sources of error analyzed consist of the misalignment of the optical elements and the error in the image digitization. The results show that the error in stress is approximately 1.0 MPa and the error in the orientation of the stress can be ignored except in the undefined regions. The systematic misalignment in the polarizer and two quarter waveplates was rectified before analysis.

4.2 Introduction

Traditional polariscopy is usually used for a specimen with a thickness of the order of millimeters and stress level of 100 MPa, where multiple fringes can be observed and phase unwrapping is required to remove the discontinuity in the phase. The error, which is of the order of a fractional fringe, is negligible compared with multiple fringes. However, for a typical photovoltaic silicon wafer with a thickness less than 300 μm and stress level around 10 MPa, only a partial fringe can be observed, and the error analysis is therefore crucial to determining the system realiability.

The errors associated with wavelength mismatch of the quarter waveplates and nominal inclination of the optical elements have been analyzed by Patterson [36, 40]. His results show that the maximum error is of the order of 0.012 fringe order. In the chapter, the wavelength mismatch is not considered because the relatively narrow bandwidth (10 nm) of the monochromatic light obtained using the bandpass filter. The main error sources analyzed are the angular misalignment in the two waveplates and the two polarizers, and the digitization error in the image grabber.

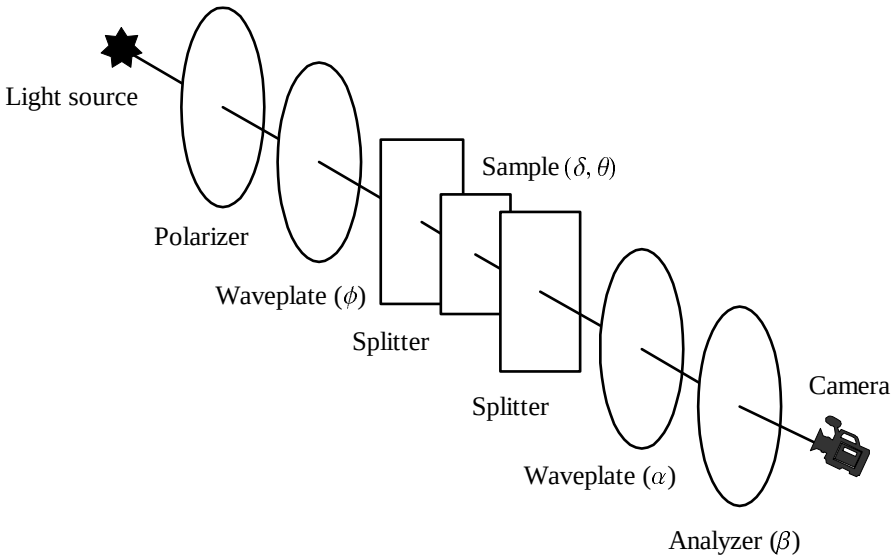

Figure 26: The experimental setup of the infrared residual stress polariscope

4.3 Theory of light propagation in Polariscope

As shown in Figure 26, the near infrared (NIR) polariscope consists of a narrow band filter, two polarizers, two waveplates, two lenses and a digital camera. The light propagation polariscope can be described by the Stokes vector and Mueller matrix [68]. For a light beam propagating along z direction (Figure 27), the electrical field can be decomposed along the x and y directions,

$$E_x = E_{0x}\left[\cos\left(\frac{2\pi}{\lambda}z - \omega t\right) + \delta_x\right] \tag{11a}$$

$$E_y = E_{0y}\left[\cos\left(\frac{2\pi}{\lambda}z - \omega t\right) + \delta_y\right] \tag{11b}$$

where E_x, E_y are the magnitude of the electrical field along x and y axes respectively, δ_x, δ_y are the phases, ω is the frequency, λ is the wavelength and t is time. The relative retardation, δ, between E_x and E_y is $\delta_x - \delta_y$. This light can also be expressed by Stokes vector without losing any information,

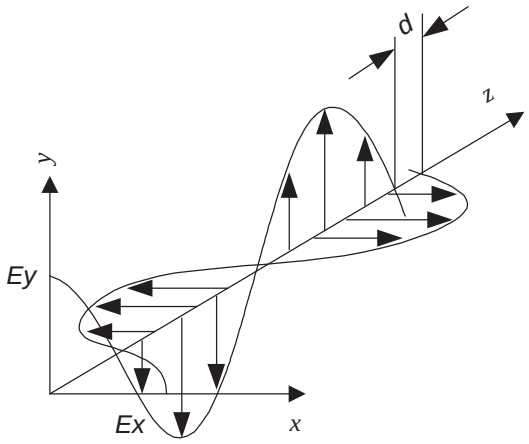

Figure 27: A light beam with an electrical field E_x and E_y propagating along z direction

$$\boldsymbol{S} = \begin{Bmatrix} s_0 \\ s_1 \\ s_2 \\ s_3 \end{Bmatrix} \tag{12}$$

where

$$s_0 = E_{x0}^2 + E_{y0}^2 \tag{13a}$$

$$s_1 = E_{x0}^2 - E_{y0}^2 \tag{13b}$$

$$s_2 = 2E_{x0}E_{y0}\cos\delta \tag{13c}$$

$$s_3 = 2E_{x0}E_{y0}\sin\delta \tag{13d}$$

As shown in above equation, the first component s_0 is the light intensity, and the other three components describe the phase. The four components are not independent, and satisfy $s_0^2 = s_1^2 + s_2^2 + s_3^2$. For a randomly polarized light beam, the Stokes vector $\boldsymbol{S}$ is given as,

$$\boldsymbol{S}_0 = I_a[1, 0, 0, 0]^T \tag{14}$$

where T represents matrix transpose, and I_a is the light intensity. An ideal linear polarizer is described by the Mueller matrix $\boldsymbol{P}(\beta)$,

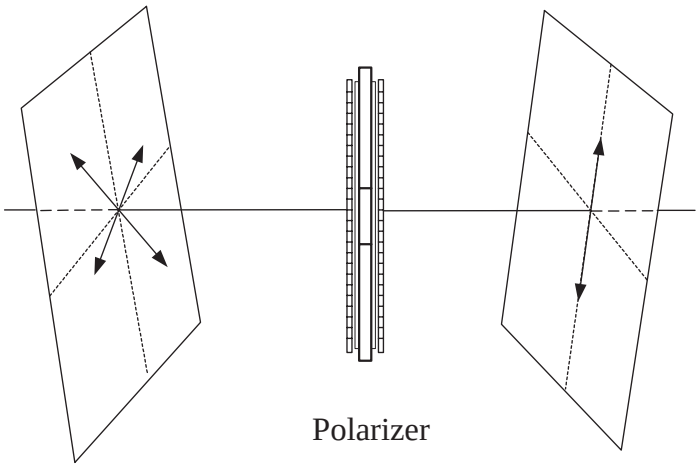

Figure 28: Light propagation through a linear polarizer

$$\boldsymbol{P}(\beta) = \begin{bmatrix} 1 & \cos 2\beta & \sin 2\beta & 0 \\ \cos 2\beta & \cos^2 2\beta & \sin 2\beta \cos 2\beta & 0 \\ \sin 2\beta & \sin 2\beta \cos 2\beta & \sin^2 2\beta & 0 \\ 0 & 0 & 0 & 0 \end{bmatrix} \tag{15}$$

where β is the angle between the principal axis of the polarizer and the reference axis. The specimen and quarter waveplates can be considered as phase retarders, which can be described by a Mueller matrix as,

$$\boldsymbol{M}(\theta, \delta) = \begin{bmatrix} 1 & 0 & 0 & 0 \\ 1 & \cos^2 2\theta + \sin^2 2\theta \cos\delta & (1 - \cos\delta) \sin 2\theta \cos 2\theta & \sin 2\theta \sin\delta \\ 1 & (1 - \cos\delta) \sin 2\theta \cos 2\theta & \sin^2 2\theta + \cos^2 2\theta \cos\delta & -\cos 2\theta \sin\delta \\ 0 & -\sin 2\theta \sin\delta & \cos 2\theta \sin\delta & \cos\delta \end{bmatrix} \tag{16}$$

where θ is the angle between the principal axis of the quarter waveplate and the reference axis, and δ is the retardation. For an ideal quarter waveplate without wavelength mismatch,

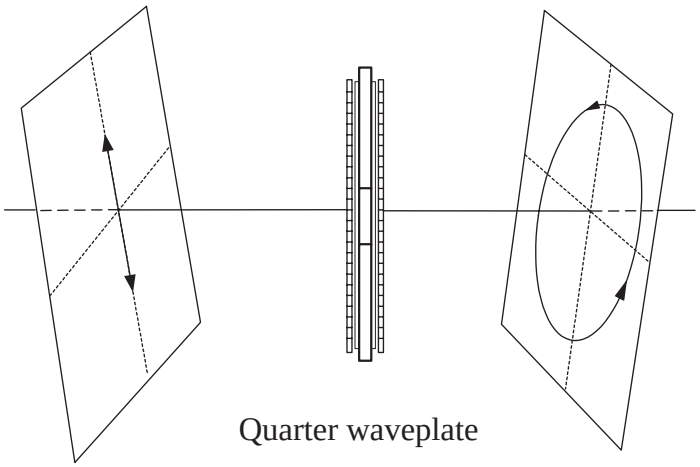

Figure 29: Light propagate through a quarter waveplate

$\delta = \pi/2$, the Mueller matrix is,

$$\boldsymbol{M}\left(\theta, \frac{\pi}{2}\right) = \begin{bmatrix} 1 & 0 & 0 & 0 \\ 1 & \cos^2 2\theta & \sin 2\theta \cos 2\theta & \sin 2\theta \\ 1 & \sin 2\theta \cos 2\theta & \sin^2 2\theta & -\cos 2\theta \\ 0 & -\sin 2\theta & \cos 2\theta & 0 \end{bmatrix} \tag{17}$$

A circular polariscope as shown in Figure 26 can be analyzed by the concatenation of the Mueller matrices.

$$\boldsymbol{S} = \boldsymbol{S}_m + \boldsymbol{P}(\beta)\,\boldsymbol{M}\left(\alpha, \frac{\pi}{2}\right)\boldsymbol{M}(\theta, \delta)\,\boldsymbol{M}\left(\phi, \frac{\pi}{2}\right)\boldsymbol{P}(0)\boldsymbol{S}_0 \tag{18}$$

where $\boldsymbol{S}_m$ accounts for the background light. $\boldsymbol{P}(0)$ and $\boldsymbol{P}(\beta)$ are the polarizer and analyzer respectively. $\boldsymbol{M}(\phi, \pi/2)$, $\boldsymbol{M}(\theta, \delta)$ and $\boldsymbol{M}(\alpha, \pi/2)$ are the first waveplate, the specimen and the second waveplate respectively. The phase-stepping technique discussed in Chapter 3 can also be described by the Mueller matrices,

$$\boldsymbol{S}_1 = \boldsymbol{S}_m + \boldsymbol{P}(0)\boldsymbol{M}\left(\frac{\pi}{4},\frac{\pi}{2}\right)\boldsymbol{M}(\theta,\delta)\boldsymbol{M}\left(\frac{\pi}{4},\frac{\pi}{2}\right)\boldsymbol{P}(0)\boldsymbol{S}_0 \tag{19a}$$

$$\boldsymbol{S}_2 = \boldsymbol{S}_m + \boldsymbol{P}(0)\boldsymbol{M}\left(\frac{\pi}{4},\frac{\pi}{2}\right)\boldsymbol{M}\left(\theta,\delta\right)\boldsymbol{M}\left(-\frac{\pi}{4},\frac{\pi}{2}\right)\boldsymbol{P}(0)\boldsymbol{S}_0 \tag{19b}$$

$$\boldsymbol{S}_3 = \boldsymbol{S}_m + \boldsymbol{P}(0)\boldsymbol{M}\left(\frac{\pi}{4},\frac{\pi}{2}\right)\boldsymbol{M}\left(\theta,\delta\right)\boldsymbol{M}\left(0,\frac{\pi}{2}\right)\boldsymbol{P}(0)\boldsymbol{S}_0 \tag{19c}$$

$$\boldsymbol{S}_4 = \boldsymbol{S}_m + \boldsymbol{P}(0)\boldsymbol{M}\left(\frac{\pi}{4},\frac{\pi}{2}\right)\boldsymbol{M}\left(\theta,\delta\right)\boldsymbol{M}\left(\frac{\pi}{4},\frac{\pi}{2}\right)\boldsymbol{P}\left(\frac{\pi}{4}\right)\boldsymbol{S}_0 \tag{19d}$$

$$\boldsymbol{S}_5 = \boldsymbol{S}_m + \boldsymbol{P}(0)\boldsymbol{M}\left(\frac{\pi}{4},\frac{\pi}{2}\right)\boldsymbol{M}\left(\theta,\delta\right)\boldsymbol{M}\left(\frac{\pi}{2},\frac{\pi}{2}\right)\boldsymbol{P}\left(\frac{\pi}{2}\right)\boldsymbol{S}_0 \tag{19e}$$

$$\boldsymbol{S}_6 = \boldsymbol{S}_m + \boldsymbol{P}(0)\boldsymbol{M}\left(\frac{\pi}{4},\frac{\pi}{2}\right)\boldsymbol{M}\left(\theta,\delta\right)\boldsymbol{M}\left(\frac{3\pi}{4},\frac{\pi}{2}\right)\boldsymbol{P}\left(\frac{3\pi}{4}\right)\boldsymbol{S}_0 \tag{19f}$$

The intensity of the six images in the phase stepping are the first components in the Stokes vectors, e.g. $I_i = S_{i,1}$, $i = 1 \cdots 6$. The sequence of simultaneous equations is solved for the relative retardation δ and the isoclinic angle θ.

4.4 The Rectification of the Optic Elements

There are mainly two types of error in photo-stepping photoelasticity, namely those associated with the optical elements and those associated with the image process devices such as the camera, the CCD array and the image digitizer.

Angular misalignments of the two waveplates and polarizers are the most dominant error associated with these optical elements. The systematic misalignment in the optic elements is first corrected before any measurement. Then, both systematic and random errors in the misalignment will be analyzed. The minimum angular misalignment is assumed to be one degree, or half of the minimum scale of the rotation stages.

4.4.1 Rectification of the polarizer and analyzer

The alignment of the polarizer and analyzer pair was check by the setup shown in Figure 30. The polarizer was fixed at 0°, and the analyzer was rotated from 0°to 360°with a step of 5°. The theoretical emerging light is describe by the Mueller matrices as,

$$\boldsymbol{S} = \boldsymbol{P}(\theta)\boldsymbol{P}(0)\boldsymbol{S}_0 \tag{20}$$

and the emerging light is

$$I = I_0 + I_a \sin(\theta) \tag{21}$$

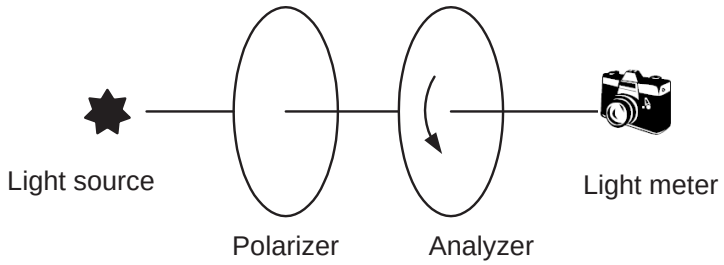

Figure 30: The setup to check the misalignment in the polarizer and analyzer

The emerging light was measured by a light meter and the result is shown in Figure 31(a). In the figure, the solid and dashed lines show the experimental and ideal results respectively. The offset between these two curves reveal the misalignment in the analyzer. The amount of the offset was determined by the cross correlation between the experimental and ideal curves shown in Figure 32. The optimal value of the offset is found at the location with the maximum cross correlation coefficient. The misalignment in the polarizer and analyzer pair was found to be 4°. The light intensity after correction is shown in Figure 31(b). The experimental and ideal curves in the figure are coincide exactly with each other and thus the misalignment is largely rectified.

4.4.2 Rectification of the two quarter waveplates

The first polarizer and waveplate pair is used to generate the circularly polarized input light, and any misalignment will deteriorate the quality of the circular polarization and generate elliptically polarized light instead. The alignment of the quarter waveplates was check by the setup shown in Figure 33, in which the polarizer and analyzer were crossed and the quarter waveplate was rotated from 0°to 360°with a step of 5°. This setup can be described by Mueller matrices,

$$\boldsymbol{S} = \boldsymbol{S}_0 + \boldsymbol{P}\left(\frac{\pi}{2}\right)\boldsymbol{M}\left(\theta, \frac{\pi}{2}\right)\boldsymbol{P}(0) \tag{22}$$

where θ=0, 5°, $\cdots$, 360°. The intensity is

$$I = I_0 + I_a(1 - \cos^2\theta) \tag{23}$$

The intensity of the emerging light is shown in Figure 34(a) and 36(a) for the first and second quarter waveplate respectively. In the figures, the solid and dashed lines show the

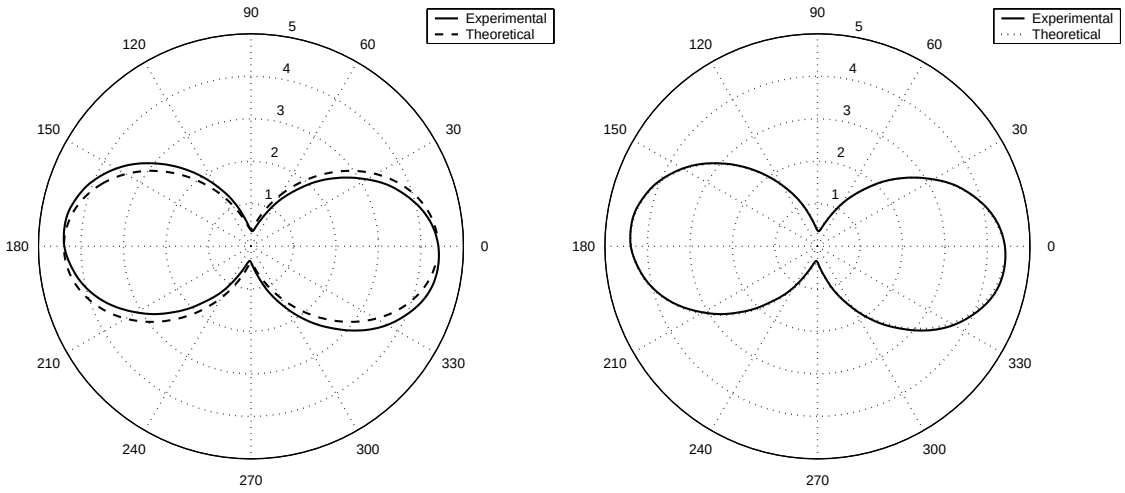

(a) (b)

Figure 31: The test of the misalignment in the polarizer and analyzer pair. (a) the offset between the dashed line (theoretical) and solid line (measured) shows the misalignment in the analyzer. (b) the theoretical and measured results coincide after rectification

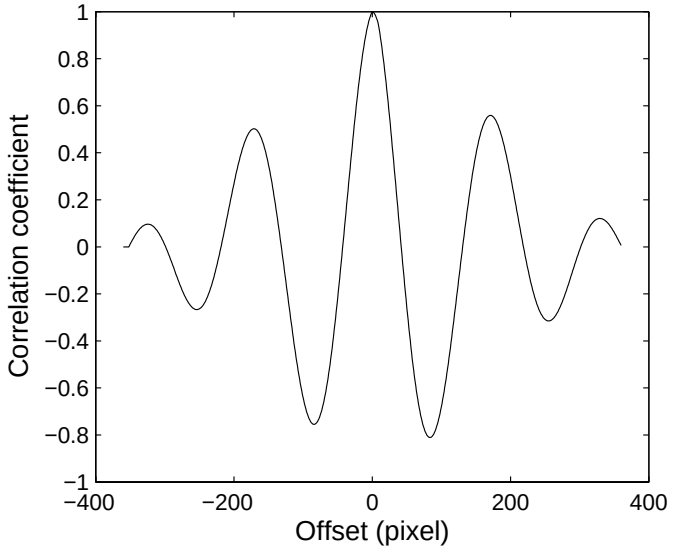

Figure 32: The coefficient of the cross correlation between the theoretical and measured light intensities

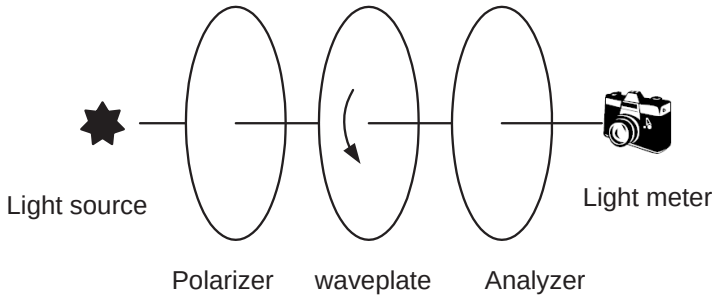

Figure 33: The setup to check the misalignment the two quarter waveplates

experimental and ideal results respectively. The offset between the two curves are observed in both figures. The coefficients of the cross correlation are shown in Figure 35 and 37 respectively. The optimal value of the offset is found in the same way, and the misalignments was found to be 2°and 3°for the first and second quarter waveplate respectively. The light intensity after correction is shown in Figure 34(b) and 36(b). The experimental and ideal curves in the figures are coincide exactly with each other and thus the misalignments are largely rectified.

4.5 Systematic and Random Error Analysis

4.5.1 Error in the first waveplate

There is a only systematic error in the first quarter waveplate because it is fixed during phase stepping. The error of the misalignment can be analyzed by introducing a small offset $\Delta\phi$, which is assumed to be 1°, in the angular position in Equation 18. The analysis is too complicated to be handled manually, and the software *Maple* is used to deal with the complexity. In this case the transmitted light is given by

$$\boldsymbol{S_i} = \boldsymbol{P}(\beta_i)\boldsymbol{M}(\alpha_i, \frac{\pi}{2})\boldsymbol{M}(\theta, \delta)\boldsymbol{M}(\frac{\pi}{4} + \Delta\phi, \frac{\pi}{2})\boldsymbol{P}(0)\boldsymbol{S}_0 \tag{24}$$

where α_i, β_i $(i = 1 \cdots 6)$ are the six positions defined in Table 4. The above equations are substituted in Equations (8, 9) and the photoelastic parameters are obtained. As shown in Figure 38, the error is a function of the photoelastic parameters. The isoclinic angle exhibits negligible error except in the undefined regions where the fringe order is integral. In these regions, the isoclinic angle will oscillate between $-\pi/2$ and $\pi/2$, which may introduce

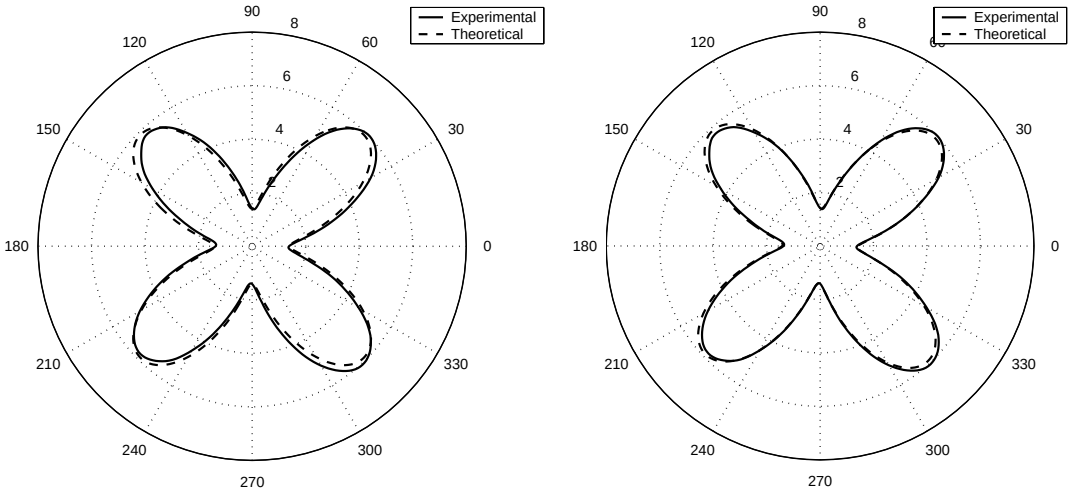

Figure 34: The test of the misalignment in the *first* quarter waveplates. (a) the offset between the dashed line (theoretical) and solid line (measured) shows the misalignment in the *first* quarter waveplate. (b) the theoretical and measured results coincide after rectification

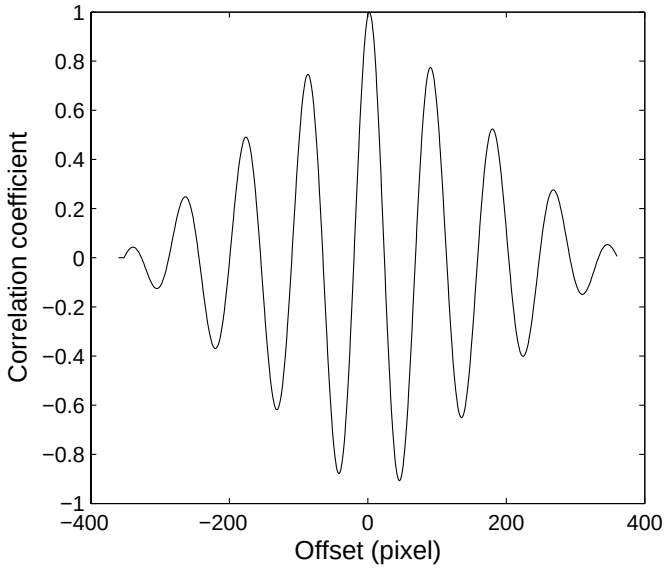

Figure 35: The coefficient of the cross correlation between the theoretical and measured light intensities (*first* quarter waveplate)

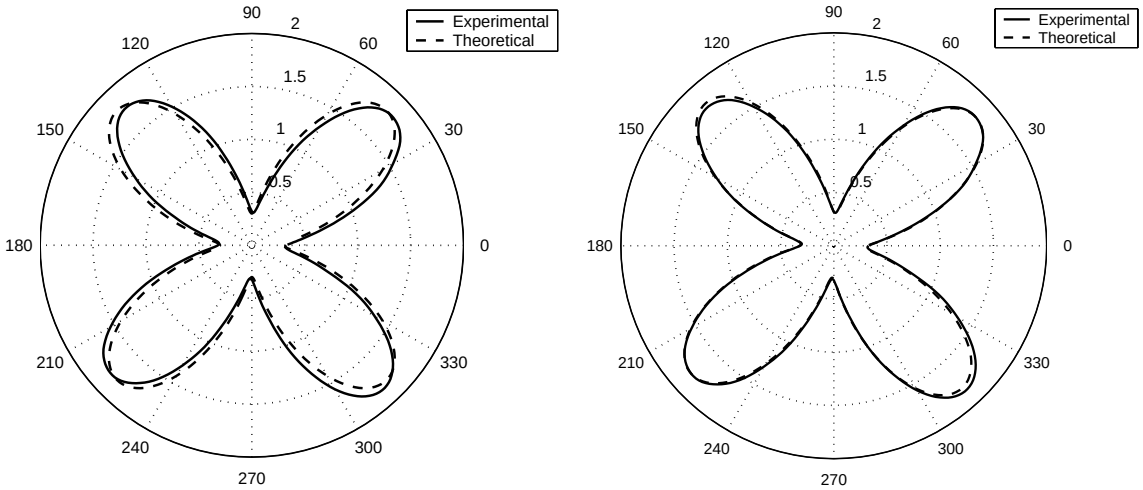

Figure 36: The test of the misalignment in the *second* quarter waveplates. (a) the offset between the dashed line (theoretical) and solid line (measured) shows the misalignment in the *second* quarter waveplate. (b) the theoretical and measured results coincide after rectification

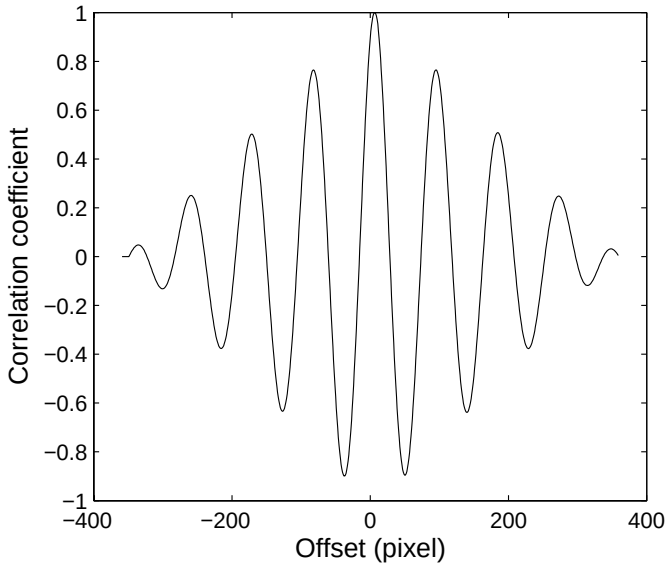

Figure 37: The coefficient of the cross correlation between the theoretical and measured light intensities (*second* quarter waveplate)

ambiguity in phase unwraping. However, this is not a problem for the measurement of in-plane residual stress in silicon because of the low stress levels.

The maximum error in the isochromatic retardation is about 0.004 fringe/degree, or 0.4 MPa/degree for a typical wafer. This value reaches it's maximun when $\theta = 0, \pi/2$, and remains almost constant with the variance of real retardation. This misalignment will shift the stress vertically in the four-point bending experiment since it has a constant isoclinic angle.

4.5.2 Error in the second waveplate

Unlike the first waveplate, both systematic and random errors are present in the misalignment of the second waveplate. The systematic error is derived in the same way as the first. The analytical expression can also be obtained by a Taylor expansion. The systematic error in the retardation is given as

$$\Delta\delta = 2\Delta\alpha \sin 2\theta \sin^2 \delta \tag{25}$$

For a typical photovoltaic sample, the maximum retardation is around 0.8 rad, and the maximum error is about 0.007 fringe, or 0.7 MPa in terms of stress. The distribution of the systematic error is shown in Figure 39. The systematic error in the isoclinic angle of the second waveplate is constant and equals the amount of misalignment, $\Delta\alpha$.

The random error can be analyzed in the same way. The difference is that the misalignments are independent in each step of the phase stepping, so the light intensities of the six images are given by

$$\boldsymbol{S_i} = \boldsymbol{P}(\beta_i)\boldsymbol{M}(\alpha_i + \Delta\alpha_i, \frac{\pi}{2})\boldsymbol{M}(\theta, \delta)\boldsymbol{M}(\frac{\pi}{4}, \frac{\pi}{2})\boldsymbol{P}(0)\boldsymbol{S}_0 \tag{26}$$

The errors can be obtained through the theory of error propagation.

$$\Delta\delta = \sqrt{\sum_{i=1}^{6}\left(\frac{\partial\delta}{\partial\alpha_i}\Delta\alpha_i\right)^2} \qquad \Delta\theta = \sqrt{\sum_{i=1}^{6}\left(\frac{\partial\theta}{\partial\alpha_i}\Delta\alpha_i\right)^2} \tag{27}$$

The random error can be obtained by substituting Equation 26 into the Equation 27. For simplicity, the maximum uncertainty in the alignment is assumed to be 1°. It is worth

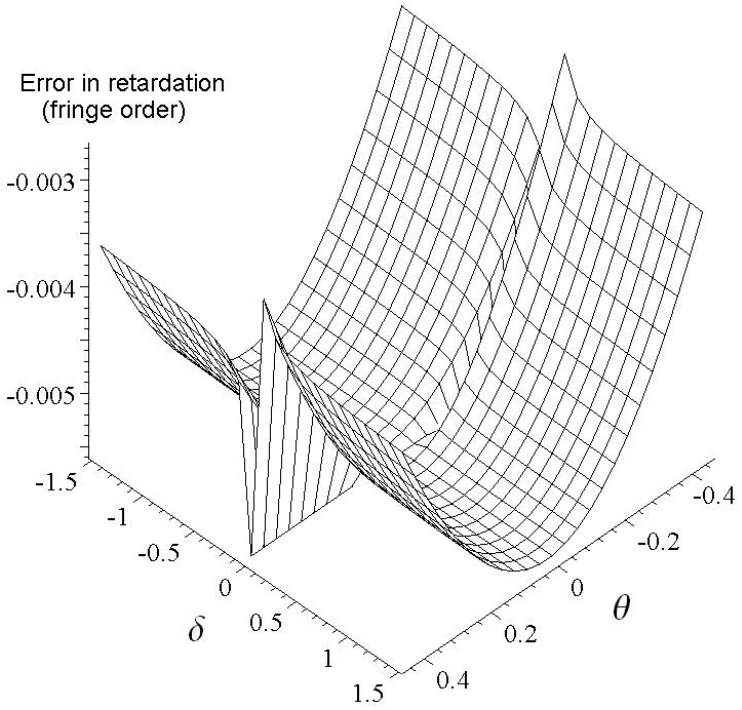

(a) Error in the retardation

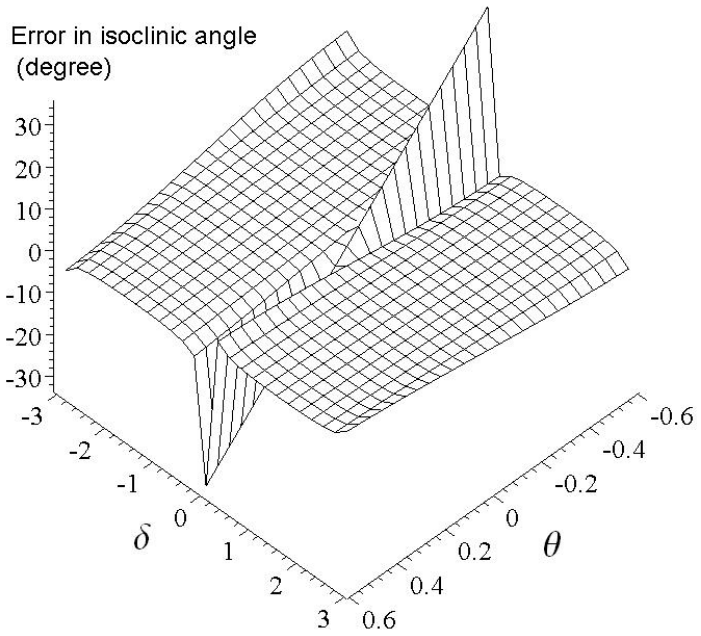

(b) Error in the isoclinic angle

Figure 38: Systematic error in the first quarter waveplate with a misalignment of 1°

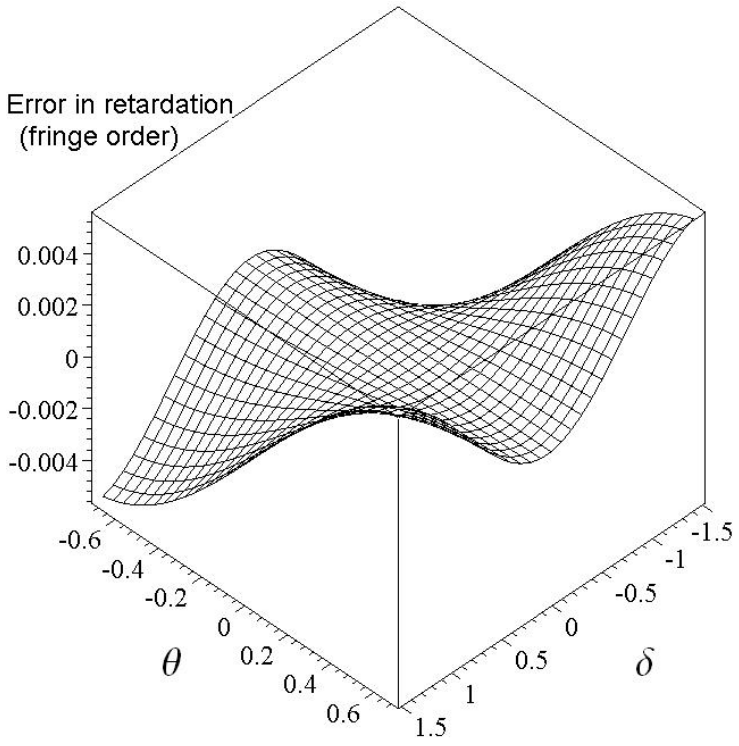

Figure 39: The systematic error in the retardation of the second quarter waveplate with a misalignment of 1°. The error in isoclinic angle is constant.

pointing out that there are only three rotations of the second waveplate. Figure 39 and 40 show the distribution of the systematic and random errors respectively. Again, it is found that the error in the isoclinic angle is small except in the undefined regions. On the other hand, the random error in the isochromatic retardation reaches its maximum in the undefined region, while the systematic error is zero.

4.5.3 Error in the analyzer

The error due to the analyzer also contains two parts: a systematic error and a random error. They are analyzed exactly in the same way as the second waveplate. The systematic error in the retardation is the same as that of the second waveplate shown in Figure 39. As shown in Figure 41, the random error in isochromatic parameter is close to that of the second waveplate, but not exactly the same. The maximum error is a little larger than that caused by the second waveplate.

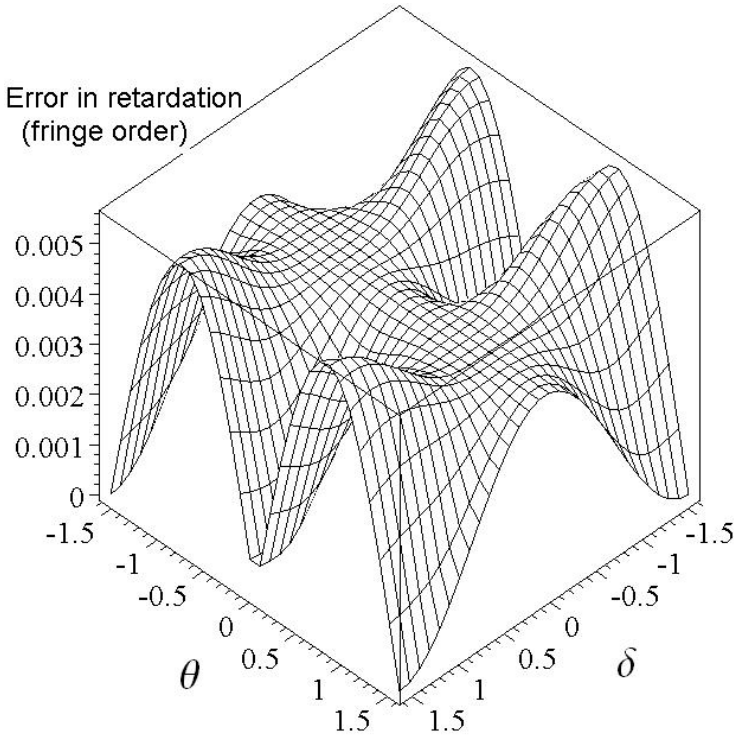

(a) Error in the retardation

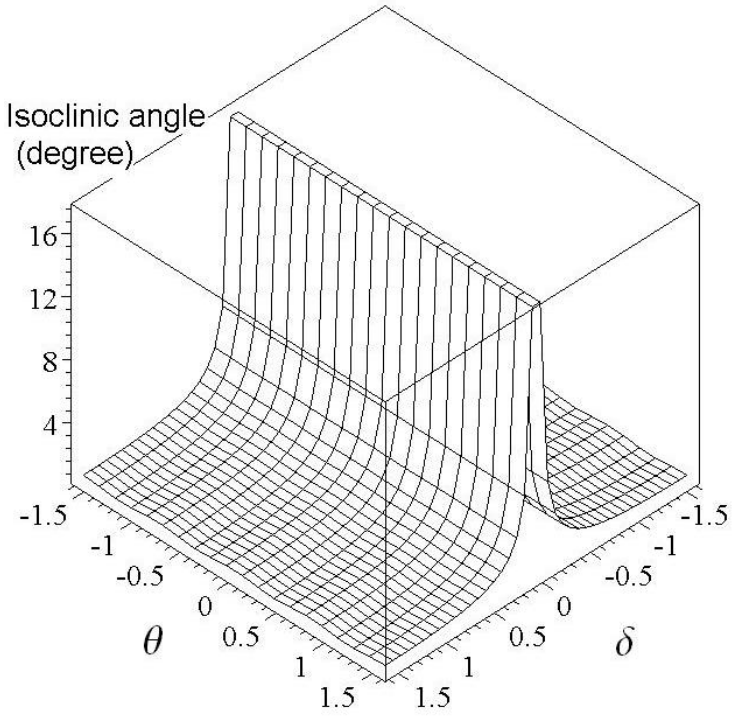

(b) Error in the isoclinic angle

Figure 40: The distribution of the random error due to the misalignment of the second waveplate

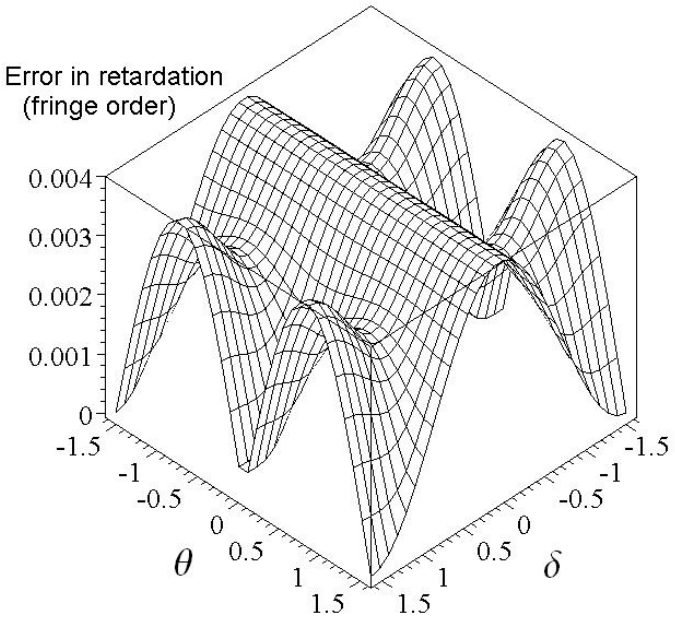

(a) Error in the retardation (fringe)

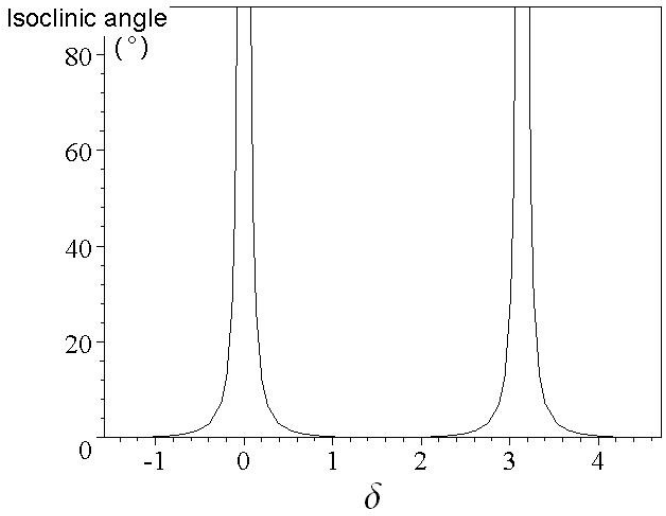

(b) Error in the isoclinic angle (°)

Figure 41: The distribution of the random error due to the misalignment of the analyzer

Table 6: The maximum error of the retardation in the optical elements with the misalignment of 1°

Optical elements	systematic error (rad)	random error (rad)
1st $\lambda/4$	N/A	0.004
2nd $\lambda/4$	0.007	0.005
analyzer	0.007	0.004
Combined	0.01	

4.5.4 Combined error of the misalignment in the optical elements

The sources of error considered here consist of: the angular misalignment of the two waveplates and the polarizer, the wavelength mismatch of the two waveplates, and digitization error. The combined error is the sum of these errors as is known from the theory of error propagation. As shown in Figure 42(a), the maximum error in stress is approximately 1.0 MPa. The two peaks in this figure show the instability in the undefined regions. The combined error in isoclinic angle shown in Figure 42(b) is negligible except in the undefined regions.

4.5.5 Error in the image digitization

In the phase-stepping, the images are captured by a CCD camera and then converted to digital signals. The main sources of error in the digital image are electronic noise and digitization error. The electronic noise can be reduced by averaging multiple images, normally over thirty images. The digitization error usually is considered to be one gray level. The error in the photoelastic parameters can be expressed as

$$\Delta\delta = \sqrt{\sum_{i=1}^{6}\left(\frac{\partial\delta}{\partial I_i}\Delta I_i\right)^2} \qquad \Delta\theta = \sqrt{\sum_{i=1}^{6}\left(\frac{\partial\theta}{\partial I_i}\Delta I_i\right)^2} \tag{28}$$

The intensities of phase-stepping are given in Table 4. By substituting the light intensities into Equation 28, the errors can be obtained as

$$\Delta\delta = \frac{1}{\sqrt{2}} I_a \tag{29}$$

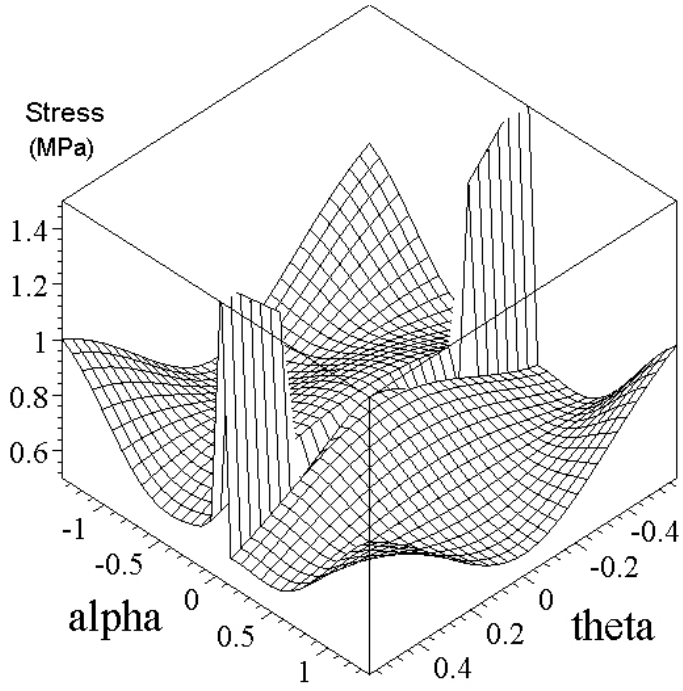

(a) Error in the stress (MPa)

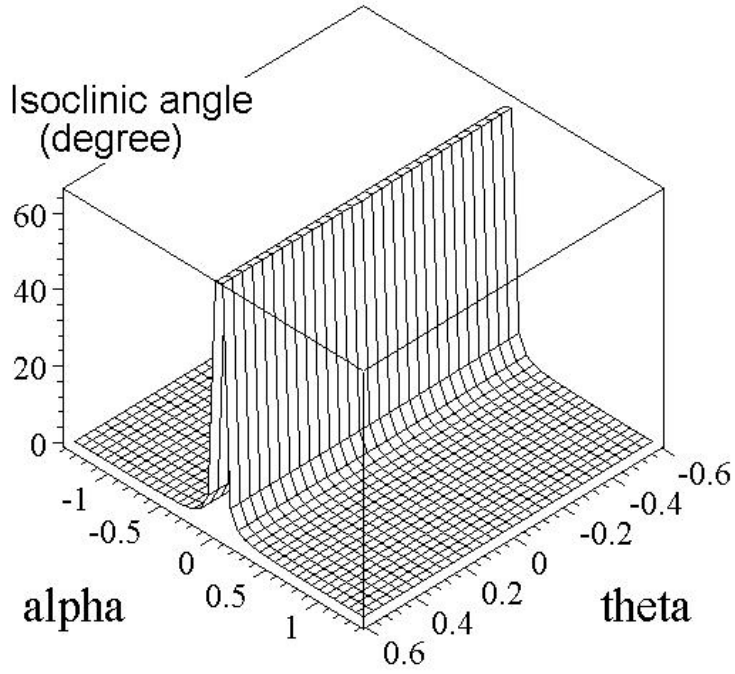

(b) Error in the isoclinic angle (°)

Figure 42: The combined error due to the misalignment of all optical elements

and

$$\Delta\theta = \frac{1}{2\sqrt{2}} I_a \sin\delta \tag{30}$$

where $I_a = \sqrt{(I_1 - I_2)^2 + (I_4 - I_4)^2 + (I_5 - I_3)^2}/2$ is the effective contrast of the images. As shown in Equation 14, both errors are inversely proportional to the effective contrast. For a typical measurement, the range of I_a is between 20 to 35, which means the error of retardation is between 0.03 and 0.05 of a fringe order, or 0.3 MPa to 0.5 MPa. The error of the isoclinic parameter is still small except in the undefined region.

In the six-step phase-stepping, the effective contrast is dominated by the first two images: the bright field and the dark field. A 8-bit digital camera has 255 gray levels. The background light I_m consumes the space of gray levels and leaves not enough space for image contrast. The error can be reduced by carefully blocked the background light with an opaque window and/or turning the light in the lab.

4.6 Conclusion

The systematic and random errors caused by the angular misalignment of the two wave-plates, the analyzer and the image digitization in a phase-stepping polariscope were analyzed. In all these cases, the error in the isoclinic angle can be ignored except in the undefined regions. The error in the phase retardation varies with the real photoelastic parameters, and the maximum error caused by all these sources combined is within 1.2 MPa.

CHAPTER V

THE ANALYSIS OF THE ANISOTROPY IN SILICON

5.1 Summary

This chapter summarizes the analysis of the stress-optic coefficients. The anisotropy in crystal silicon will be considered and the coefficients of (001), (011) and (111) silicon will be obtained analytically in terms of the stress-optic tensor.

5.2 Stress-optic Law of Isotropic Birefringence Materials

The application of mechanical stresses to an transparent material modifies its optical properties by the size, shape and orientation of the refractive ellipsoid. Thus, a isotropic optical material such as silicon will become optically anisotropic when subjected to stresses. This phenomenon is known as the photoelastic effect. This effect normally persists while the loads are maintained but vanishes, almost instantaneously when they are removed.

For a material with isotropic stress-optical coefficient, the principal axes of its refractive index ellipsoid at any point coincide with the principal axes of stress at that point. The relationship between the principal refractive indices and the principal stresses are expressed as the stress-optic law [24]

$$n_1 - n_2 = C(\sigma_1 - \sigma_2) \tag{31a}$$

$$n_2 - n_3 = C(\sigma_2 - \sigma_3) \tag{31b}$$

$$n_3 - n_1 = C(\sigma_3 - \sigma_1) \tag{31c}$$

The equations are for light propagation in the directions of principal stresses σ_1, σ_2 and σ_3, respectively; C is known as the relative stress-optic coefficient. The stress-optic law is [24],

$$\delta = \frac{2\pi t}{\lambda} C(\sigma_1 - \sigma_2) \tag{32}$$

5.3 Optical Properties of Anisotropic Materials

Silicon is anisotropic material when stressed. For a material with anisotropic stress-optic properties, more fundamental relations between the indices of refraction and stresses are needed to obtain the stress-optic law. The refractive indices of a given medium are defined by the direction of the wave normal and the second-order tensor known as the dielectric impermeability tensor, $\boldsymbol{\beta}$

$$\boldsymbol{\beta} = \begin{bmatrix} \beta_1 & \beta_6 & \beta_5 \\ \beta_6 & \beta_2 & \beta_4 \\ \beta_5 & \beta_4 & \beta_3 \end{bmatrix} \tag{33}$$

where β_i $(i = 1 \ldots 6)$ represents the components of the dielectric impermeability tensor. Because of the symmetry, there are only six independent components in the tensor. The dielectric impermeability tensor may also be expressed in the form of an ellipsoid. In arbitrary coordinate axes, x_1, x_2 and x_3, it has the general form

$$\beta_1 x_1^2 + \beta_2 x_2^2 + \beta_3 x_3^2 + 2\beta_4 x_2 x_3 + 2\beta_5 x_3 x_1 + 2\beta_6 x_1 x_2 = 1 \tag{34}$$

The ellipsoid defines all the components of the second order tensor, including the principal axes. If x_1, x_2, x_3 are the principal axes of the permeability tensor, then $\beta_4 = \beta_5 = \beta_6 = 0$. The above equation can be simplified as

$$\beta_1 x_1^2 + \beta_2 x_2^2 + \beta_3 x_3^2 = 1 \tag{35}$$

This equation can also be expressed in the form of refractive indices instead of impermeability, provided $\beta_1 = 1/n_1^2$, $\beta_2 = 1/n_2^2$ and $\beta_3 = 1/n_3^2$ in the principal axes, and n_1, n_2 and n_3 are the principal refractive indices.

$$\frac{x_1^2}{n_1^2} + \frac{x_2^2}{n_2^2} + \frac{x_3^2}{n_3^2} = 1 \tag{36}$$

For an isotropic optical material, $n_1 = n_2 = n_3 = n_0$, there exists no birefringence, and the index ellipsoid degenerates to a sphere. In general, cubic crystals, e.g. silicon, exhibit isotropic optical properties (Figure 43(a)), but become optically anisotropic when stressed (Figure 43(b)). For uniaxial crystals, $n_1 = n_2 \neq n_3$, and the index ellipsoid is an ellipsoid

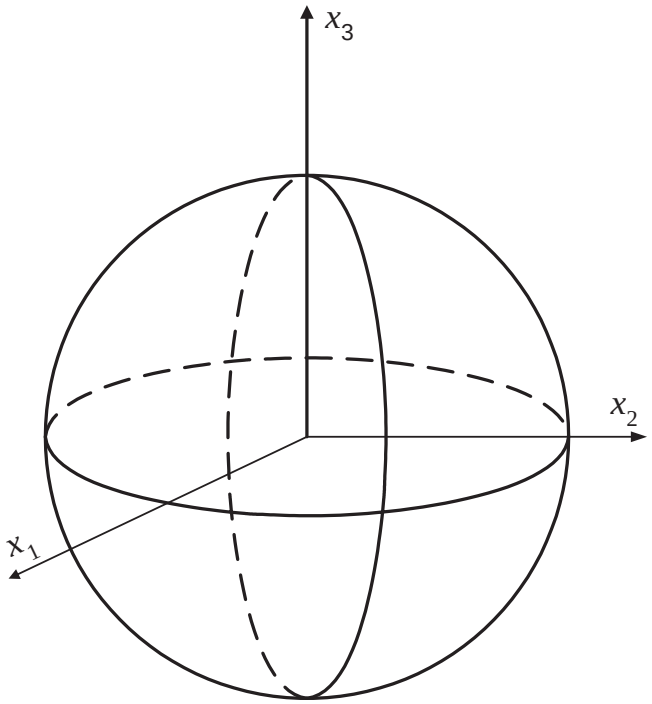

(a) Refractive index sphere of silicon before stressed

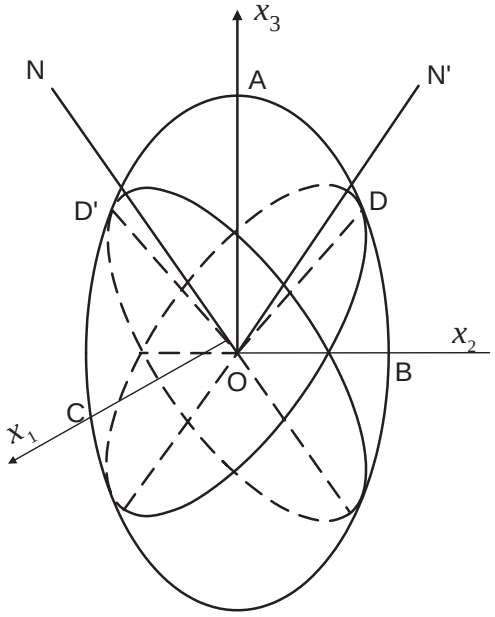

(b) Refractive index ellipsoid of silicon after stressed

Figure 43: The refractive index sphere (before stressed) and ellipsoid (stressed)

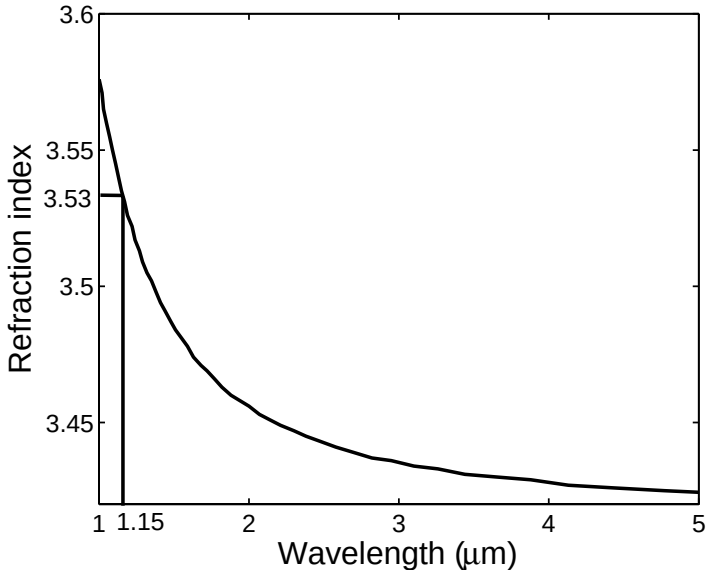

Figure 44: Refractive index of silicon at near infrared spectrum

of revolution whose principal axis is known as the optical axis. The optical axis defines the direction for which a wave traveling parallel to this axis will have no birefringence. For biaxial crystals $n_1 \neq n_2 \neq n_3$, the index ellipsoid is a triaxial ellipsoid, and there exists two optical axes for which there is no birefringence.

For silicon, the components of $\boldsymbol{\beta}$ under the stress-free condition are

$$\beta_1^0 = \beta_2^0 = \beta_3^0 = 1/n_0^2 \tag{37a}$$

$$\beta_3^0 = \beta_4^0 = \beta_5^0 = 0 \tag{37b}$$

where n_0 is the refractive index of silicon before being stressed. The refractive index of silicon in the near infrared spectrum is shown in figure 44. For $\lambda = 1.15$ μm, the refractive index is $n_0 = 3.53$.

The changes in the dielectric impermeability tensor due to stress and strain are small and are considered perturbations to the index ellipsoid. Thus, a new dielectric impermeability tensor $\Delta\boldsymbol{\beta}$, the change in impermeability, is created in the presence of a mechanical stresses, including residual stresses. This tensor normally is no longer diagonal in the stress-free principal dielectric axes. In general, changes in the dielectric impermeability tensor due

to the effects of stress or strain may be superimposed on the natural birefringence for all crystal systems. The changes in the index of refraction are, therefore, expressed as additive terms of the coefficients of the index ellipsoid equation as shown below:

$$\Delta\boldsymbol{\beta} = \boldsymbol{\beta} - \boldsymbol{\beta}^0 \tag{38}$$

where $\boldsymbol{\beta}^0$ and $\boldsymbol{\beta}$ are the impermeability tensor before and after stress respectively. For the components,

$$\Delta\beta_i = \beta_i - \beta_i^0 \qquad i = 1 \ldots 6 \tag{39}$$

When observation is made along the x_3 axes and the refractive index ellipsoid is projected on the $x_1 - x_2$ plane, the projection of the ellipsoid in equation 34 is given as

$$\beta_1 x_1^2 + \beta_2 x_2^2 + 2\beta_6 x_1 x_2 = 1 \tag{40}$$

Normally the directions of the principal stresses σ_1 and σ_2 are not the same as those of the projected ellipse. In the principal coordinate of the stresses, the deviation of the axes can be obtained as,

$$\tan 2\psi = \frac{2\beta_6}{\beta_1 - \beta_2} \tag{41}$$

where ψ is the deviation angle. By using equations 39 and 37, $\Delta\beta_6 = \beta_6$ and $\Delta\beta_1 - \Delta\beta_2 = \beta_1 - \beta_2$. The deviation angle can be expressed as,

$$\tan 2\psi = \frac{2\Delta\beta_6}{\Delta\beta_1 - \Delta\beta_2} \tag{42}$$

The retardation can also be expressed by the impermeability tensor. In the principal axes of the impermeability tensor after being stressed, the Equation 39 can be written as

$$\Delta\beta_i = \frac{1}{n_i^2} - \frac{1}{n_0^2} = \frac{(n_0 - n_i)(n_0 + n_i)}{n_0^2 n_i^2} \tag{43}$$

where n_i is the refractive index after stress is applied. Since the change of refractive index is small, $n_0 + n_i \approx 2n_0$. Then the above equation can be simplified as

$$n_i - n_0 = -\frac{n_0^3}{2}\Delta\beta_i \qquad i = 1, 2, 3 \tag{44}$$

thus

$$n_i - n_j = -\frac{n_0^3}{2}(\Delta\beta_i - \Delta\beta_j) \qquad i, j = 1, 2, 3 \tag{45}$$

Usually the parameter measured by experiment is the retardation, δ,

$$\delta = \frac{2\pi t}{\lambda}(n_1 - n_2) \tag{46}$$

where t is the thickness of the sample, λ is the wavelength of the light source. So the retardation is expressed as

$$\delta = -\frac{n_0^3 \pi t}{\lambda}(\Delta\beta_1 - \Delta\beta_2) \tag{47}$$

5.4 Anisotropy in the Stress-optic Coefficient

5.4.1 The analysis of (001) silicon

Residual stresses accentuate the anisotropy of the silicon. The stress-optic coefficient varies with the directions of observation and principal stresses. The anisotropic stress-optic coefficient can be derived from the general relation between the stress tensor and the dielectric impermeability tensor $\boldsymbol{\beta}$ [69].

$$\Delta\boldsymbol{\beta} = \boldsymbol{\pi}\boldsymbol{\sigma} \tag{48}$$

where $\boldsymbol{\pi}$ is a fourth-rank piezo-optical coefficient tensor, $\boldsymbol{\sigma}$ is the stress tensor, and $\Delta\boldsymbol{\beta}$ is the increment of the impermeability tensor $\boldsymbol{\beta}$ caused by stress. Due to the cubic symmetry of silicon, in the [100], [010] and [001] coordinate system, $\boldsymbol{\pi}$ can be expressed as a 6×6 matrix after reducing its subscripts, and $\boldsymbol{\sigma}$, $\Delta\boldsymbol{\beta}$ can be expressed in the reduced form by a 6×1 matrixes, then Equation 48 is expressed in matrix form as:

$$\begin{bmatrix} \Delta\beta_1 \\ \Delta\beta_2 \\ \Delta\beta_3 \\ \Delta\beta_4 \\ \Delta\beta_5 \\ \Delta\beta_6 \end{bmatrix} = \begin{bmatrix} \pi_{11} & \pi_{12} & \pi_{12} & & & \\ \pi_{12} & \pi_{11} & \pi_{12} & & & \\ \pi_{12} & \pi_{12} & \pi_{11} & & & \\ & & & \pi_{44} & & \\ & & & & \pi_{44} & \\ & & & & & \pi_{44} \end{bmatrix} \begin{bmatrix} \sigma_x \\ \sigma_y \\ \sigma_z \\ \tau_{yz} \\ \tau_{zx} \\ \tau_{xy} \end{bmatrix} \tag{49}$$

Also as a result of cubic symmetry, there are only three independent components π_{11}, π_{12} and π_{44} in the piezo-optical tensor.

The procedure to obtain the anisotropic stress-optic coefficient is shown in figure 45. The general relation shown in equation 48 is first transferred to the principal coordinate

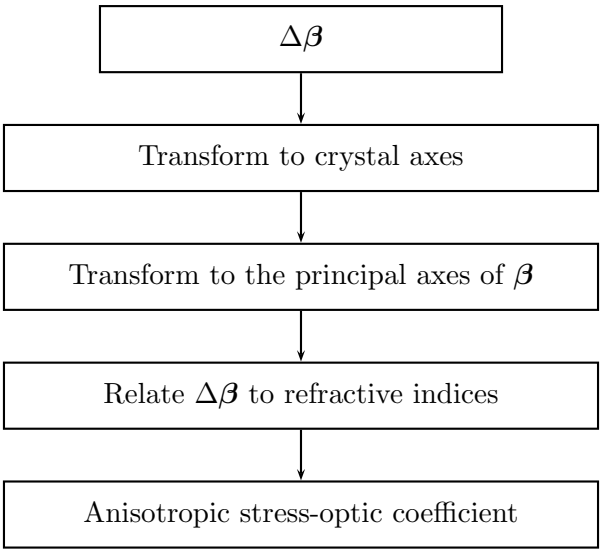

Figure 45: Flow chart of the analysis of the anisotropic in stress-optical coefficient

of the impermeability tensor. The matrix for coordinate rotation around z-axis can be expressed as

$$\boldsymbol{T} = \begin{bmatrix} \cos\phi & \sin\phi & 0 \\ -\sin\phi & \cos\phi & 0 \\ 0 & 0 & 1 \end{bmatrix} \tag{50}$$

This coordination transformation can be expressed in matrix format,

$$\boldsymbol{x}' = \boldsymbol{T}\boldsymbol{x} \tag{51}$$

where x' is the position in the new coordinate, thus,

$$\begin{bmatrix} x_1' \\ x_2' \\ x_3' \end{bmatrix} = \begin{bmatrix} x_1\cos\phi + x_2\sin\phi \\ -x_1\sin\phi + x_2\cos\phi \\ x_3 \end{bmatrix} \tag{52}$$

substitute this transformation into the refractive index ellipsoid equation 34, the transformation matrix of the impermeability tensor can be given as,

$$\boldsymbol{B}(\phi) = \begin{bmatrix} \cos^2\phi & \sin^2\phi & 0 & 0 & 0 & \sin 2\phi \\ \sin^2\phi & \cos^2\phi & 0 & 0 & 0 & -\sin 2\phi \\ 0 & 0 & 1 & 0 & 0 & 0 \\ 0 & 0 & 0 & \cos\phi & -\sin\phi & 0 \\ 0 & 0 & 0 & \sin\phi & \cos\phi & 0 \\ -\frac{1}{2}\sin 2\phi & \frac{1}{2}\sin 2\phi & 0 & 0 & 0 & \cos 2\phi \end{bmatrix} \tag{53}$$

It is noticed that the transformation matrix is not symmetric or antisymmetric. In the new coordinate $\boldsymbol{x'}$, the impermeability tensor can be expressed as,

$$\boldsymbol{\beta'} = \boldsymbol{B}(\phi)\boldsymbol{\beta} \tag{54}$$

The inverse transformation is $\boldsymbol{B}(-\phi)$, and

$$\boldsymbol{B}(\phi)\boldsymbol{B}(-\phi) = \boldsymbol{I} \tag{55}$$

Because

$$\boldsymbol{B}\Delta\boldsymbol{\beta} = \boldsymbol{B}(\phi)\boldsymbol{\pi}\boldsymbol{B}(-\phi)\boldsymbol{B}(\phi)\boldsymbol{\sigma} \tag{56}$$

Then in the new coordinate $\boldsymbol{x'}$

$$\boldsymbol{B'} = \boldsymbol{\pi'}\boldsymbol{\sigma'} \tag{57}$$

The impermeability tensor in the new coordinate is,

$$\boldsymbol{\pi'} = \boldsymbol{B}(\phi)\boldsymbol{\pi}\boldsymbol{B}(-\phi) \tag{58}$$

For a thin silicon sample, the shear stresses τ_{xz}, τ_{yz} and the normal stress σ_z can be considered zero, and the non-zero components, σ_x, σ_y and τ_{xy}, can be considered uniform through the thickness. Therefore, the state of stress in a thin silicon sample can be consider as a state of plane stress. The orientation of the principal axes of the impermeability is determined by the isoclinic angle, θ, the principal direction of the impermeability tensor

obtained from experiment by the phase stepping. This relation in Equation 48 can also be transformed to the principal axes, where $\beta_6' = 0$

$$\begin{bmatrix} \Delta\beta_1' \\ \Delta\beta_2' \\ \Delta\beta_3' \\ 0 \\ 0 \\ 0 \end{bmatrix} = \begin{bmatrix} \pi_{11}' & \pi_{12}' & \pi_{12} & 0 & 0 & \pi_{16}' \\ \pi_{12}' & \pi_{11}' & \pi_{12} & 0 & 0 & -\pi_{16}' \\ \pi_{12} & \pi_{12} & \pi_{11} & 0 & 0 & 0 \\ 0 & 0 & 0 & \pi_{44} & 0 & 0 \\ 0 & 0 & 0 & 0 & \pi_{44} & 0 \\ \frac{\pi_{16}'}{2} & -\frac{\pi_{16}'}{2} & 0 & 0 & 0 & \pi_{66}' \end{bmatrix} \begin{bmatrix} \sigma_x' \\ \sigma_y' \\ 0 \\ 0 \\ 0 \\ \tau_{xy}' \end{bmatrix} \tag{59}$$

where σ_x', σ_y' and τ_{xy}' are the stress components in the principal axes of the impermeability tensor. The piezo-optical matrix is no longer symmetric. Generally, the coefficients in these principal axes are functions of θ. For the (001) plane observed along the [001] direction,

$$\pi_{11}' = \pi_{11} - \frac{1}{2}(\pi_{11} - \pi_{12} - \pi_{44}) \sin^2 2\theta \tag{60a}$$

$$\pi_{12}' = \pi_{12} + \frac{1}{2}(\pi_{11} - \pi_{12} - \pi_{44}) \sin^2 2\theta \tag{60b}$$

$$\pi_{16}' = -\frac{1}{2}(\pi_{11} - \pi_{12} - \pi_{44}) \sin 4\theta \tag{60c}$$

$$\pi_{66}' = \pi_{44} + (\pi_{11} - \pi_{12} - \pi_{44}) \sin^2 2\theta \tag{60d}$$

In these principal axes, the relation between τ_{xy} and $\sigma_x - \sigma_y$ can be derived from $\beta_6' = 0$.

$$\tau_{xy}' = \frac{\pi_{16}'}{2\pi_{66}'}(\sigma_x' - \sigma_y') \tag{61}$$

The principal shear stress can be expressed as [70],

$$\tau_0 = \sqrt{(\sigma_x - \sigma_y)^2 + 4\tau_{xy}^2} \tag{62}$$

Thus,

$$\begin{aligned} \tau_0 &= (\sigma_x' - \sigma_y')\sqrt{1 + \left(\frac{\pi_{16}'}{\pi_{66}'}\right)^2} \\ &= 2\tau_{xy}'\sqrt{\left(1 + \frac{\pi_{66}'}{\pi_{16}'}\right)^2} \end{aligned} \tag{63}$$

This relation is used to determine the principal directions of the residual stresses and their deviation from the principal axes of the impermeability where the phase retardation is

related to the impermeability by [3]

$$\delta = \frac{\pi t n_0^3}{\lambda}(\Delta\beta_1' - \Delta\beta_2') \tag{64}$$

where n_0 is the refractive index when the silicon is stress free. The stress-optic coefficient $C(\theta)$ for the (001) orientation observed along the normal direction can be obtained by substituting Equation 59, 60 and 64 into Equation 32.

$$C_{(001)}(\theta) = \frac{n_0^3}{2}\frac{1}{\sqrt{\frac{\sin^2 2\theta}{\pi_{44}^2} + \frac{\cos^2 2\theta}{(\pi_{11}-\pi_{12})^2}}} \tag{65}$$

Figure 46 shows the variation of $C(\theta)$ as a function of θ for the (001) and (111) orientations. Since the values of $\pi_{11} - \pi_{12}$ and π_{44} can be assumed to be known, the anisotropy of $C(\theta)$ can be determined. For the (001), the stress-optic coefficient reaches a maximum of $n_0^2\pi_{44}/2$ when the principal stress is along the [100], and a minimum $n_0^3(\pi_{11} - \pi_{12})/2$ when the principal stress is along the [110]. The angle of the deviation between the principal directions of the dielectric impermeability and the stress tensor is derived from Equation 61 as [70],

$$\phi_{(001)} = -\frac{1}{2}\arctan\frac{(\pi_{11} - \pi_{12} - \pi_{44})\sin 4\theta}{(\pi_{11} - \pi_{12})\sin^2 2\theta + \pi_{44}(1 + \cos^2 2\theta)} \tag{66}$$

As shown in Figure 47(a), the deviation between the principal axes of the permeability and the stresses is within 7° for the (001). Therefore, in the experiment, the isoclinic angle can be considered as the principal orientation of the stresses without introducing much error.

5.4.2 The analysis of (110) silicon

As shown in Figure 48, EFG silicon has a preponderantly orientation of (110) irrespective of the seed crystal orientation. The effective stress-optical coefficient of the (110) orientation can be obtained in the same way. The piezo-optical tensor is first transformed to the local coordinate, $(001, 1\bar{1}0, 110)$, of the crystal shown in Figure 49. The normalized transformation matrix is,

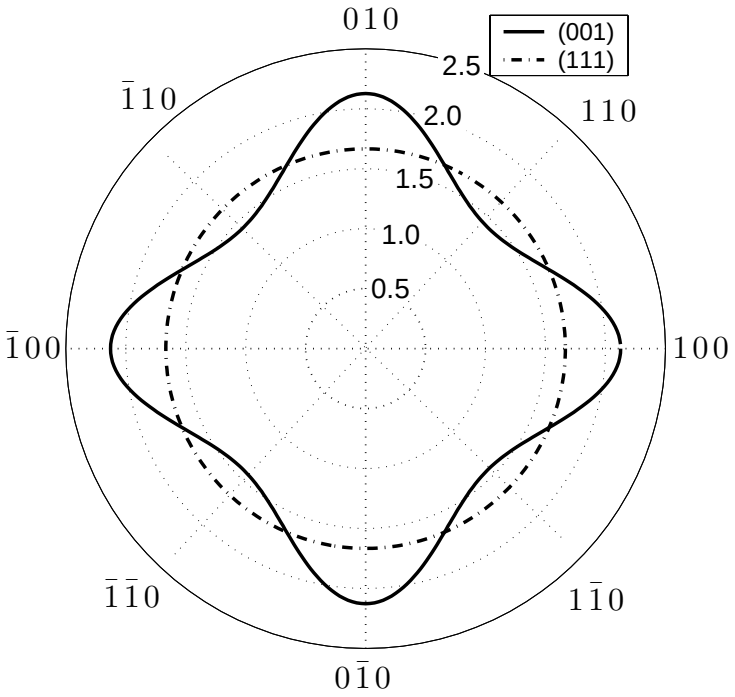

Figure 46: Effective stress-optic coefficient for the (001) and (111) orientations

$$\boldsymbol{T} = \begin{bmatrix} 0 & 0 & 1 \\ \frac{1}{\sqrt{2}} & -\frac{1}{\sqrt{2}} & 0 \\ \frac{1}{\sqrt{2}} & \frac{1}{\sqrt{2}} & 0 \end{bmatrix} \tag{67}$$

The piezo-optical matrix in this new coordinate is,

$$\boldsymbol{\pi}' = \begin{bmatrix} \frac{1}{2}(\pi_{11}+\pi_{12}+\pi_{44}) & \frac{1}{2}(\pi_{11}+\pi_{12}-\pi_{44}) & \pi_{12} & 0 & 0 & 0 \\ \frac{1}{2}(\pi_{11}+\pi_{12}-\pi_{44}) & \frac{1}{2}(\pi_{11}+\pi_{12}+\pi_{44}) & \pi_{12} & 0 & 0 & 0 \\ \pi_{12} & \pi_{12} & \pi_{11} & 0 & 0 & 0 \\ 0 & 0 & 0 & \pi_{44} & 0 & 0 \\ 0 & 0 & 0 & 0 & \pi_{44} & 0 \\ 0 & 0 & 0 & 0 & 0 & \pi_{11}-\pi_{12} \end{bmatrix} \tag{68}$$

This matrix is further transform into the principal coordinate of the impermeability

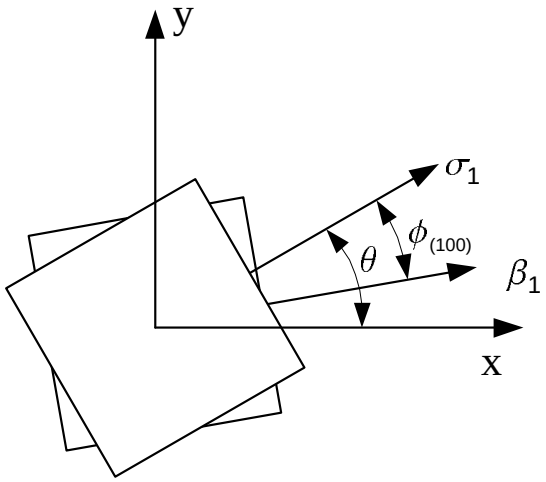

(a) The physical meaning of the deviation

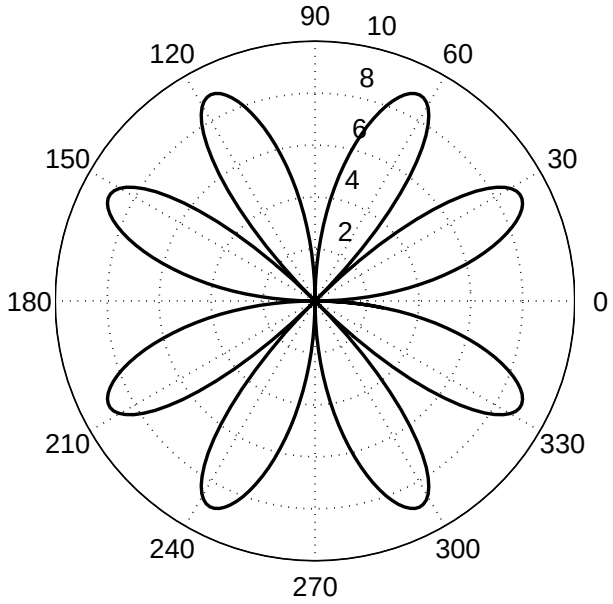

(b) The distribution of the deviation (°)

Figure 47: The deviation between the principal axes of the stresses and the impermeability of the (001) orientation silicon

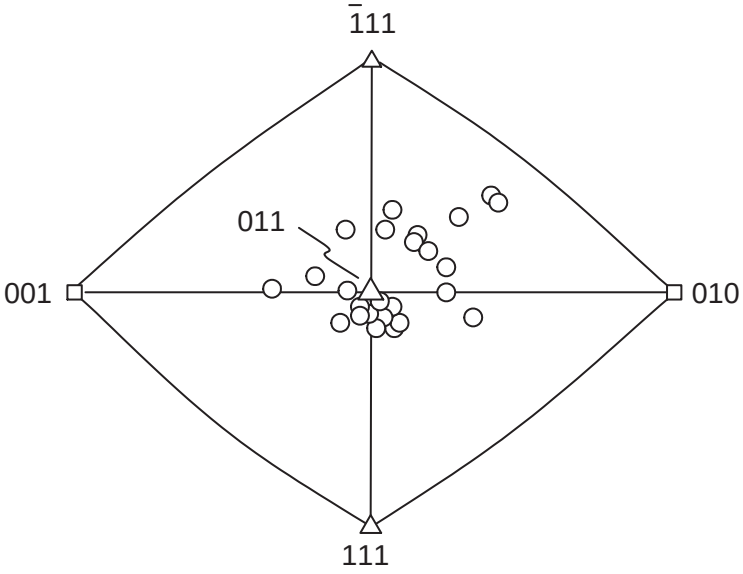

Figure 48: The pole diagram of EFG ribbon shows the surface orientation is usually very close to (110) [2].

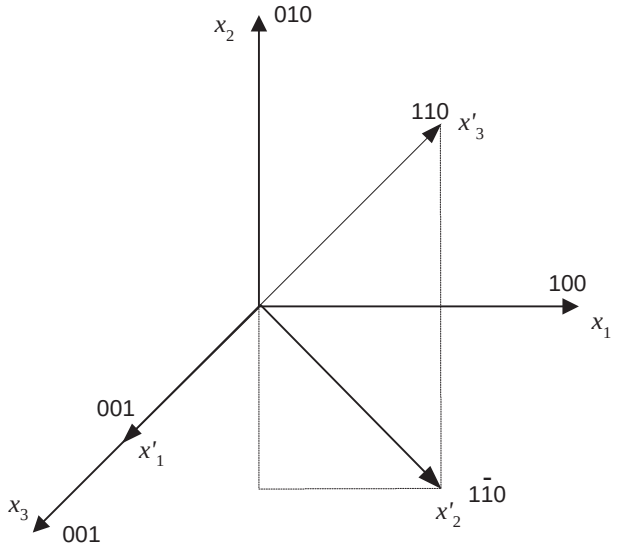

Figure 49: The local coordinate of (110) silicon

using Equation 58. The piezo-optical matrix is similar with that of (001) silicon,

$$\boldsymbol{\pi}'' = \begin{bmatrix} \pi_{11}'' & \pi_{12}'' & \pi_{12} & 0 & 0 & \pi_{16}'' \\ \pi_{12}'' & \pi_{11}'' & \pi_{12} & 0 & 0 & -\pi_{16}'' \\ \pi_{12} & \pi_{12} & \pi_{11} & 0 & 0 & 0 \\ 0 & 0 & 0 & \pi_{44} & 0 & 0 \\ 0 & 0 & 0 & 0 & \pi_{44} & 0 \\ \frac{1}{2}\pi_{16}'' & -\frac{1}{2}\pi_{16}'' & 0 & 0 & 0 & \pi_{66}'' \end{bmatrix} \tag{69}$$

where,

$$\pi_{11}'' = \pi_{11} - \frac{1}{2}\left(\pi_{11} - \pi_{12} - \pi_{44}\right)\cos^2 2\theta \tag{70a}$$

$$\pi_{12}'' = \pi_{12} + \frac{1}{2}(\pi_{11} - \pi_{12} - \pi_{44})\cos^2 2\theta \tag{70b}$$

$$\pi_{16}'' = \frac{1}{2}(\pi_{11} - \pi_{12} - \pi_{44})\sin 4\theta \tag{70c}$$

$$\pi_{66}'' = \pi_{44} + (\pi_{11} - \pi_{12} - \pi_{44})\cos^2 2\theta \tag{70d}$$

The coefficient is the same with that of (001) silicon,

$$C_{(011)}(\theta) = \frac{n_0^3}{2}\frac{1}{\sqrt{\frac{\sin^2 2\theta}{\pi_{44}^2} + \frac{\cos^2 2\theta}{(\pi_{11}-\pi_{12})^2}}} \tag{71}$$

5.4.3 Analysis of (111) silicon

The effective stress-optical coefficient of the (111) orientation can be obtained in the same way. The local coordinate of (111) silicon, $(11\bar{2}, \bar{1}10, 111)$ is shown in Figure 50, and the transform matrix is,

$$\boldsymbol{T} = \begin{bmatrix} \frac{\sqrt{6}}{6} & -\frac{\sqrt{2}}{2} & \frac{\sqrt{3}}{3} \\ \frac{\sqrt{6}}{6} & \frac{\sqrt{2}}{2} & \frac{\sqrt{3}}{3} \\ -\frac{\sqrt{6}}{3} & 0 & \frac{\sqrt{3}}{3} \end{bmatrix} \tag{72}$$

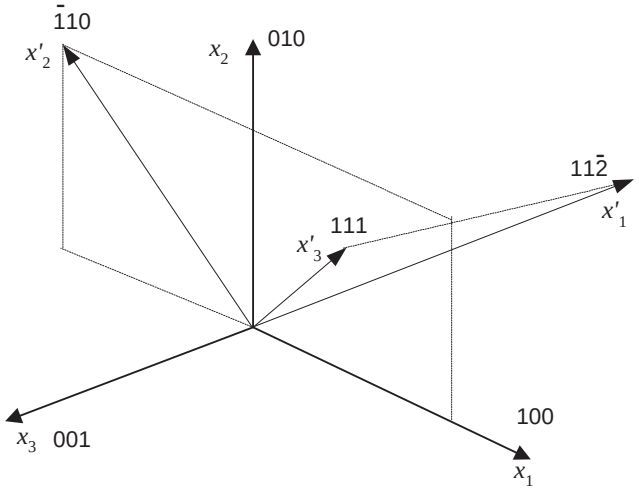

Figure 50: The local coordinate of (111) silicon

The new impermeability tensor after transformation can be expressed as,

$$\begin{bmatrix} \Delta\beta_1'' \\ \Delta\beta_2'' \\ \Delta\beta_3'' \\ 0 \\ 0 \\ 0 \end{bmatrix} = \begin{bmatrix} \pi_{11}'' & \pi_{12}'' & \pi_{13}'' & \pi_{14}'' & \pi_{15}'' & 0 \\ \pi_{12}'' & \pi_{11}'' & \pi_{13}'' & -\pi_{14}'' & -\pi_{15}'' & 0 \\ \pi_{12}'' & \pi_{12}'' & \pi_{33}'' & 0 & 0 & 0 \\ \frac{\pi_{14}''}{2} & -\frac{\pi_{14}''}{2} & 0 & \pi_{44}'' & 0 & -\pi_{15}'' \\ \frac{\pi_{15}''}{2} & -\frac{\pi_{15}''}{2} & 0 & 0 & \pi_{44}'' & \pi_{14}'' \\ 0 & 0 & 0 & -\pi_{15}'' & \pi_{14}'' & \pi_{44}'' \end{bmatrix} \begin{bmatrix} \sigma_x'' \\ \sigma_y'' \\ 0 \\ 0 \\ 0 \\ \tau_{xy}'' \end{bmatrix} \tag{73}$$

where,

$$\pi_{11}'' = \frac{1}{2}(\pi_{11} + \pi_{12} + \pi_{44}) \tag{74a}$$

$$\pi_{12}'' = \frac{1}{6}(\pi_{11} + 5\pi_{12} - \pi_{44}) \tag{74b}$$

$$\pi_{13}'' = \frac{1}{3}(\pi_{11} + 2\pi_{12} - \pi_{44}) \tag{74c}$$

$$\pi_{14}'' = \frac{\sqrt{2}}{3}(\pi_{11} - \pi_{12} - \pi_{44})\cos 3\theta \tag{74d}$$

$$\pi_{15}'' = \frac{\sqrt{2}}{3}(\pi_{11} - \pi_{12} - \pi_{44})\sin 3\theta \tag{74e}$$

$$\pi_{33}'' = \frac{1}{3}(\pi_{11} + 2\pi_{12} + 2\pi_{44}) \tag{74f}$$

$$\pi_{44}'' = \frac{1}{3}(2\pi_{11} - 2\pi_{12} + \pi_{44}) \tag{74g}$$

As shown in Equation 73, the shear stress in the principal coordinate of the impermeability is also zero,

$$\tau_{xy}{}'' = 0 \tag{75}$$

which indicates that there is no deviation between the two principal axes. The two components of the stress optic tensor, $\pi_{11}{}''$ and $\pi_{12}{}''$ are also independent of the orientation of the principal axes, therefore, (111) silicon behaves as if it were isotropic. So that

$$C_{(111)}(\theta) = \frac{n_0^3}{2}\frac{\pi_{11} - \pi_{12} + 2\pi_{44}}{3} \tag{76}$$

As shown in Figure 46, the stress-optical coefficient of the (111) orientation is constant. Other orientations have no simple equivalent stress-optic coefficient.

5.5 Conclusions

The stress-optic coefficients of (001), (011) and (111) silicon were derived analytically. The (001) and (011) silicon have the same anisotropic coefficients with a maximum of $n_0^2\pi_{44}/2$ and minimum of $n_0^3(\pi_{11}-\pi_{12})/2$. The angle of the deviation between the principal directions of of the stresses and retardation is negligible. The stress-optic coefficient of the (111) silicon is isotropic and independent on the orientation.

CHAPTER VI

EXPERIMENTAL RESULTS AND DISCUSSION

6.1 Summary

This chapter summarizes the calibration of the stress-optic coefficients of the CZ, EFG and cast silicon. A four-point bending fixture will be used for the calibration. The samples are silicon beams with various orientations sectioned from the silicon wafers. The experimental data will be analyzed using least-square fit to reduce error.

6.2 Calibration of the Anisotropy in CZ Silicon

Four-point bending, shown in Figure 51, was used to introduce known stresses in single crystal silicon samples that were removed from a wafer at various orientations to calibrate the residual stress polariscope and the anisotropy. The load was applied by two weights and the residual stresses were assumed to be negligible compared to the applied stresses. Seven silicon 'beams', six of dimensions $100 \times 8 \times 0.5$ mm and one of $120 \times 11 \times 0.5$ mm, were removed by dicing from six 100 mm and one 200 mm (001) double-side polished single crystal Cz wafers respectively. As shown in Figure 52, each beam has an orientation from 0° to 90° relative to the primary flat of the wafers with a step of 15°.

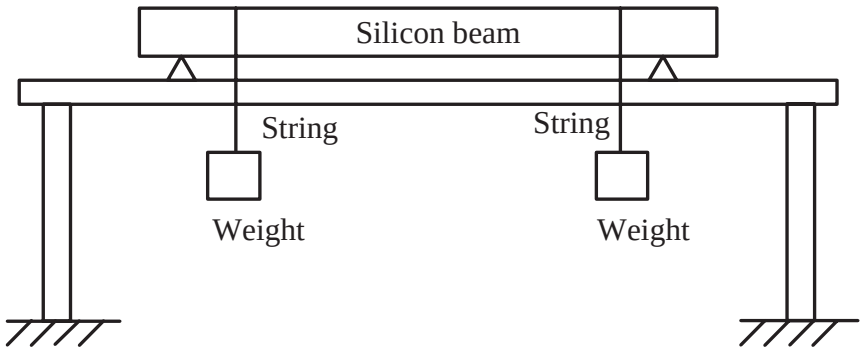

Figure 51: Four-point bending experiment setup

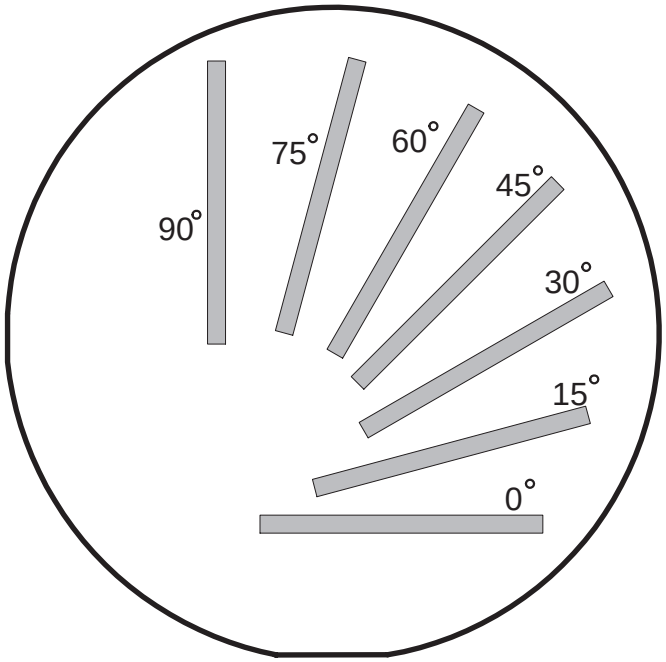

Figure 52: Silicon beams for the calibration of anisotropy

Figure 53 shows the results of the retardation and the isoclinic angle of one beam sectioned at 30° relative to the primary flat with the fringe multiplication factor of 1. The results of the beams with other orientations are similar. The physical size of the measured area is 170×50 pixels, or 8×25 mm. It can be seen that the retardation is uniform along the longitudinal direction and the gray scale of the image indicates that it is linear along the transverse direction. The isoclinic angle in the upper half of the beam is zero, which indicates that the principal stress is along the longitudinal direction, and in the lower half it is $\pi/2$ or $-\pi/2$, which means that the principal stress is along the transverse direction. There is a small undefined region in the center of the sample where the direction can not be measured accurately due to the low stress level.

Usually the maximum stress is used for the purpose of characterization. However, the maximum stress cannot be determined with enough accuracy because the edges of the beams are not clearly defined in the images, and a variation of one pixel, or 0.2 mm, can introduce a 5% error. On the other hand, the slopes of the retardation, $d\delta/dy$, can be determined with higher accuracy using a linear least-square fit. This slope can be related to the stress-optic

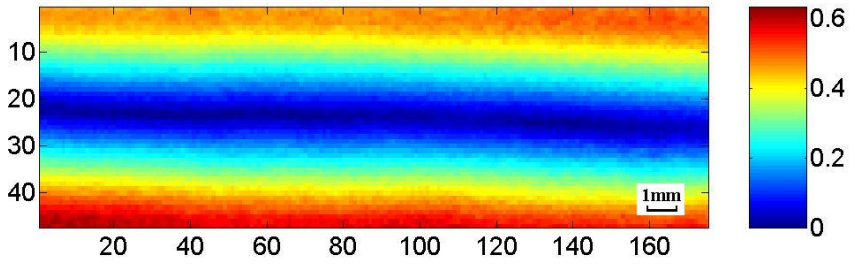

(a) retardation

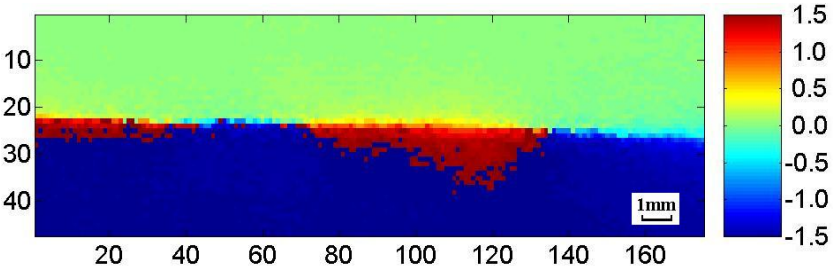

(b) isoclinic

Figure 53: The calibration result of four-point bending of a silicon beam cut at 30° relative to the orientation flat of the wafer with fringe multiplication factor 1. The green and blue pixels represent $\theta = 0$ and $\pi/2$ respectively

coefficient, therefore, it can be determined with higher accuracy. Figure 54 shows a typical least-square fit of the retardation. The correlation coefficient of the linear fit is 0.997. The drop of the retardation at the two edges is attributed to the loss in spatial resolution because of the non-ideal point light source, which has a diameter of 8 mm. The principal stresses for pure bending are,

$$\sigma_1 = \frac{M}{I} y, \quad \sigma_2 = 0 \tag{77}$$

where $I = h^3 t/12$ is the moment of inertia of the cross section, M is the applied moment, and y is the vertical location from the center. By substituting Equation 77 into Equation 32, the stress-optic coefficient can be obtained in terms of the slope of the retardation,

$$C = \frac{d\delta}{dy} \Big/ \left(\frac{2\pi t}{\lambda} \frac{M}{I} \right) \tag{78}$$

Table 7 shows the average of the slopes along the longitudinal direction. The standard deviation of the average is within 0.003, or 2% of the average, which demonstrates the uniformity in the retardation along the longitudinal direction. The average slope is transformed

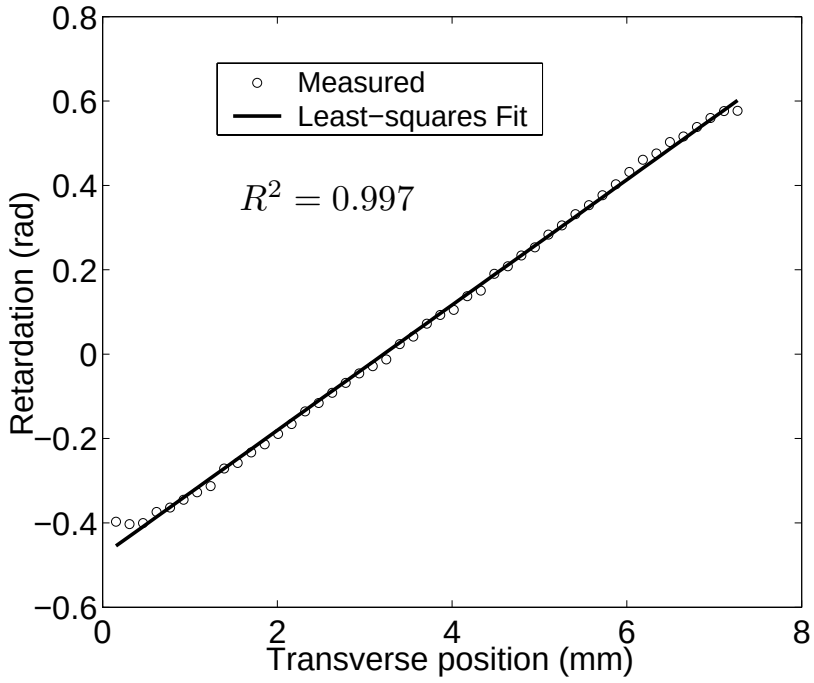

Figure 54: Least-squares fit of the retardation of an CZ sample along transverse direction

to the stress-optic coefficient, C using Equation 78. Table 7 shows the seven coefficients corresponding to the seven different orientations obtained from the seven samples. The components of the piezo-stress tensor, $\pi_{11} - \pi_{12}$ and π_{44}, can be obtained from Equation 65 as $\pi_{11} - \pi_{12} = 2C|_{\theta=0^\circ}/n_0^3$ and $\pi_{44} = 2C|_{\theta=45^\circ}/n_0^3$. However, these constants can be determined with higher accuracy through the nonlinear least-square fit of the anisotropic stress-optic coefficient shown in Equation 65.

$$\begin{cases} \dfrac{\partial}{\partial(\pi_{11}-\pi_{12})} \displaystyle\sum_{i=1}^{7} [C(\theta_i) - C_i]^2 = 0 \\ \dfrac{\partial}{\partial \pi_{44}} \displaystyle\sum_{i=1}^{7} [C(\theta_i) - C_i]^2 = 0 \end{cases} \tag{79}$$

where C_i, $i = 1 \cdots 7$, are the seven stress-optic coefficients of different orientations shown in Table 7. Equation 79 is solved by numerical methods, and the results are shown in Table 7 and Figure 55. The discrepancy between the least-square fit and the experiment is within 3%, which demonstrates that the anisotropic stress-optic coefficient is valid. The

Table 7: The slope of the retardation of silicon beams with different orientations

angle (°)	$d\delta/dy$ (rad/mm)	Standard deviation	C ($\times 10^{-11}$Pa^{-1})	Least-squares fit ($\times 10^{-11}$Pa^{-1})
0*	0.1022	0.0022	1.422	1.435
15	0.1407	0.0029	1.564	1.544
30	0.1624	0.0025	1.805	1.866
45	0.1939	0.0027	2.155	2.127
60	0.1673	0.0029	1.860	1.866
75	0.1424	0.0022	1.583	1.544
90	0.1275	0.0020	1.417	1.435

* This beam is $120 \times 11 \times 0.5$ mm sectioned from 8' wafer

components of the piezo-stress tensor obtained by this method are,

$$\pi_{11} - \pi_{12} = 9.88 \times 10^{-13}\ \text{Pa}^{-1}, \tag{80a}$$

$$\pi_{44} = 6.50 \times 10^{-13}\ \text{Pa}^{-1} \tag{80b}$$

The results are lower than those measured by Giardini [54], $\pi_{11}-\pi_{12} = 14.4\times10^{-13}$ Pa^{-1}, $\pi_{44} = 10.0 \times 10^{-13}$ Pa^{-1}, but higher to those obtained by Iwaki [66], $\pi_{11} - \pi_{12} = 8.48 \times 10^{-13}$ Pa^{-1} and $\pi_{44} = 4.58 \times 10^{-13}$ Pa^{-1}. The maximum and minimum of the stress-optic coefficient are:

$$C_{\max} = 2.127 \times 10^{-11}\ \text{Pa}^{-1}, \tag{81a}$$

$$C_{\min} = 1.435 \times 10^{-11}\ \text{Pa}^{-1} \tag{81b}$$

and the anisotropy in the coefficient is

$$\frac{(C_{\max} - C_{\min})}{C_{\max}} \times 100\% = 33\% \tag{82}$$

The effective stress-optic coefficient for (111) silicon is,

$$C_{111} = 1.68 \times 10^{-11}\ \text{Pa}^{-1} \tag{83}$$

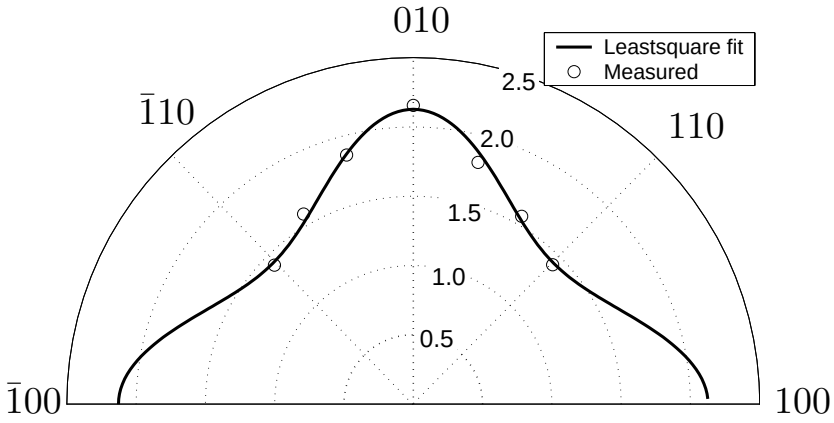

Figure 55: Experimental results of the effective stress-optic coefficient of the (001) orientation compared with theoretical calculations

6.3 Calibration of the Anisotropy in EFG Silicon

The calibration of EFG samples was carried out in the same way as CZ silicon. The size of the beams is $120 \times 12 \times 0.32$ mm removed from 4×4 inches EFG wafers. As shown in Figure 56, each sample has an orientation from 0° to 90° with a step of 15° relative to the growth direction. Compared with single crystal silicon, EFG wafers have notably higher residual stresses. The average shear stress is approximately 5 MPa. To minimize the effect of the residual stresses, a significantly larger load with a maximum stress of 32 MPa, which is two times bigger than that of single crystal, was applied on the beams. After increasing the load, the average residual stress is reduced to 15% of the maximum stress applied. The effect of the residual stress on the stress-optic coefficient is expected to be smaller than 15% because the least-square fit, which is an average along the transverse direction, was used to extract the data.

The retardation of the four-point bending of an EFG sample is shown in Figure 57(a). The maximum retardation is around 1.5 rad for the load of 10 N-mm. Compared with single crystal silicon, the EFG samples have a notably larger variation in the retardation. The reasons for this variation are the residual stresses and the non-uniformity of thickness and light absorption in the EFG material. The retardation of the residual stress is shown in Figure 57(b). The maximum magnitude of the residual stress is around 0.3 rad and the

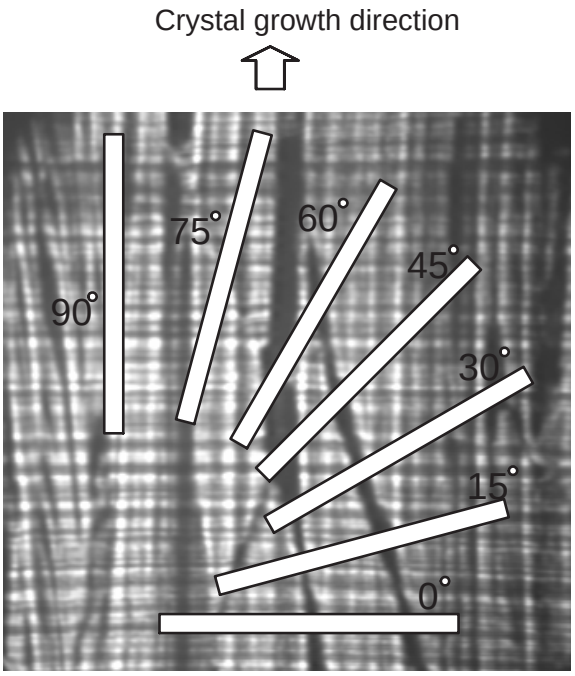

Figure 56: The sample for the calibration of EFG wafer

absolute average is around 0.05 rad.

Once again, the least-square fit is used to extract the slope of the retardation along the transverse direction. It not only reduces the effect of the error, but also can minimize the influence of the residual stress because the residual stress is self-balanced along any section. A linear least-square fit of a randomly selected cross section is shown in Figure 58. The correlation of this fit is $R^2 = 0.988$, which is lower than that of the CZ silicon.

Figure 59(a) shows the variation of the coefficient along the longitudinal direction. A peak-to-peak 30% variation is observed. In order to evaluate the influence of the residual stress on the coefficient, the retardation of the residual stress along the longitudinal direction is also shown in Figure 59(b). However, no clear correlation was observed between the variation of the coefficient and the distribution of the residual stresses.

The stress-optic coefficients and their variations can be obtained in the same way as the CZ silicon. Table 8 shows the value of the coefficients and variances. The anisotropy can be clearly observed in Figure 60. The trend of the anisotropy is close to that of single crystal silicon, and the minimum value $C_{\min}$ is 2.3×10^{-11} MPa^{-1} at 0° and the maximum

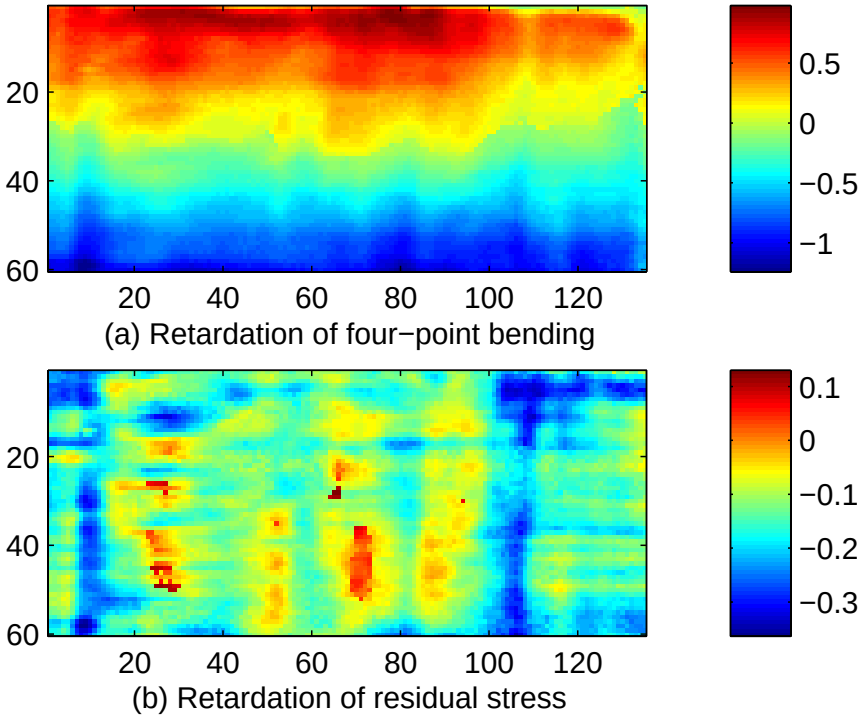

Figure 57: The retardation of the stressed (above) and free (below) sample of EFG wafer with an orientation of 0°

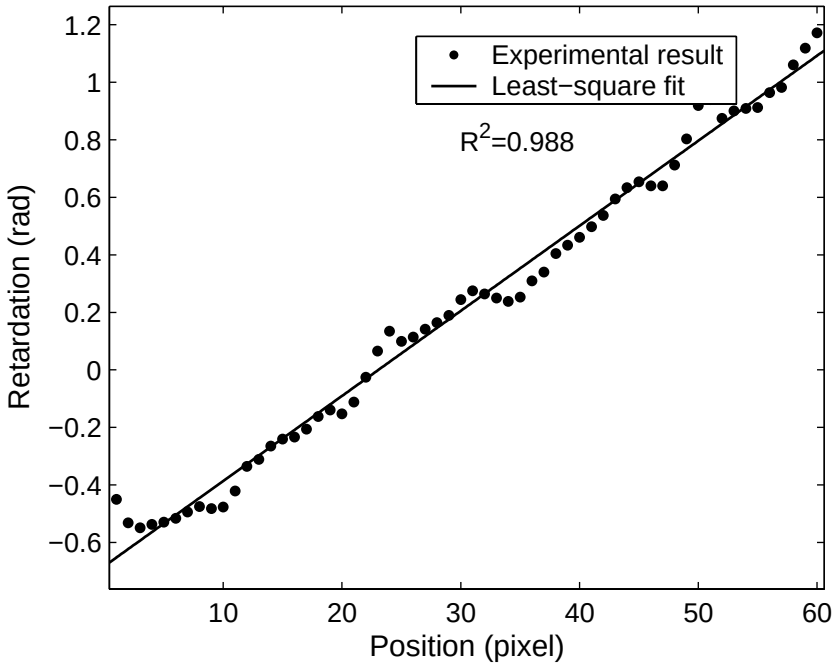

Figure 58: Least-squares fit of retardation along transverse direction of an EFG sample with an orientation of 0°

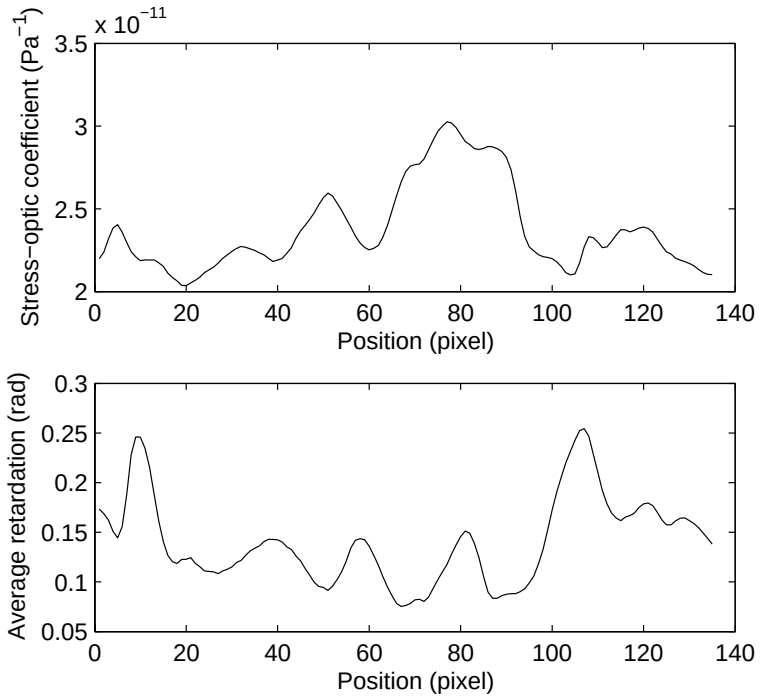

Figure 59: The distribution of stress-optic coefficient (above) and retardation of the residual stress (below) of the EFG sample with an orientation of 0°

value $C_{\max}$ is 3.4 $\times 10^{-11}$ MPa^{-1} at 45°. These values are considerably larger than single crystal silicon, which shows the EFG, as one type of polycrystalline silicon, has different optical properties. The dash line in Figure 60 shows the least-square fit of the experimental results using the theoretical formula shown in equation 65. This least-square fit is 1.7 times larger than that of CZ silicon shown as the solid line. The difference demonstrates that substantial error will be introduced to the residual stresses when the coefficient of single crystal is used for EFG samples.

6.4 Calibration of the Coefficient of Cast Silicon

The calibration of CAST samples was carried out in the same way as EFG silicon. The sample size is 150 × 15 × 0.269 mm removed from 4 × 4 inches double-size polished cast wafers. As shown in Figure 61, each sample has an orientation from 0° to 45° with a step of 9° relative to the growth direction, an extra sample with 90° is also provide for completion. Compared with EFG silicon, cast wafers have relatively lower level of residual stresses. Figure 62 shows the distribution of the retardation of the residual stress in a

Table 8: The stress-optic coefficients of EFG silicon

Sample orientation (°)	C ($\times 10^{-11}$Pa^{-1})	Standard deviation ($\times 10^{-11}$Pa^{-1})
0°	2.312	0.372
15°	2.848	0.578
30°	3.188	0.224
45°	3.433	0.249
60°	3.013	0.410
75°	2.463	0.377
90°	2.297	0.259

cast sample, which was patched together with the beams after sectioning. The average absolute magnitude of the shear stress is 0.04 rad, or approximately 1.5 MPa. The load applied is 230 N-mm, or 36 MPa in terms of the maximum stress in the four-point bending. The average residual stress is reduced to 4% of the maximum applied stress, which is substantially lower than that of EFG silicon.

The retardation of the calibration shown in Figure 63 is also substantially more uniform compared with EFG samples. However, the effect of the grain can still be observed in the distribution. The grain structure of the cast silicon beam is shown in Figure 64. The two dark lines are the strings used to hang the weight. The linear least-square fit is used to extract the stress-optic coefficient as was done for the CZ and EFG sample. A fit of a randomly selected cross section is shown in Figure 65. The correlation coefficient of this fit is 0.992, which is better than that of the EFG silicon and close to the CZ silicon.

The stress-optic coefficients and their variations are shown in Table 9. As observed in the table, the cast wafers have a notably lower variation. Figure 66 shows the distribution of the coefficients. No obvious anisotropy is observed. The dash line in the figure shows the coefficient of (111) silicon, whose stress-optic coefficient is 1.68×10^{-11} Pa^{-1}. The average coefficient of the all the different orientations is 1.66×10^{-11} Pa^{-1}, which is close to the (111) silicon. Therefore, it is reasonable to conclude that the cast silicon is isotropic.

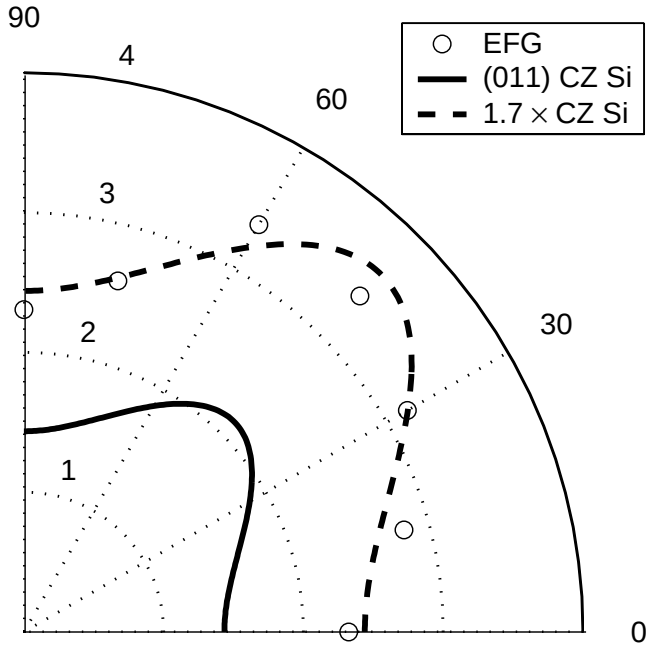

Figure 60: Experimental results of the effective stress-optic coefficient of the EFG sample compared with that of single crystal silicon

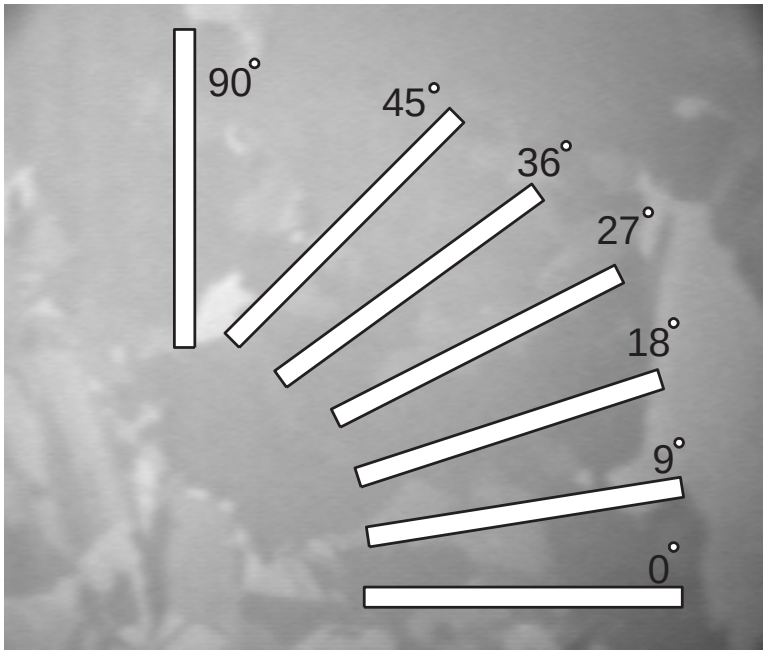

Figure 61: The sample for the calibration of CAST wafer

Figure 62: The residual stress in a CAST wafer

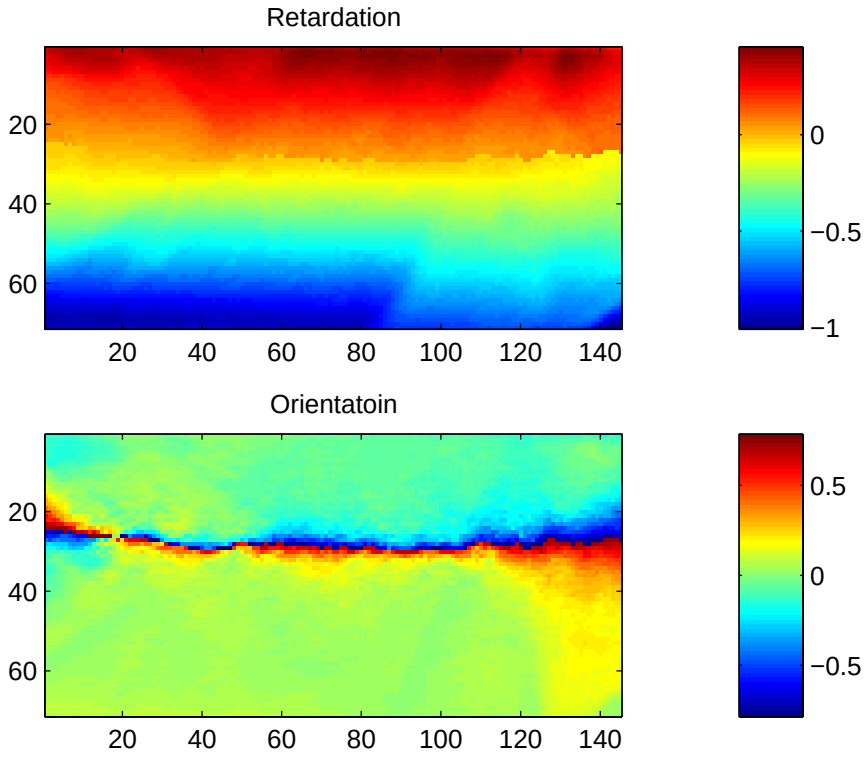

Figure 63: The retardation and isoclinics of the four-point bending of a cast silicon beam sectioned at 45°, the area is selected between the two strings in the bending with a physical size of 30×12 mm.

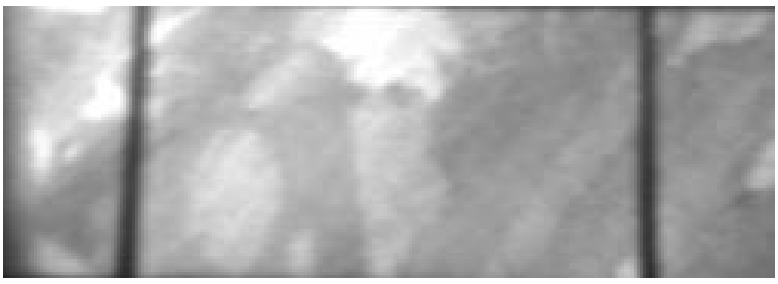

Figure 64: The image of the grain structure of a cast silicon beam sectioned at 45°

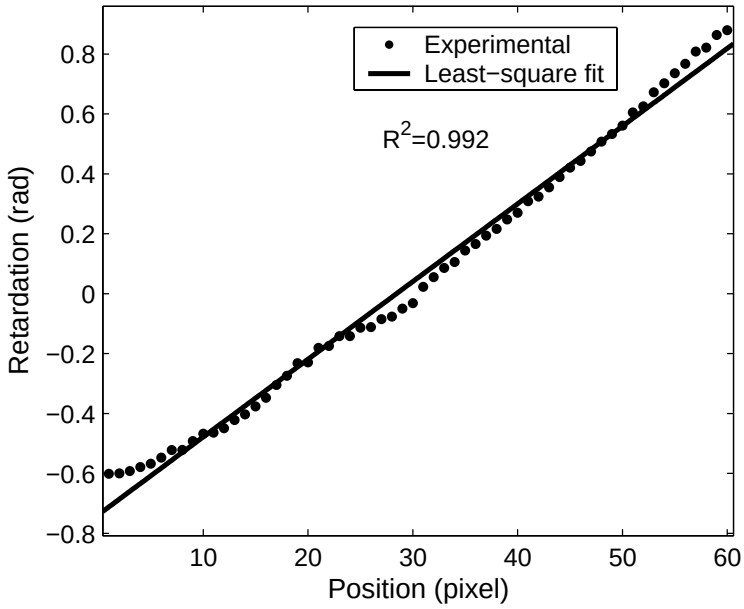

Figure 65: The sample for the calibration of CAST wafer

Table 9: The stress-optic coefficients of CAST silicon

Sample orientation (°)	C ($\times 10^{-11}$Pa^{-1})	Standard deviation ($\times 10^{-11}$Pa^{-1})
0°	1.733	0.165
9°	1.655	0.128
18°	1.852	0.048
27°	1.633	0.095
36°	1.600	0.094
45°	1.608	0.074
90°	1.572	0.059

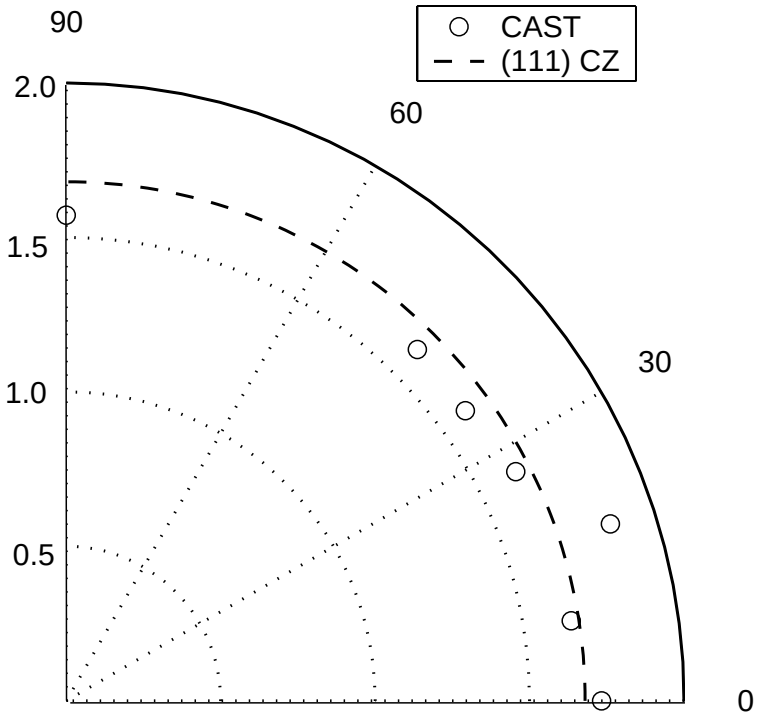

Figure 66: The stress-optic coefficient of CAST silicon

6.5 Conclusions

The anisotropic stress-optic coefficients of CZ, EFG and cast silicon were calibrated by four-point bending, and the components of the stress-optic tensor were measured to be: $\pi_{11} - \pi_{12} = 9.88 \times 10^{-13}$ Pa^{-1}, $\pi_{44} = 6.50 \times 10^{-13}$ Pa^{-1}. The coefficient of EFG has the anisotropic profile same with that of (001) silicon with a magnitude of 1.7 times bigger. The cast silicon have an isotropic coefficient same with the (111) silicon.

Table 10: Summary of the coefficients of CZ, EFG and cast silicon

Silicon	(111) silicon	(001), (011) silicon
CZ	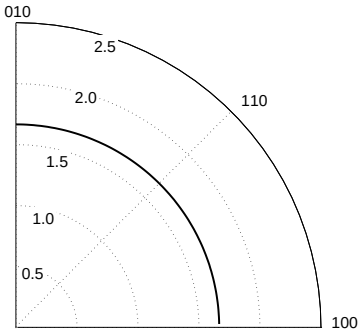 Isotropic	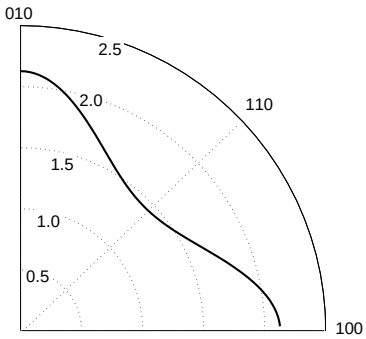 Anisotrpoic
EFG		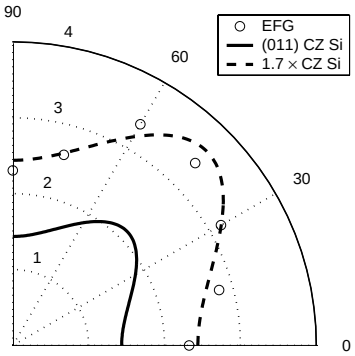 Anisotropic
CAST	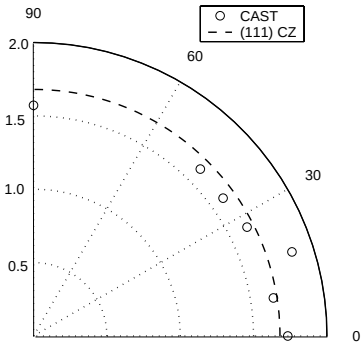 Isotropic	

CHAPTER VII

RESIDUAL STRESS MONITORING OF PHOTOVOLTAIC WAFERS IN PROCESSING

7.1 Summary

This chapter summarizes the research on the characterization of residual stresses and lifetime of polycrystalline sheet silicon for photovoltaic application. The full-field polariscope and scanning room temperature photoluminescence (PL) are used to characterize silicon sheet after major processing steps. The characteristics of the spatial distribution and the quantitative correlation between the residual stresses and the lifetime are presented.

7.2 Residual Stresses in Various Photovoltaic Silicon

The residual stresses were measured using the near-infrared polariscope. Four types of silicon, e.g. CZ silicon, cast, EFG and string ribbon silicon, which are the main material for photovoltaic industry, were selected. Figure 67 shows the transmissive images of the samples. As shown Figure 67(a), the grain structure can be clearly observed in the image after etching, and the sawing marks are also clearly shown in Figure 67(b). High spatial variation is observed in the images of EFG and string ribbon samples. This non-uniformity is mainly attributed to the defects and grain boundaries in the samples. They may degenerate the resolution in the dark regions because the effective contrast is limited in these areas.

Figure 69 shows the typical distribution of the residual stresses in different types of photovoltaic silicon. The residual stresses in cast (Figure 69(a)) and CZ silicon (Figure 69(b)) are relatively uniform, while the string ribbon (Figure 69(c)) and EFG (Figure 69(d)) silicon have substantially higher spatial variation. The pattern of the residual stress is closely related to that of the crystal structure with strips of high stress following the crystal growth direction. The average residual stress is 2.2 MPa and 2.0 MPa for cast and CZ respectively, while string ribbon and EFG silicon have notably high residual stress, e.g. 5.0 MPa and

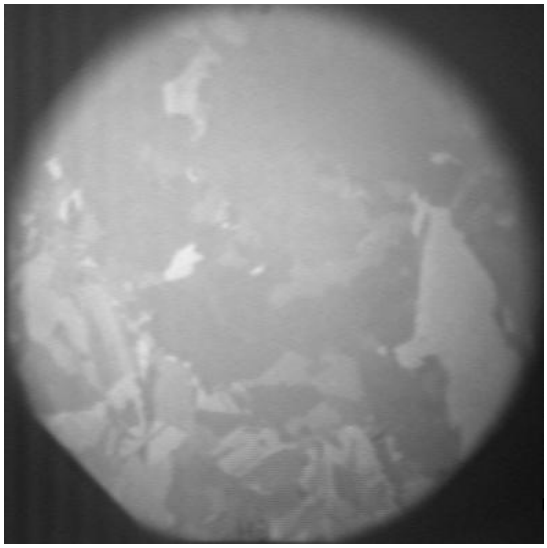

(a) Etched CAST, size 4×4 inches

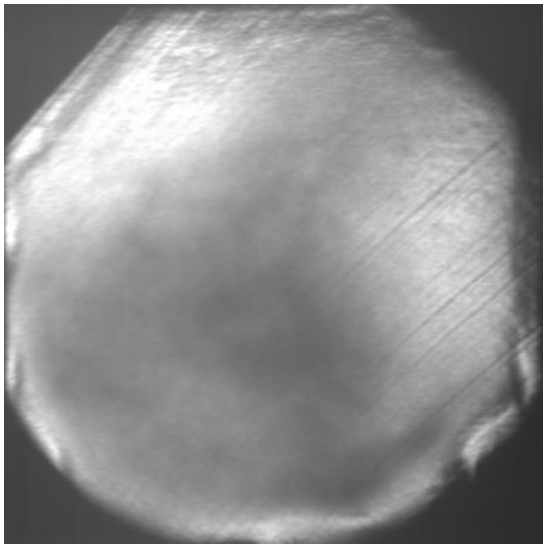

(b) Etched CZ, size 3×3 inches

(c) Ribbon, size 3×2 inches

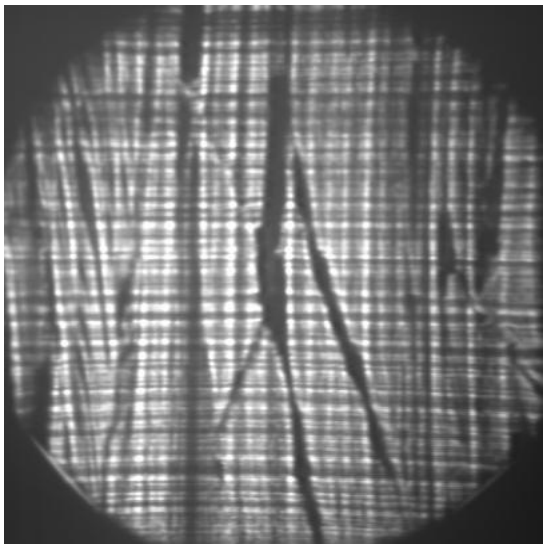

(d) EFG, size 3×3 inches

Figure 67: The transmission images of the image of photovoltaic silicon, the images only show the center part (around 2.5×2.5 inches) of the samples

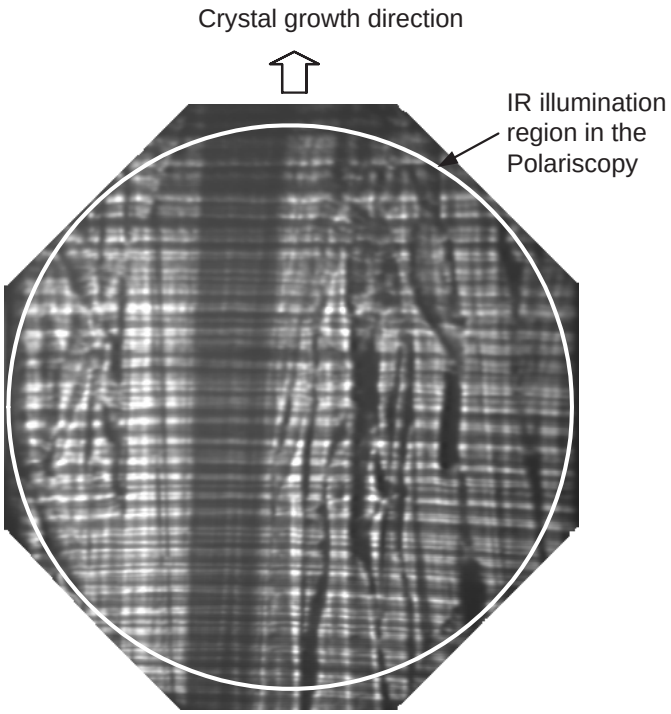

Figure 68: Photograph of an EFG wafer, indicating the growth direction and region of IR illumination.

7.2 MPa in average stress respectively. It is interesting that a defect in the cast wafer is clearly observed in the residual stress mapping shown in Figure 69(a).

Figure 70 shows the probability density function (PDF) of the magnitude of the residual stress. The shape of the PDF of all the four types of silicon is similar and close to an χ^2 distribution. This figure also shows that EFG and string silicon have substantially larger average and maximum residual stress compared with cast and CZ silicon.

The orientation is another critical characteristic for the residual stresses because it determines the propagation mode of the micro cracks. As shown in Figure 71, there are three basic crack propagation modes. Normally the fracture toughness, K_c, is lower for mode I, or opening mode crack [70].

There is no appreciable pattern in the orientation of cast and CZ silicon, while a clear preference is observed in the EFG and ribbon silicon. Figure 72 shows the average orientation as a function of the residual stress. It can be observed that as the magnitude of the residual stresses increases, the average orientation is closer to 90°, which means that the

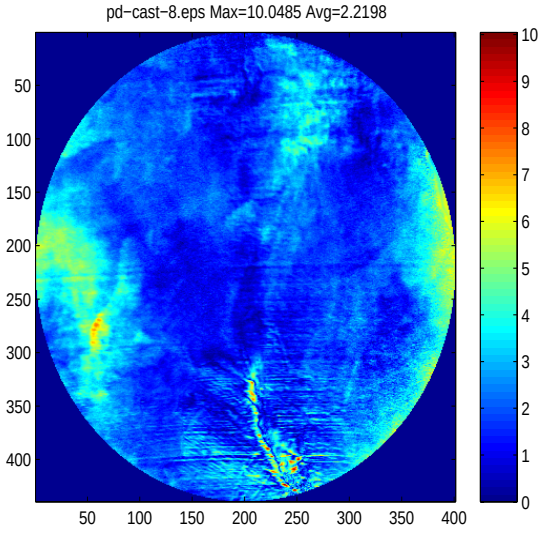

(a) CAST

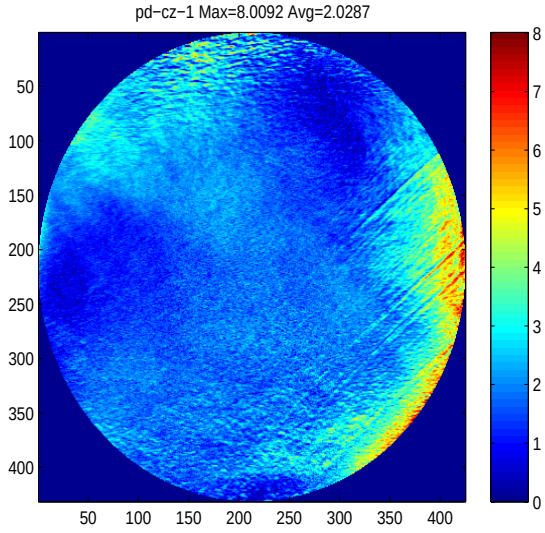

(b) CZ

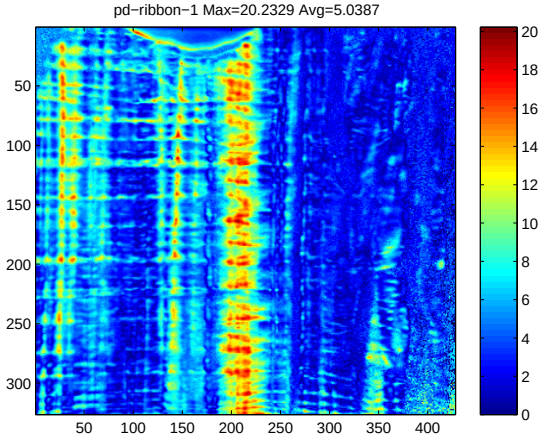

(c) Ribbon

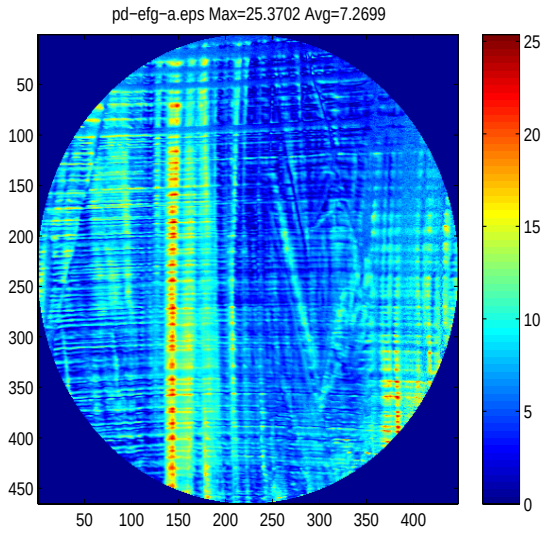

(d) EFG

Figure 69: The typical distribution of the residual stresses in different types of photovoltaic silicon

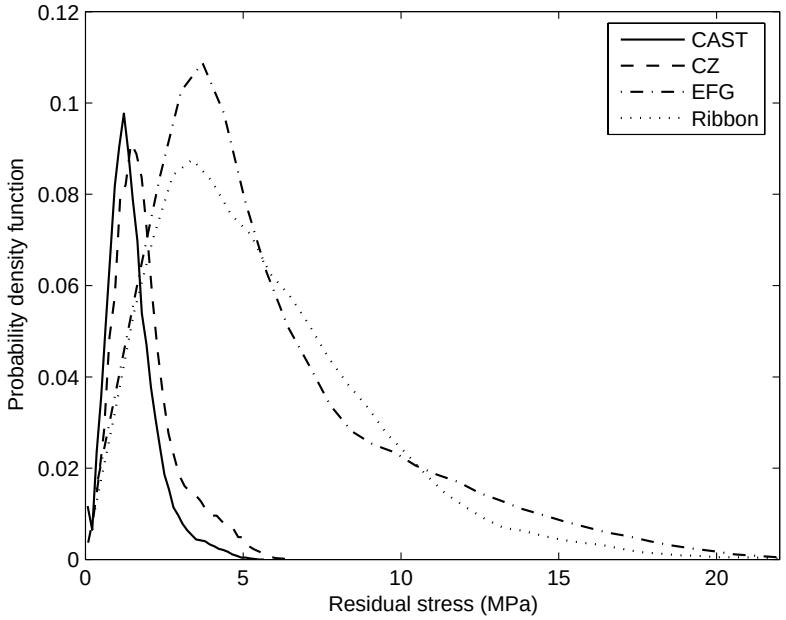

Figure 70: Probability distribution of the magnitude of residual stress in a various photovoltaic silicon

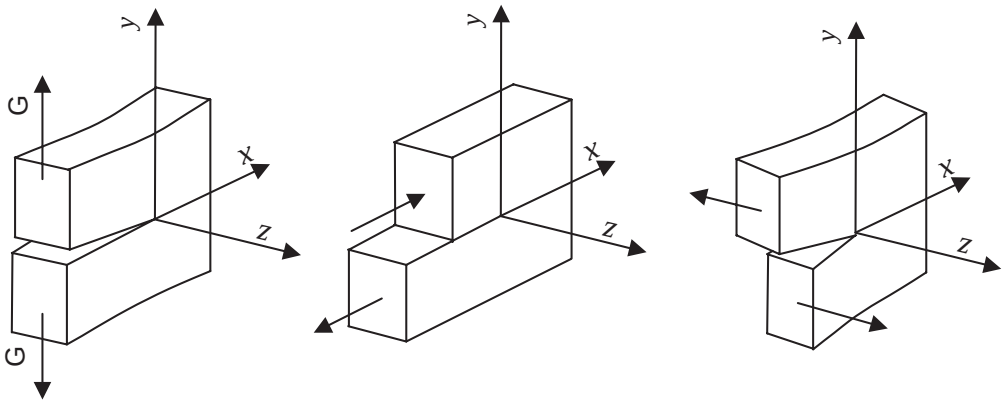

Figure 71: The schematic diagram of different crack propagation modes

stress with a high magnitude is more likely aligned along the crystal growth direction. The stress distribution of a randomly selected cross section perpendicular to the growth direction is shown in Figure 74. Once again the spatial variation is clearly observed. Figure 74 also shows the orientation of the residual stress. It can be seen that the orientation of the residual stress falls into a narrow range from 70° to 90°, which is close to the crystal growth direction.

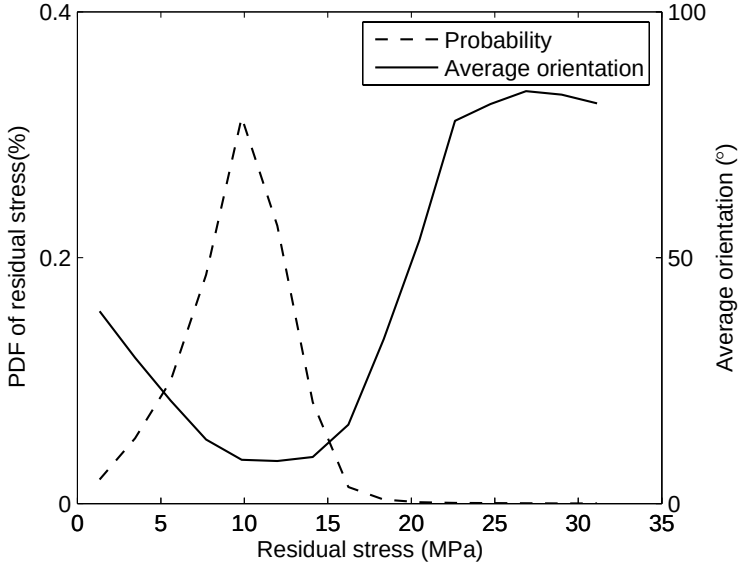

(a) Ribbon

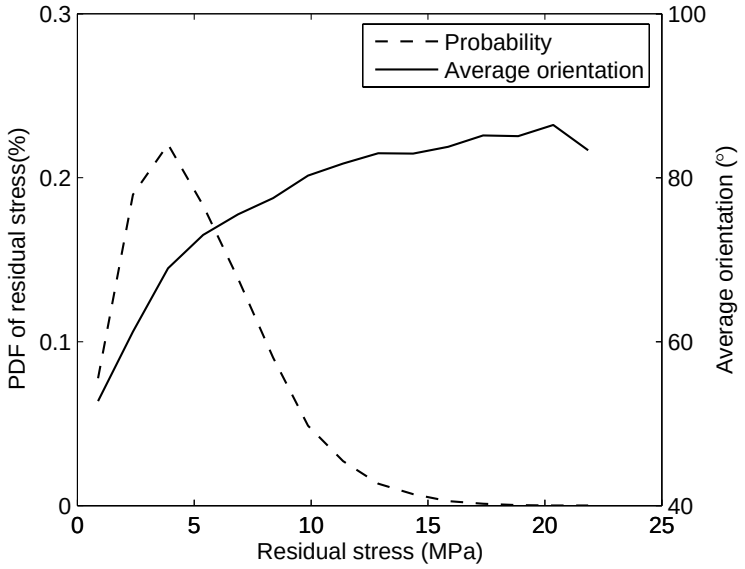

(b) EFG

Figure 72: Probability distribution of the magnitude of residual stress in a silicon ribbon

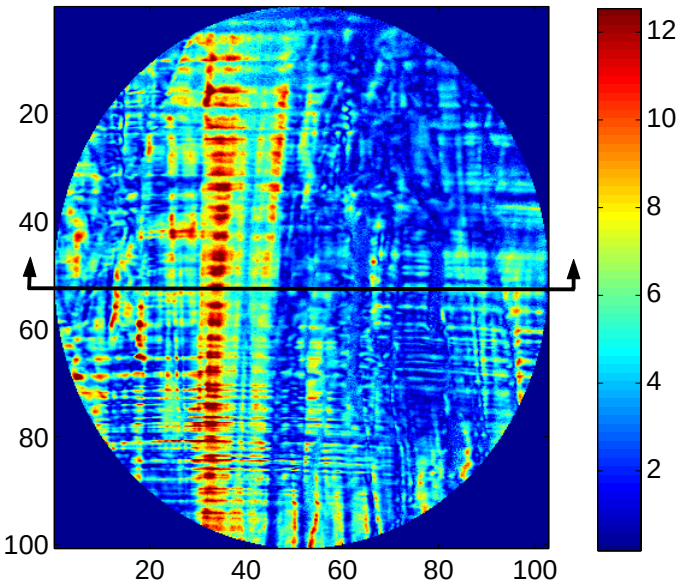

Figure 73: Residual stress distribution of an EFG wafer, a scan through the central region as shown in this figure is shown in Figure 74

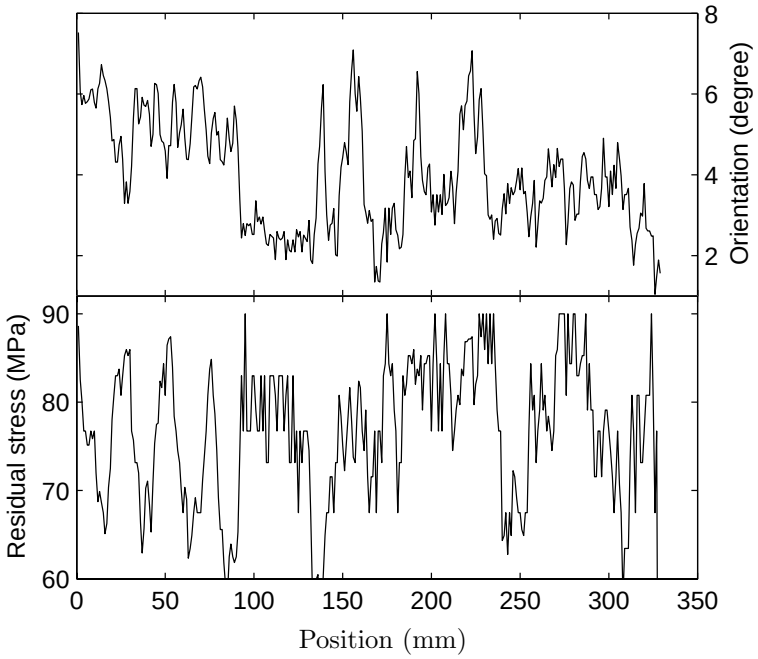

Figure 74: Magnitude and orientation of the residual stress at an arbitrary section perpendicular to the growth direction

7.3 Photoluminescence (PL) in Silicon

The electron-hole lifetime is another parameter that is related to cell efficiency and it is believed to be linked to the residual stresses. The measurement was carried out by Dr. Ostapenkon and his group in the University of South Florida using room temperature photoluminescence (PL) [71]. Figure 75 shows the schematic diagram of the experimental setup. The excitation source of the room temperature PL is an InGaAr infrared diode with a wavelength of 810 nm and power up to 130 nW. The emission is captured using photomultiplier tube at 400 nm to 800 nm spectral range and liquid nitrogen cooled Ge-diode at 800 nm to 1,700 nm. Full field mapping is accomplished by using an X-Y translation stage. Previous research [71] shows that the band-to-band PL intensity, $h\nu_{max} = 1.09eV$, in crystalline silicon at room temperature is proportional to the effective minority carrier lifetime, therefore, these measurements can serve as an independent parameter to track the evolution in the electronic qualities. The spatial resolution is adjustable between 60 μm and 1 mm, which is determined by the size of the focus spot of the excitation laser diode. The distribution of the bulk lifetime (diffusion length) was measured by the surface photovoltage (SPV) technique. However, the success of this technique is critically dependent on the surface condition, i.e. surface recombination velocity, and not all samples show a detectable SPV signal.

Figure 76 shows the typical distribution of the photoluminescence in different types of photovoltaic silicon. The photoluminescence has the same characteristics in spatial distribution as the residual stresses. As shown in Figure 69(a)) and (Figure 69(b)), the photoluminescence of cast and CZ silicon are relatively uniform, while the string ribbon (Figure 69(c)) and EFG (Figure 69(d)) silicon have substantially higher spatial variation. It is interesting that a ring pattern is also observed in PL images of CZ-Si wafers, which may indicate the appearance of the "ring" defects and could be attributed to a boundary between vacancy and interstitial-enriched wafer regions.

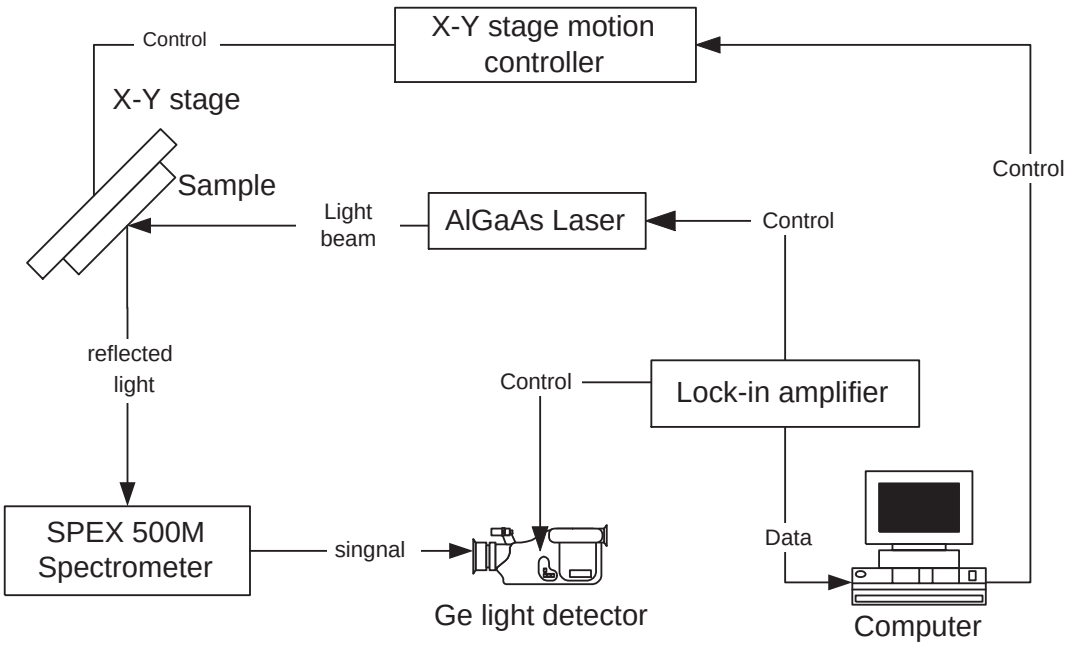

Figure 75: The schematic diagram of the experimental setup of photoluminescence

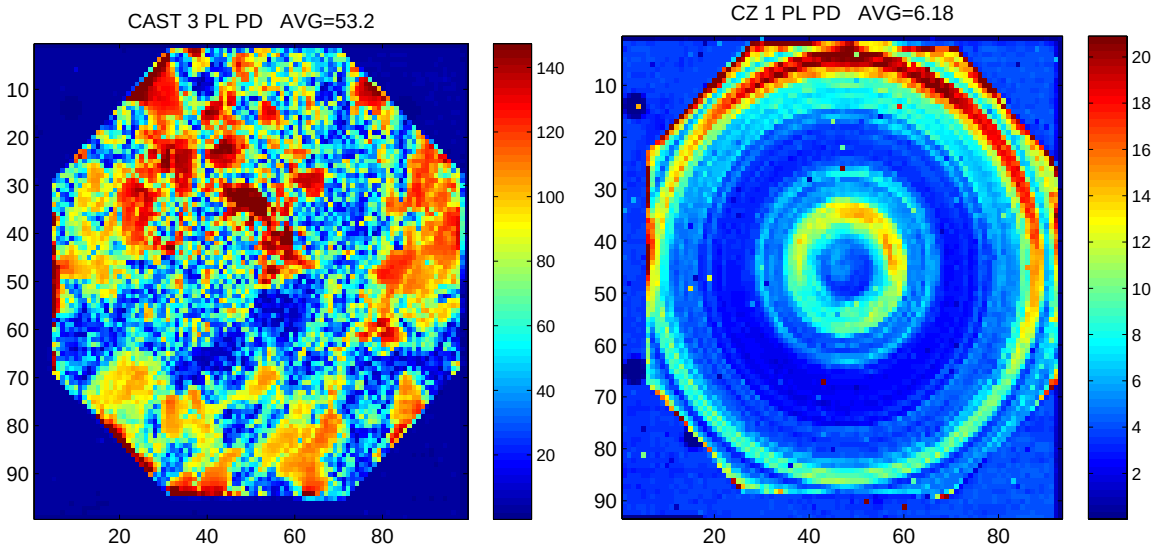

(a) CAST (b) CZ

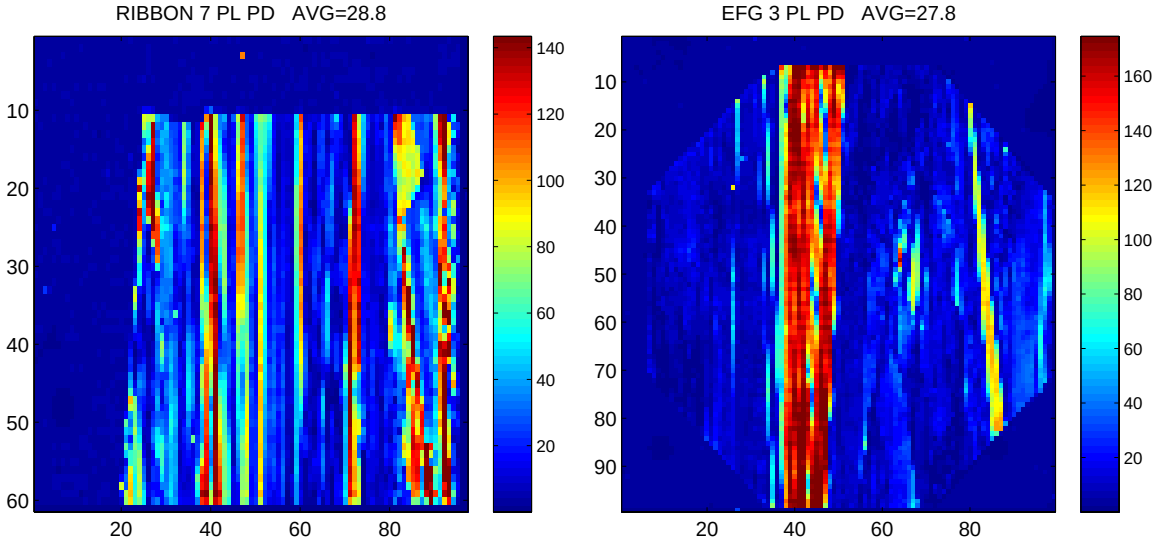

(c) Ribbon (d) EFG

Figure 76: The typical mapping of the photoluminescence of various photovoltaic silicon

7.4 Correlation between Residual Stresses and Photoluminescence

A clear correlation between the residual stresses and photoluminescence is observed for ribbon silicon shown in Figure 77 and EFG silicon shown in Figure 78. The high residual stress areas are correlated to the high PL and SPV, or high lifetime areas. This correlation is more apparent for EFG and ribbon wafers which have a higher average residual stress. The reason for this correlation is that in the high residual stress areas, the residual stress is not released; therefore this generates fewer defects which act as recombination centers and impair the minority lifetime.

Since both the residual stresses and photoluminescence in ribbon and EFG silicon are relatively uniform along the crystal growth direction, the average along this direction can be illustrative to demonstrate their correlation quantitatively. Figure 79 shows the average residual stress and photoluminescence along the growth direction. The two curves have the same trend and the locations of peaks are closely matched. The quantitative correlation can be obtained by comparing the residual stress and the photoluminescence point-by-point. Figure 80 shows this correlation by taking residual stress and photoluminescence as the two axes. The solid line shows the least square fit of the data. The correlation coefficient of this fit is moderate, 0.8, but a linear tendency between the residual stress and PL is clearly observed.

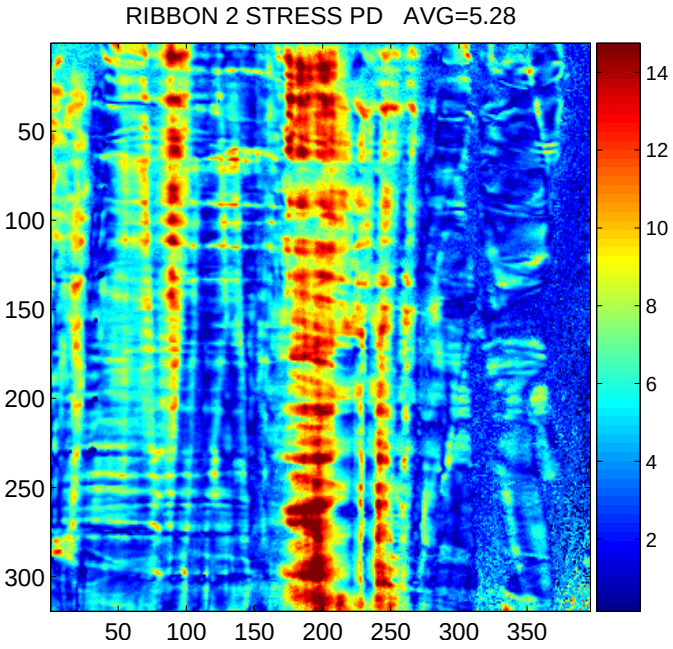

(a) Residual stress (MPa)

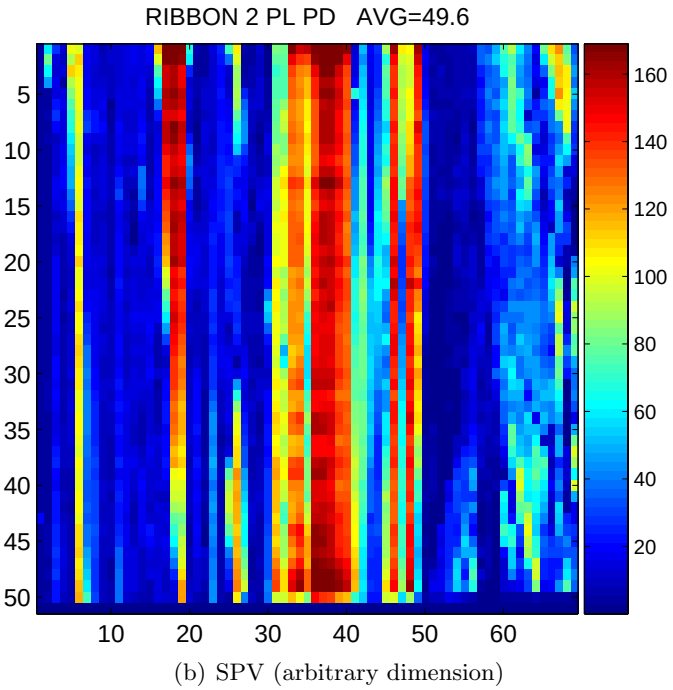

(b) SPV (arbitrary dimension)

Figure 77: The correlation between residual stress and photoluminescence of *ribbon* silicon

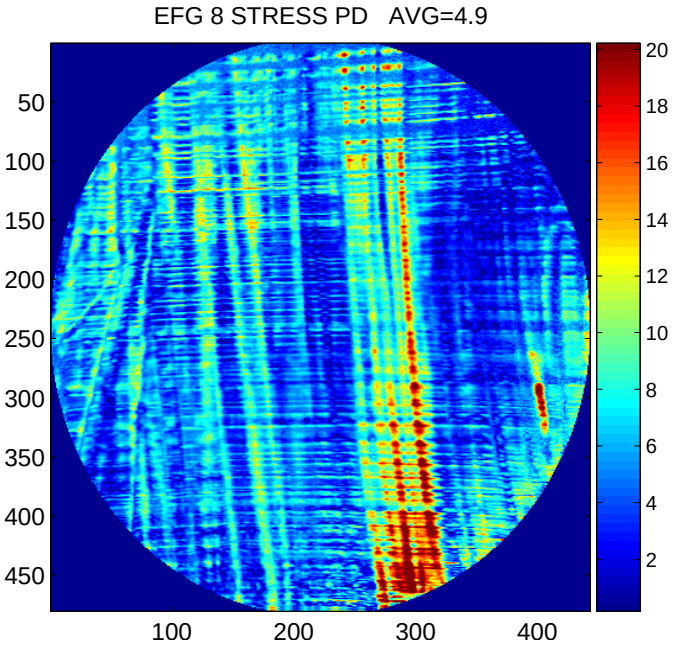

(a) Residual stress (MPa)

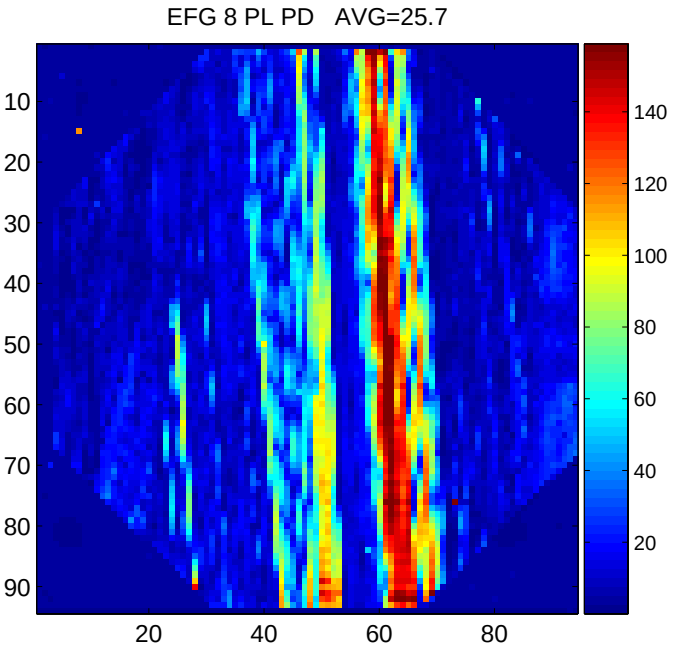

(b) SPV (arbitrary dimension)

Figure 78: The correlation between residual stress and photoluminescence of *EFG* silicon

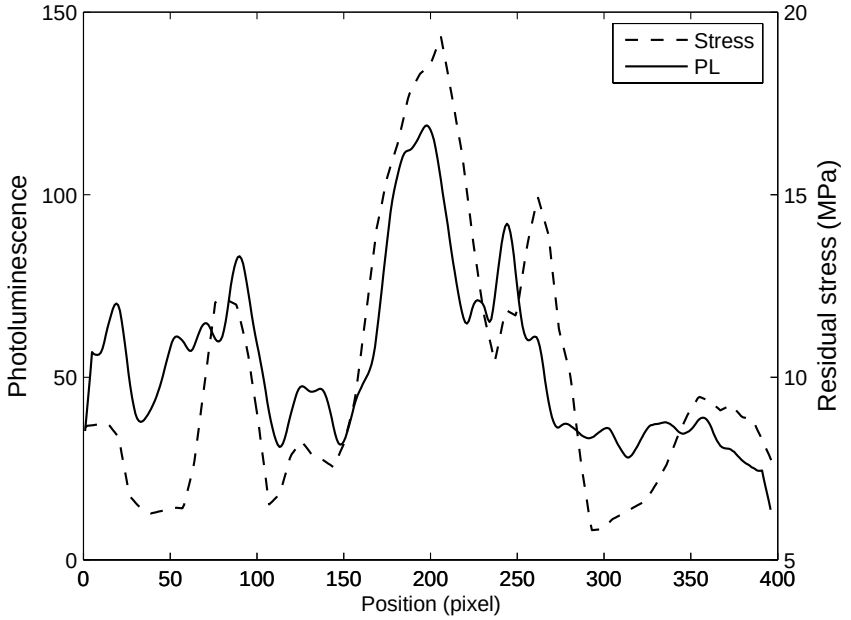

(a) Ribbon

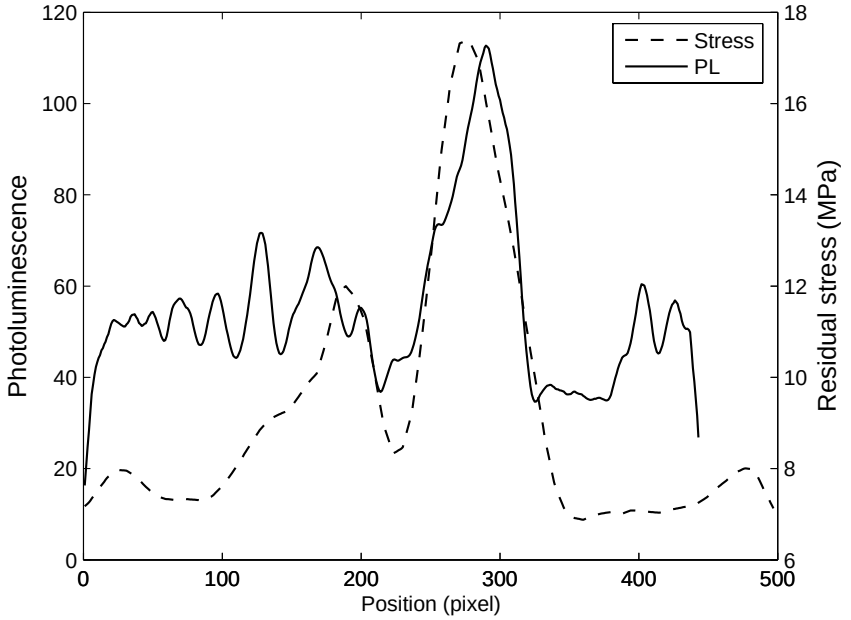

(b) EFG

Figure 79: Correlation between average residual stress and PL

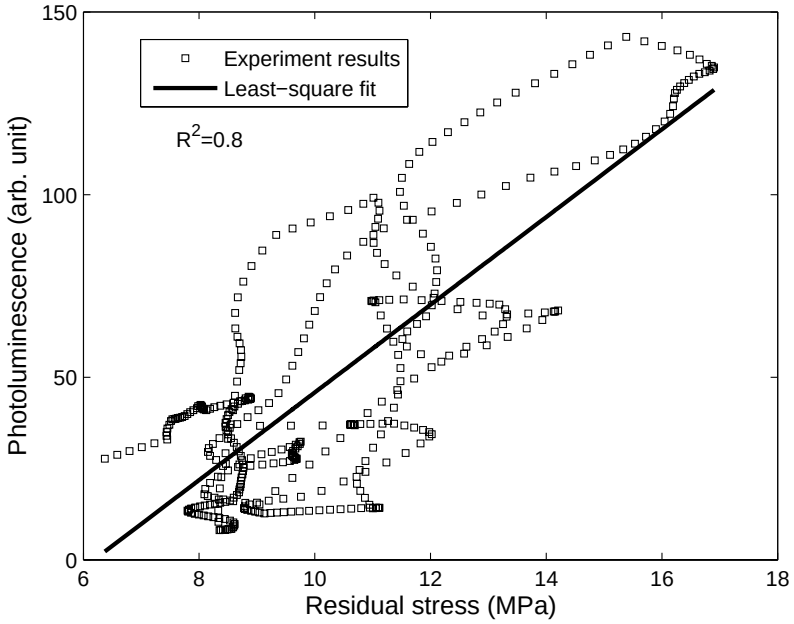

(a) Ribbon

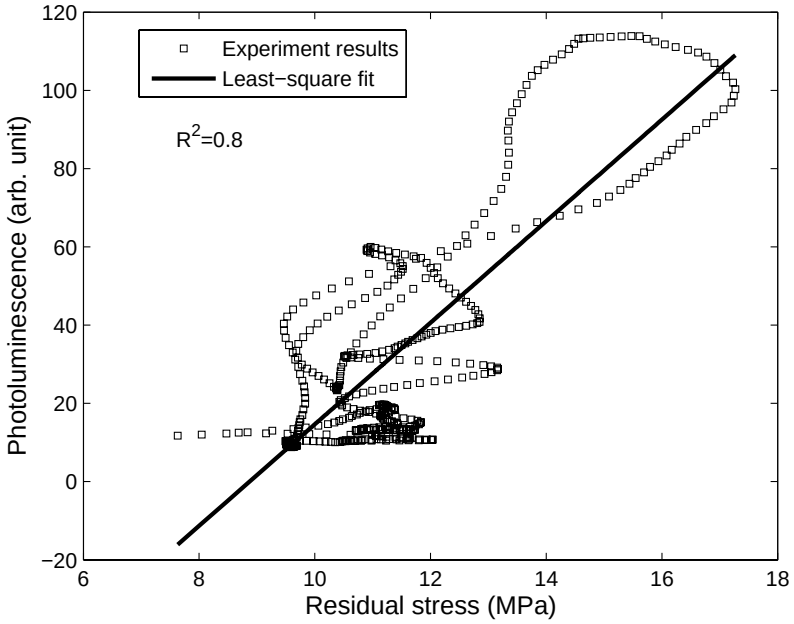

(b) EFG

Figure 80: Correlation between average residual stress and PL

7.5 Residual stress, PL and SPV monitoring in PV manufacturing

The flow chart of the research on the evolution of the residual stress and PL intensity in photovoltaic manufacturing is shown in Figure 81. Three CZ-Si wafers, ten cast, nine EFG and ten Ribbon samples were obtained from RWE Schott, Evergreen Solar, BP Solar and EBARA Solar respectively. The wafers are being processed at the Georgia Tech University Center of Excellence for Photovoltaic Research (UCEP). The major manufacturing steps involve cleaning & etching, diffusion, anti-reflection coating and front & back surface contact. The data were processed using a program *DataProcessing* developed in Matlab. The interface of the program is shown in Figure 82.

The maximum and average values of residual stress, PL and SPV are shown in Table

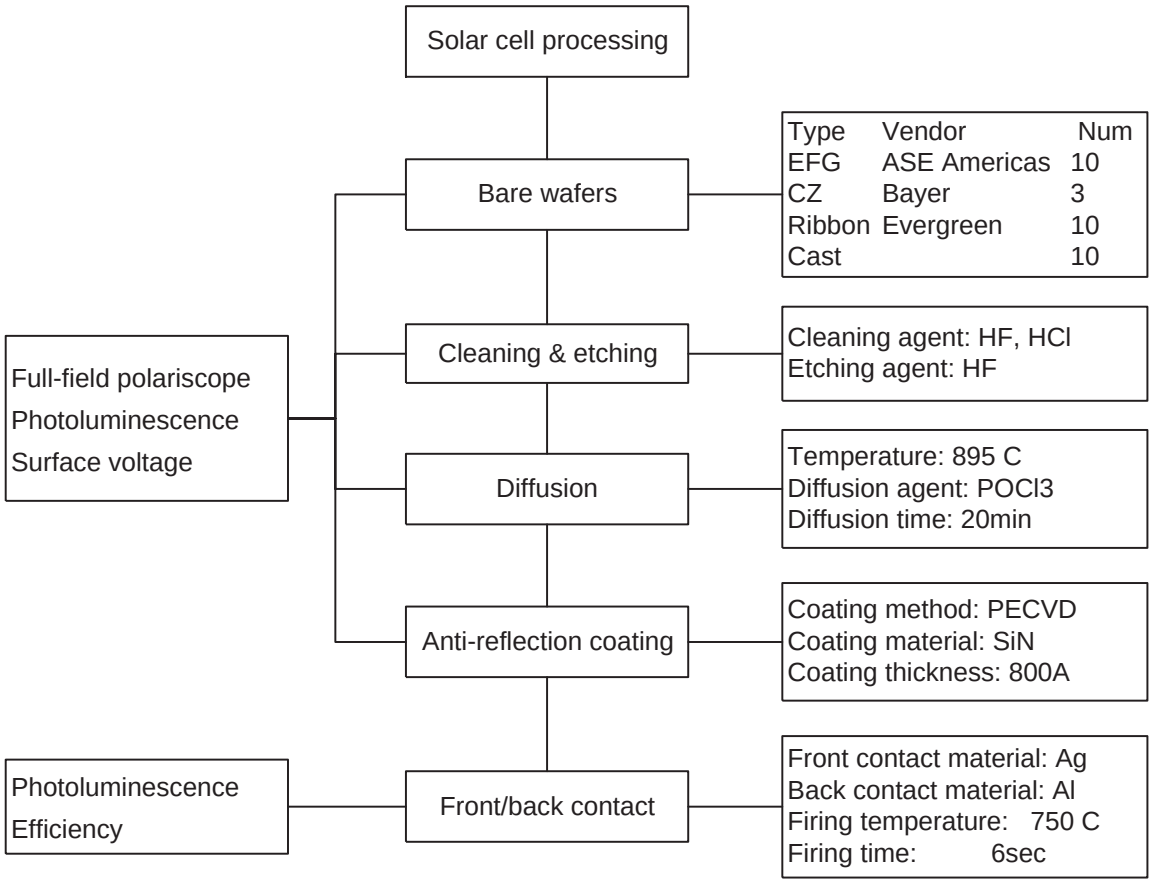

Figure 81: Solar cell processing flow chat

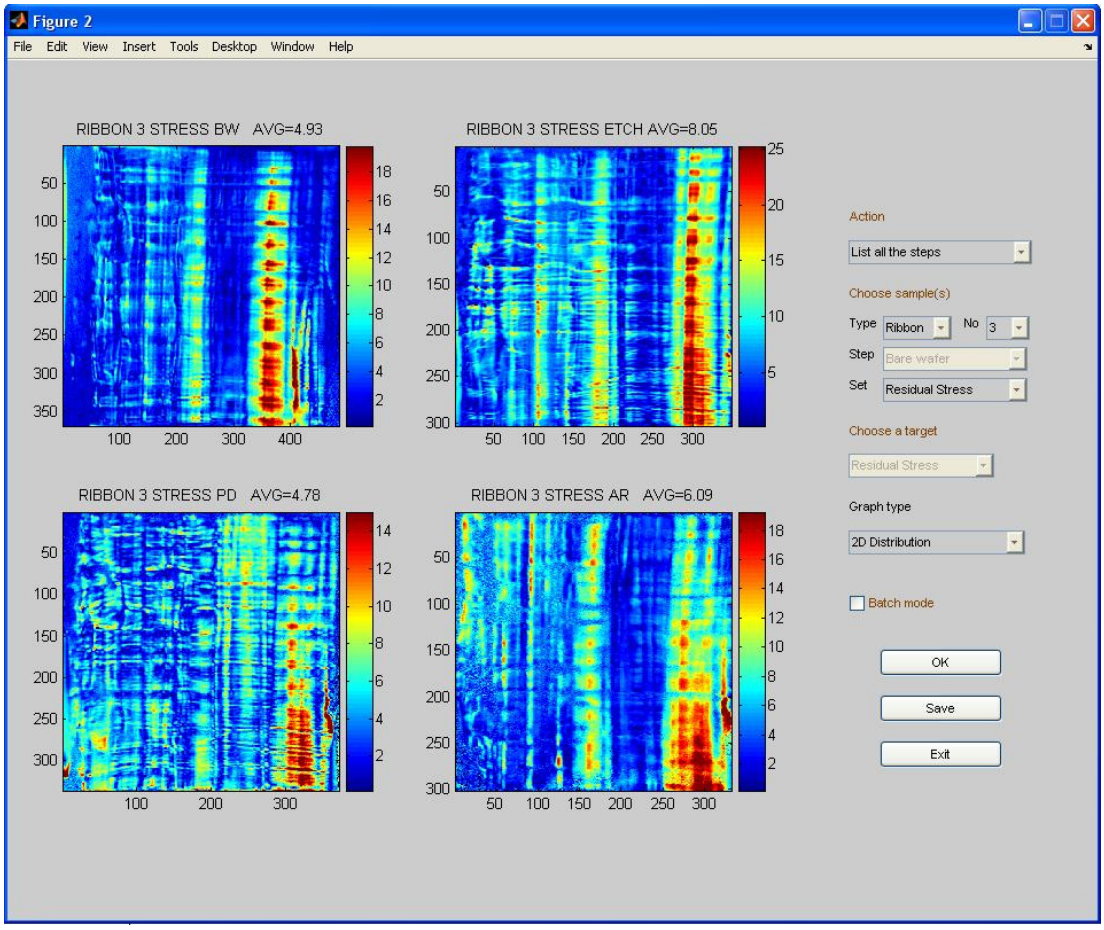

Figure 82: Solar cell processing flow chat

11 and 12 respectively for cast, CZ, EFG and string ribbon wafers. As can be seen in Table 11, there is a significant decrease in both the maximum and average residual stress for the cast and CZ samples after etching & cleaning, while a slight increase in both values was observed in the EFG and ribbon wafers. It is hypothesized that the etching & cleaning processing removed the top layer which was heavily damaged by the sawing process.

Figure 83 to 86 summarize the distribution of the residual stress, PL and SPV for selected samples. The results of the SPV after certain processing steps are not shown because the SPV signals are below the sensitivity of the system due to the change in surface condition in processing. As shown in Table 12, a slight decrease in the PL is observed after the cleaning and etching step. This decrease in PL is mainly caused by the increase of the surface recombination velocity, which reduces the effective lifetime, because the cleaning and etching does not change the bulk lifetime. On the other hand, more than a 10-fold increase in PL intensity is observed in all samples except CZ-Si after P-diffusion. This increase is attributed to the upgrade of bulk lifetime due to the phosphorous gettering mechanism. However, the lifetime of CZ-Si wafers can not be upgraded because the single crystal has much better quality and there are not many defects available for gettering.

PL mapping profile maintained unchanged after cleaning, P-diffusion and AR-coating steps. The average value of PL intensity is gradually increased corresponding to upgrade of the bulk and surface recombination lifetime, considering that $I_{\mathrm{PL}} \sim \tau_{\mathrm{eff}}$, and

$$\tau_{\mathrm{eff}}^{-1} = \tau_{\mathrm{bulk}}^{-1} + \tau_{\mathrm{surface}}^{-1} \tag{84}$$

This effect has been studied previously [72]. After metallization and Al-firing, the PL maps are changed dramatically. They became more homogeneous, although the average PL intensity (lifetime) was reduced in all samples. The most dramatic reduction is observed in a case of cast wafers ($\sim$5 fold reduction). This can be attributed to the dissolution of defect clusters from contaminated dislocations, which reduce the recombination activity of the dislocations, but in return degrade the "good regions" of the wafers.

Table 11: Maximum and average residual stresses in silicon sheet during processing

No.	t (μm)	Maximum (MPa)				Average (MPa)			
		Bare	Etched	Diffused	AR	Bare	Etched	Diffused	AR
Cast wafers									
1	0.326	11.79	9.07	8.09	12.45	2.67	1.34	1.62	5.51
2	0.325	12.96	5.64	7.55	12.08	2.69	1.17	1.57	5.59
3	0.325	16.03	8.15	8.77	12.00	3.32	1.31	1.61	5.42
4	0.326	14.84	6.75	7.43	12.52	3.18	1.27	1.60	5.60
5	0.328	12.45	6.54	7.31	12.17	2.34	1.26	1.60	5.69
6	0.327	10.89	6.56	8.32	12.40	2.65	1.26	1.49	5.45
7	0.326	11.67	6.91	6.34	12.45	2.75	1.25	1.40	5.48
8	0.328	14.11	9.30	9.80	N/A	3.97	1.67	1.77	N/A
9	0.325	16.67	7.09	6.87	13.19	2.46	1.52	1.49	6.75
10	0.346	10.19	7.57	9.39	11.09	2.15	1.66	1.75	5.10
CZ wafers									
1	0.319	23.84	6.82	8.79	11.11	4.68	1.52	1.62	3.66
2	0.322	18.87	6.86	8.08	9.63	4.52	1.09	1.51	3.50
3	0.321	18.23	7.76	7.13	9.36	4.73	1.94	1.26	2.93
EFG wafers									
1	0.260	15.28	19.56	17.84	17.29	2.25	3.25	2.98	3.36
2	0.305	7.13	13.29	14.85	9.83	1.32	2.38	2.19	2.15
3	0.256	11.15	13.79	14.91	12.21	1.93	2.79	2.81	3.98
4	0.240	13.38	20.85	16.40	18.24	2.06	3.52	2.75	3.38
5	0.265	10.21	18.45	10.91	9.03	1.29	2.36	1.43	3.84
6	0.279	12.17	15.97	24.85	14.68	1.55	2.97	2.96	3.23
8	0.258	13.78	17.64	19.81	16.78	2.07	3.65	2.85	3.77
9	0.291	10.34	11.72	16.01	N/A	1.43	2.47	2.31	N/A
10	0.280	13.84	20.08	16.22	12.39	2.17	3.46	3.79	3.20
String Ribbon wafers									
1	0.276	12.35	20.70	13.78	13.91	2.58	5.06	3.53	3.41
2	0.296	11.45	16.65	11.71	15.01	2.30	4.39	3.18	3.04
3	0.281	19.11	19.85	14.89	16.52	2.89	4.59	2.82	3.63
4	0.288	16.96	23.49	14.27	16.07	2.93	5.25	2.78	3.68
5	0.302	8.62	23.51	17.18	16.08	2.07	2.58	2.48	2.04
6	0.326	16.11	13.36	12.48	17.28	2.88	2.92	2.63	1.88
7	0.269	16.81	18.94	19.71	17.19	2.38	5.59	3.45	3.52
8	0.288	17.98	25.01	15.77	14.61	2.86	4.79	2.79	3.81
9	0.277	12.15	19.88	13.97	19.78	2.51	3.98	3.41	3.49
10	0.280	11.71	17.62	10.82	14.96	2.39	3.71	2.88	3.30

Table 12: Average values of band-to-band PL intensity and minority carrier diffusion length measured by SPV technique

No.	Bare		Cleaning Etching		P-diffusion	AR coating
	PL	SPV (mV)	PL	SPV (mV)	PL	PL
CZ						
1	14.67	N/A	6.19	123.78	6.48	28.82
2	15.22	N/A	26.25	123.58	6.09	29.11
3	15.53	N/A	10.30	111.56	3.65	25.66
Cast						
3	8.93	N/A	6.87	105.28	66.72	141.99
4	8.31	N/A	7.10	107.87	63.88	139.35
6	7.94	N/A	6.19	112.34	58.87	120.80
7	8.55	N/A	5.60	114.22	51.60	114.82
8	8.67	N/A	5.15	112.46	55.79	broken
10	8.12	N/A	5.28	88.02	56.88	125.32
EFG						
1	6.71	40.88	2.25	40.17	23.54	66.76
2	5.23	23.41	2.04	34.03	21.18	59.85
3	8.47	43.12	2.44	40.70	36.49	86.57
5	4.90	36.97	2.72	39.03	25.97	69.43
6	3.90	40.70	2.06	39.64	21.47	59.76
8	4.43	39.82	2.24	41.66	31.05	78.95
Ribbon						
2	2.30	N/A	1.17	N/A	50.63	119.61
3	2.62	N/A	1.23	N/A	63.01	118.99
5	4.26	N/A	3.11	N/A	41.41	98.83
7	3.40	N/A	1.54	N/A	39.32	105.87
8	3.96	N/A	1.54	N/A	54.21	119.98

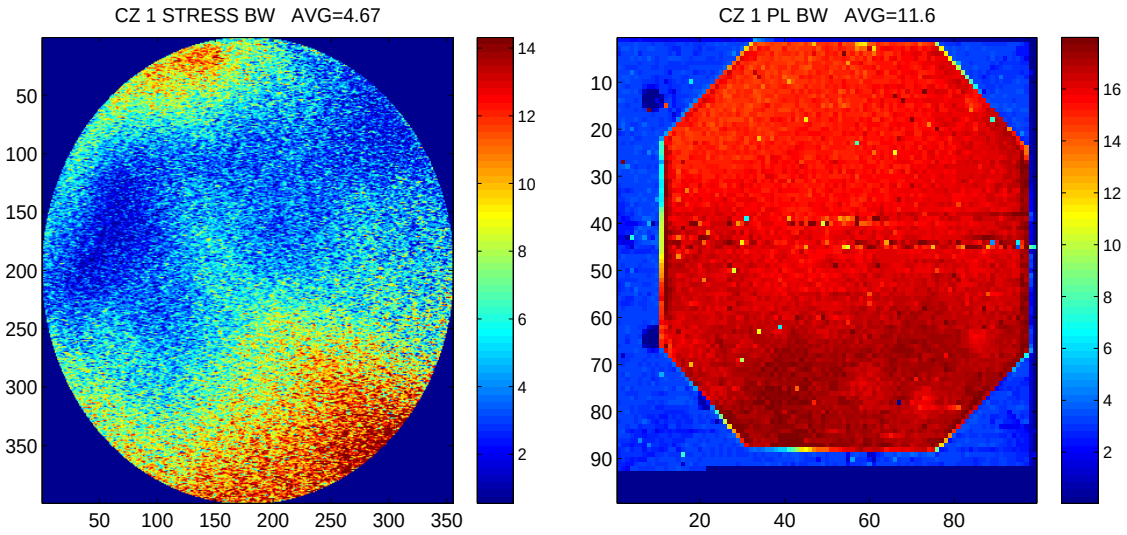

(a) Bare wafer

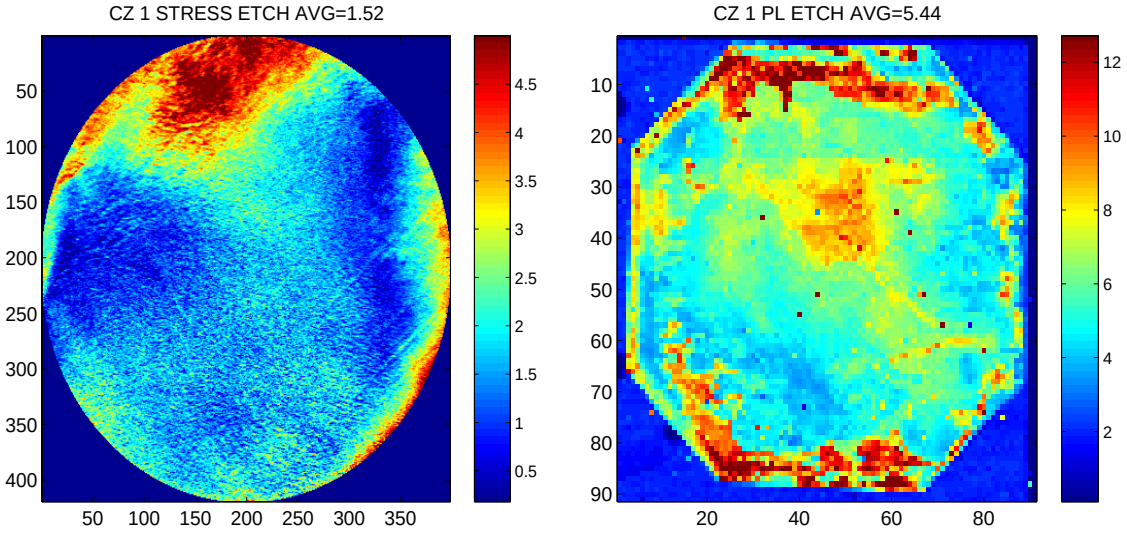

(b) Etched wafer

Figure 83: Residual stress [MPa] (first column) and PL [arbitrary unit] (second column) of CZ #1

Figure 83 continued...

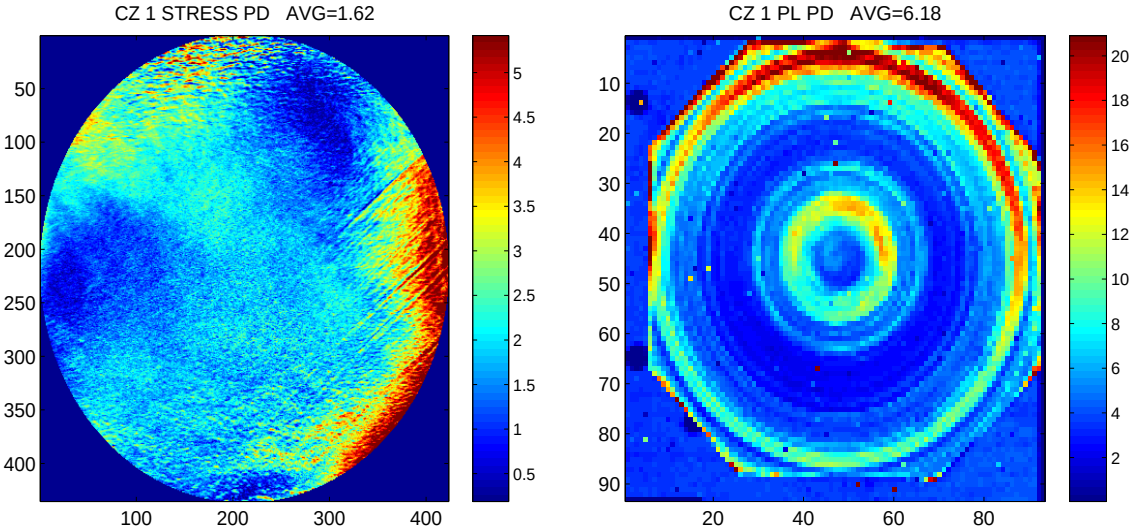

(c) Diffused wafer

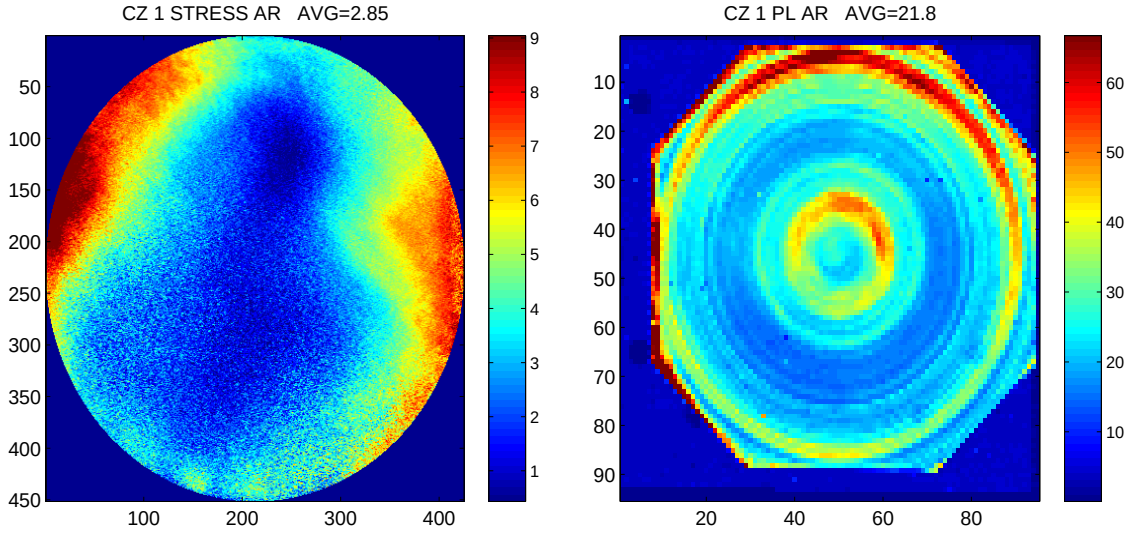

(d) Anti-reflection coated wafer

Figure 83: Residual stress [MPa] (first column) and PL [arbitrary unit] (second column) of CZ #1

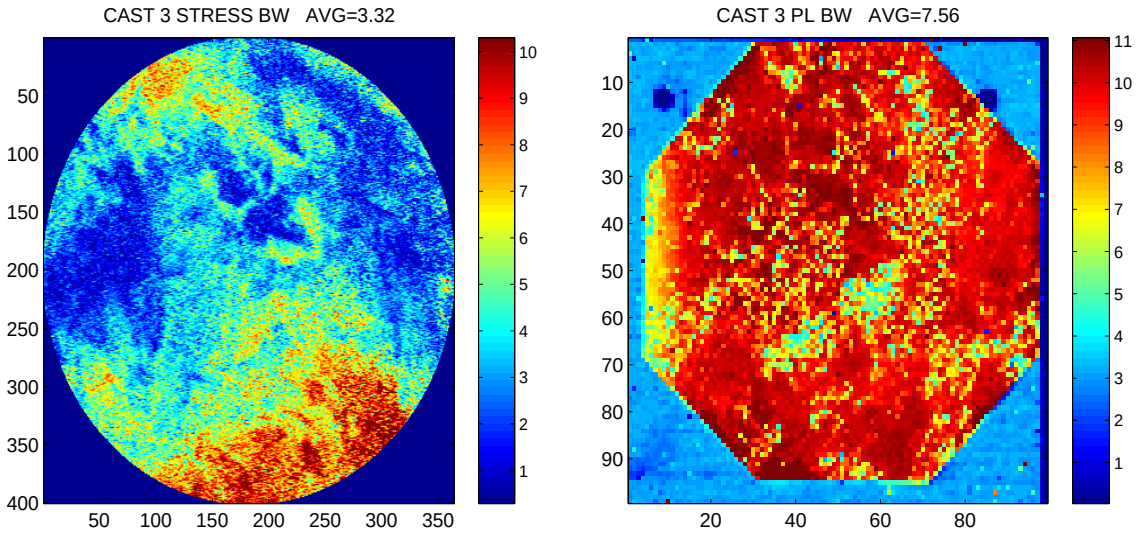

(a) Bare wafer

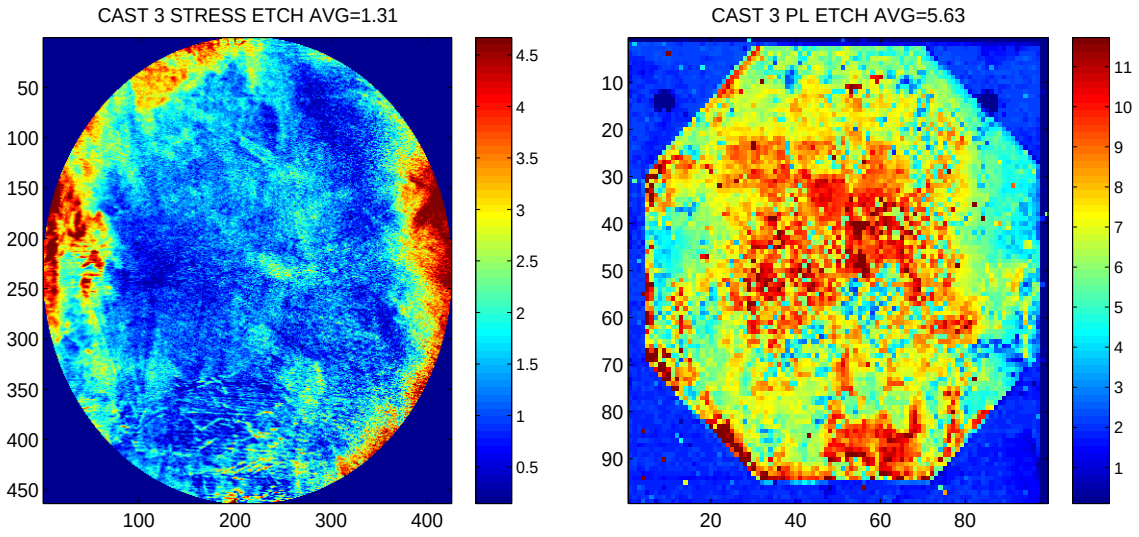

(b) Etch wafer

Figure 84: Residual stress [MPa] (first column) and PL [arbitrary unit] (second column) of cast #3

Figure 84 continued...

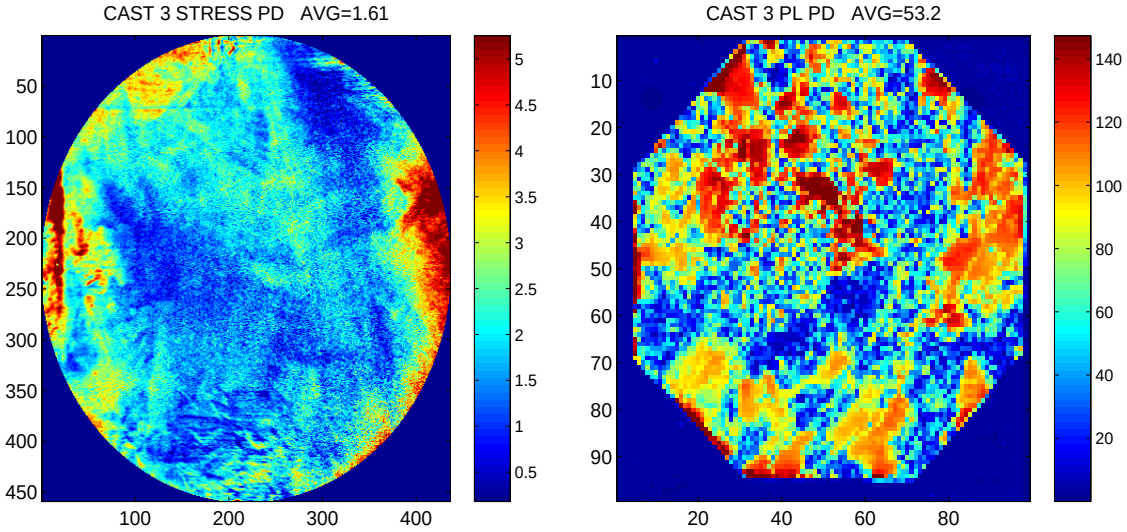

(c) Diffused wafer

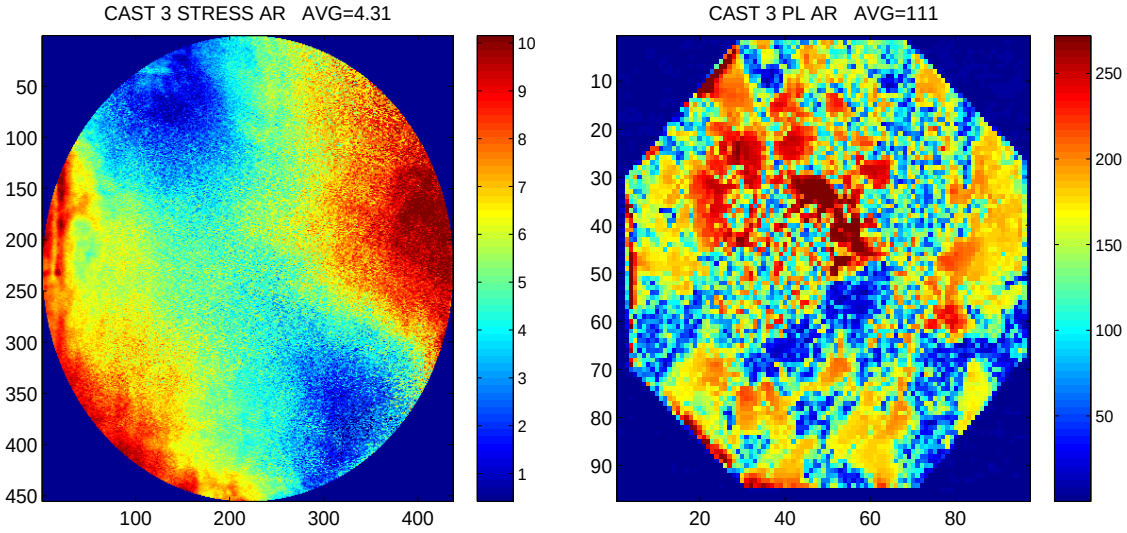

(d) Anti-reflection coated wafer

Figure 84: Residual stress [MPa] (first column) and PL [arbitrary unit] (second column)of cast #3

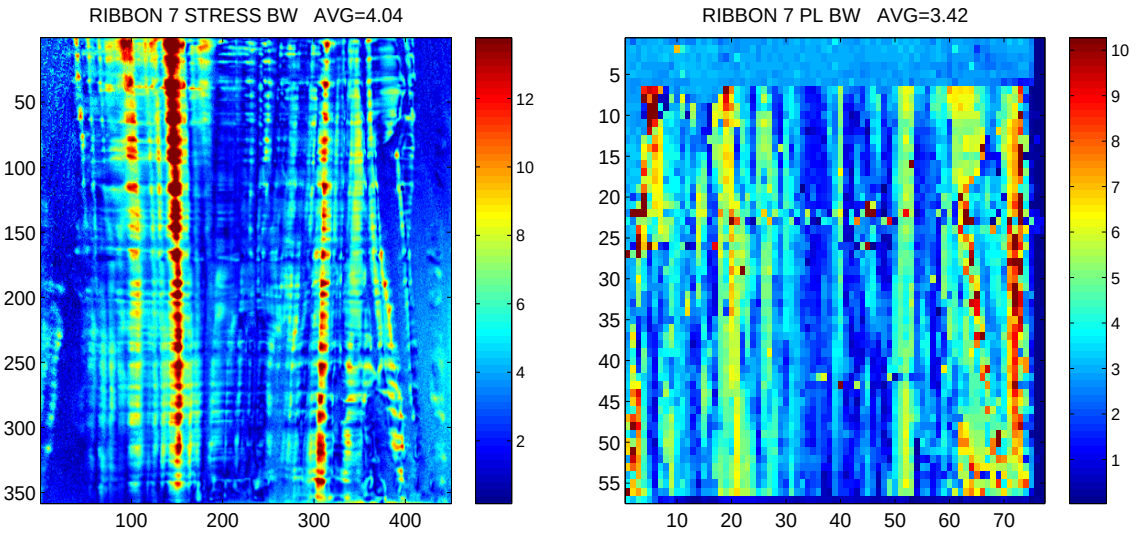

(a) Bare wafer

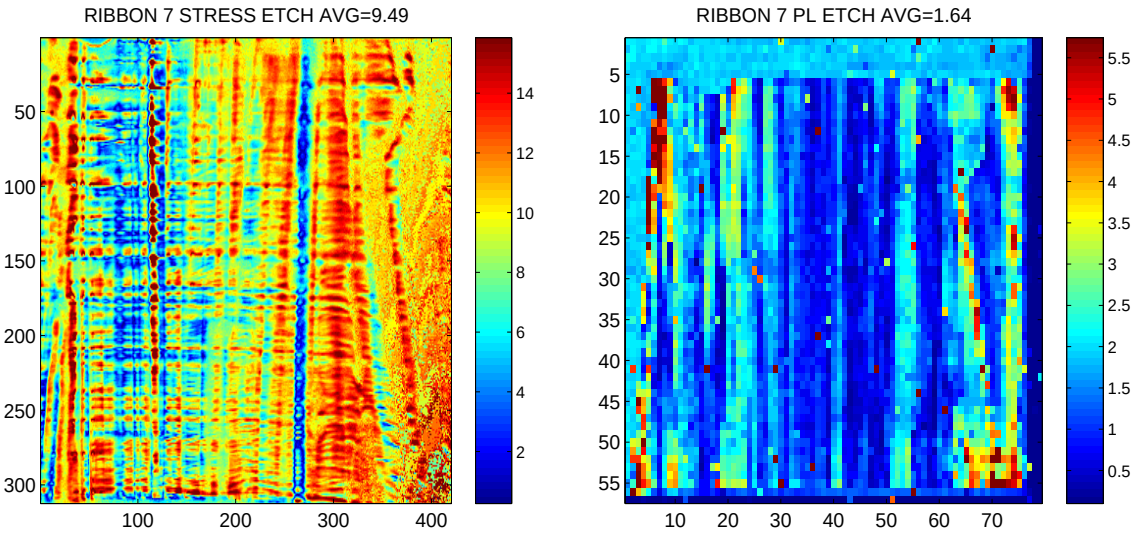

(b) Etch wafer

Figure 85: Residual stress [MPa] (first column) and PL [arbitrary unit] (second column) of Ribbon #7

Figure 85 continued...

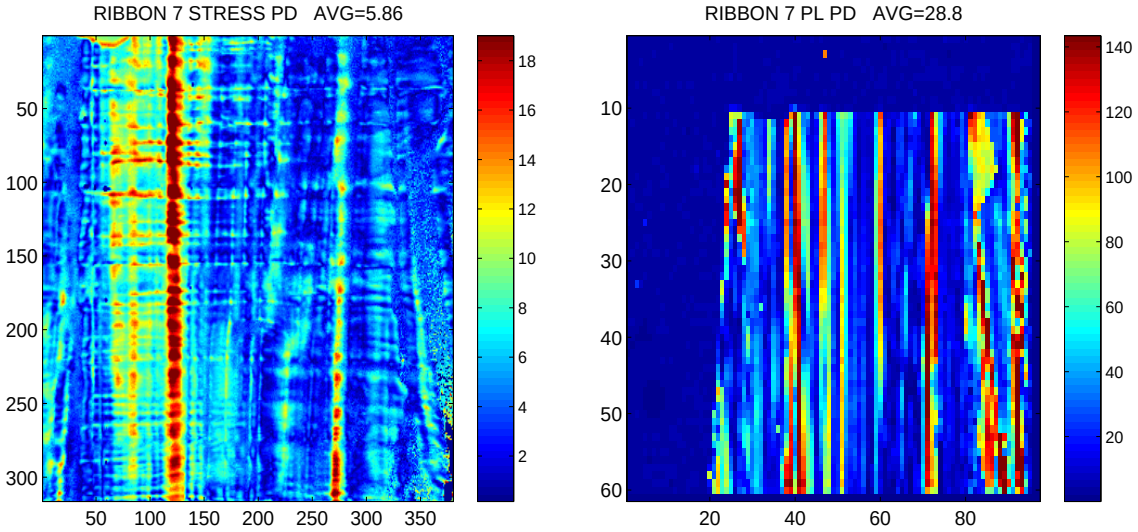

(c) Diffused wafer

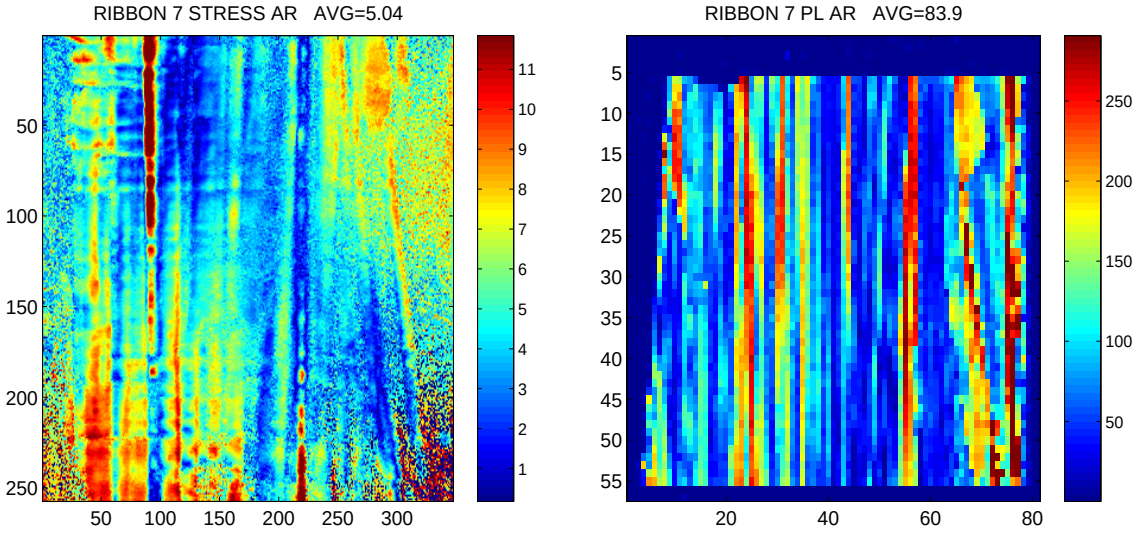

(d) Anti-reflection coated wafer

Figure 85: Residual stress [MPa] (first column) and PL [arbitrary unit] (second column) of Ribbon #7

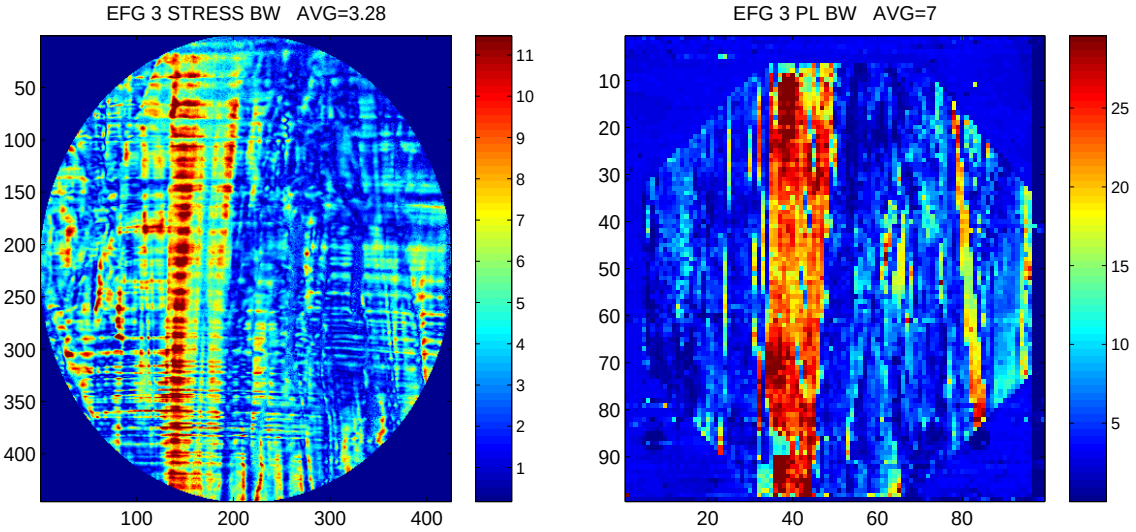

(a) Bare wafer

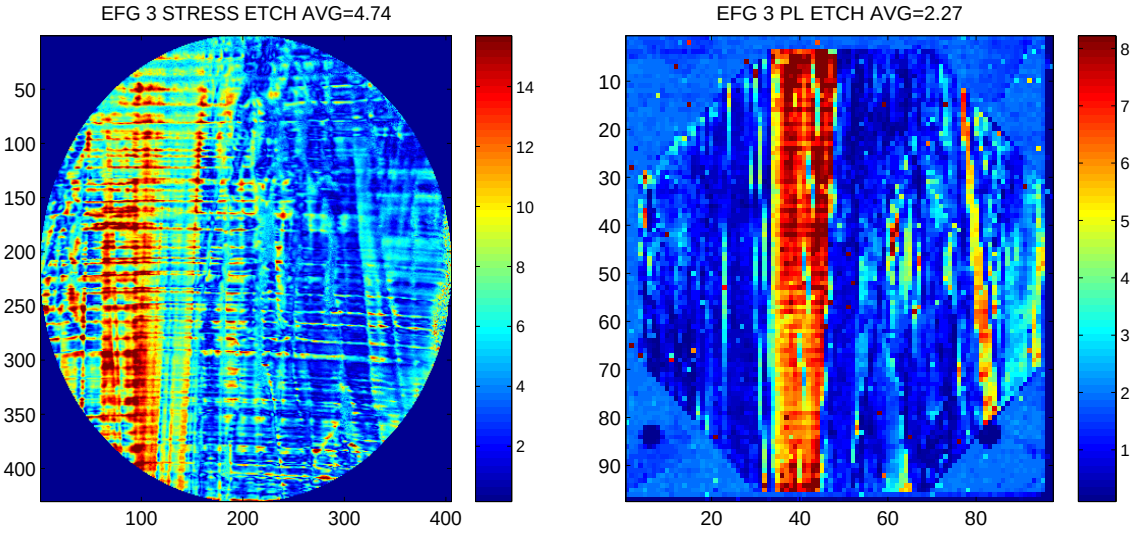

(b) Etch wafer

Figure 86: Residual stress [MPa] (first column) and PL [arbitrary unit] (second column) of EFG #3

Figure 86 continued...

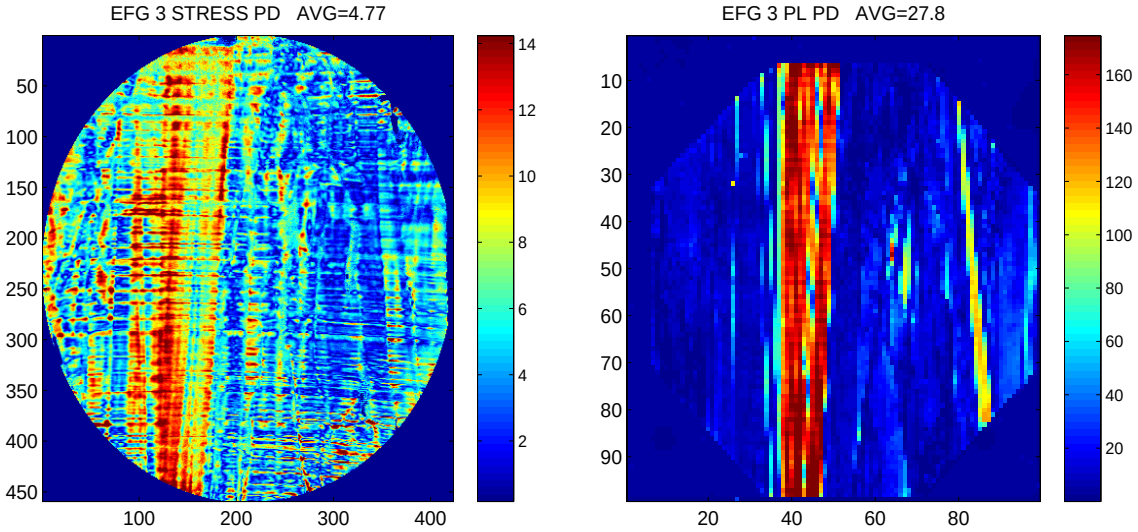

(c) Diffused wafer

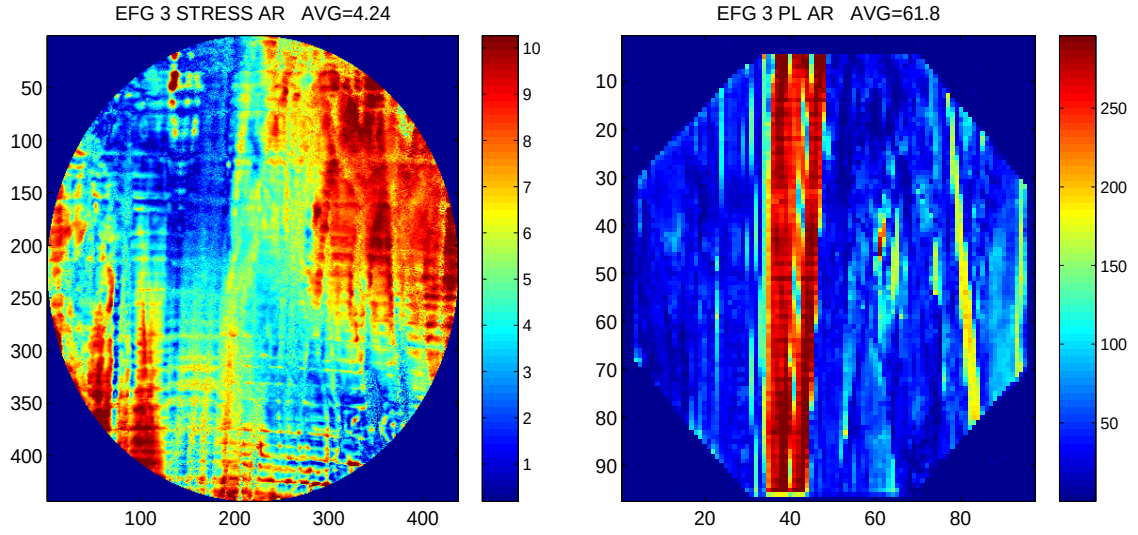

(d) Anti-reflection coated wafer

Figure 86: Residual stress [MPa] (first column) and PL [arbitrary unit] (second column) of EFG #3

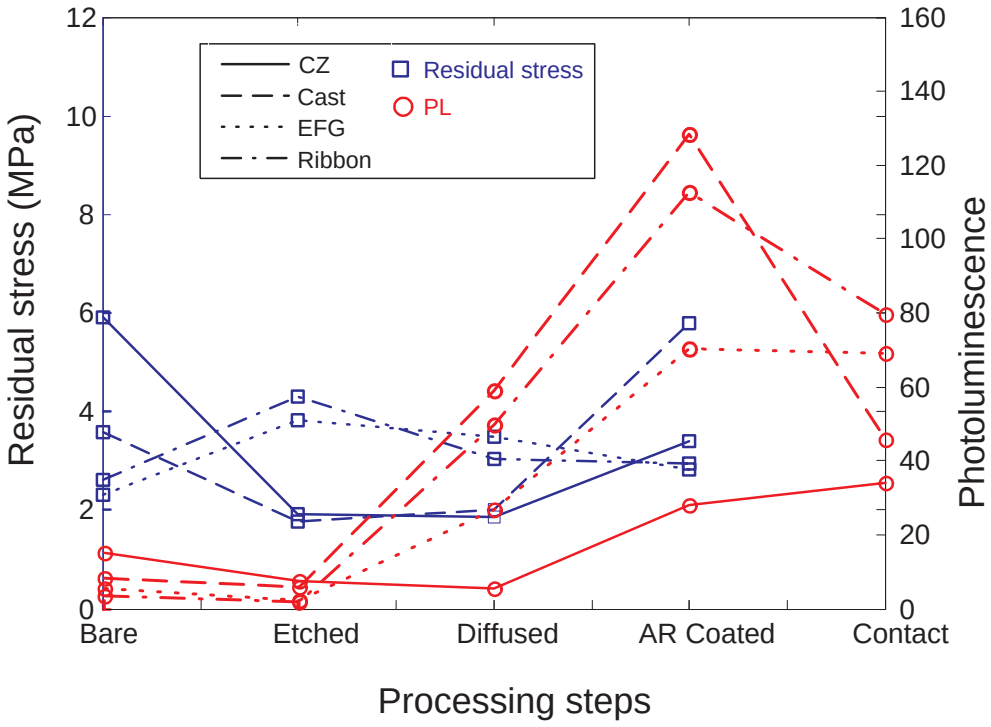

Figure 87: Evolution of residual stresses and PL with processing

Figure 87 and Table 13 show the average residual stress and PL of samples of the same type after processing. The four types of silicon are divided into two groups. The CZ and cast silicon are one group, which has similar pattern in the evolution of the residual stress and PL, and the string ribbon and EFG silicon are the other group. Once again a substantial decrease in residual stress is observed for CZ and cast silicon after etching, while the PL remains at the same level. The effects of phosphorous gettering and surface passivation on the PL are clearly observed in the figure. The PL was reduced by half due to the increase of surface recombination velocity after metal contact.

7.6 The Correlation between Residual Stress, Photoluminescence and Efficiency

Figure 88 shows the image of the front surface of a photovoltaic cell. The grids on the surface are the metal contact fingers. On each wafer, nine small cells, or sub-cells with a size of 20 × 20 mm, were fabricated. The layout the nine sub-cells is shown in Figure 89.

Table 13: Evolution of residual stress and PL with processing

Sample type	Bare	Etched	Diffused	AR coated	Contact
Average residual stress (MPa)					
CZ	5.92	1.93	1.87	3.41	N/A
Cast	3.59	1.76	2.02	5.80	N/A
EFG	2.32	3.81	3.48	2.81	N/A
Ribbon	2.61	4.31	3.02	2.94	N/A
Average PL (arbitrary unit)					
CZ	15.14	7.58	5.41	27.86	33.91
Cast	8.42	6.03	58.96	128.46	45.87
EFG	5.61	2.29	26.62	70.22	69.24
Ribbon	3.31	1.72	49.72	112.66	79.43

Grooves were cut between the each sub-cell to separate them so that the efficiency can be measured every individual sub-cell.

The efficiency measurement gives a 3×3 mapping of the whole PV cell, while the PL and residual stress mapping have 80×80 and 500×500 pixels respectively. The mapping of the PL and residual stress should be divided into 3×3 sections and the averages of these sections are used to match the efficiency mapping. Figure 90 shows the alignment of the sub-cells on a PL image. The red squares shows the positions of the nine sub-cells. The effect of the contact fingers are also observed is the figure.

The efficiencies of the cast and EFG silicon are shown in Table 14. There are no valid data available for the string ribbon silicon because the samples were contaminated. The these happened to CAST8, EFG9 and some sub-cells. The sub-cells with an efficiency below 14.5% will not be counted because they the efficiency is below the normal level, which is around 16%.

The correlation between residual stress, PL and efficiency is shown in Figure 91 and 92 for cast silicon, Figure 93 and 94 for EFG silicon. For both cast and EFG silicon, a positive correlation between residual stress, PL and efficiency was observed. The linear fits between the residual stress and efficiency, PL and efficiency are shown as the solid lines in

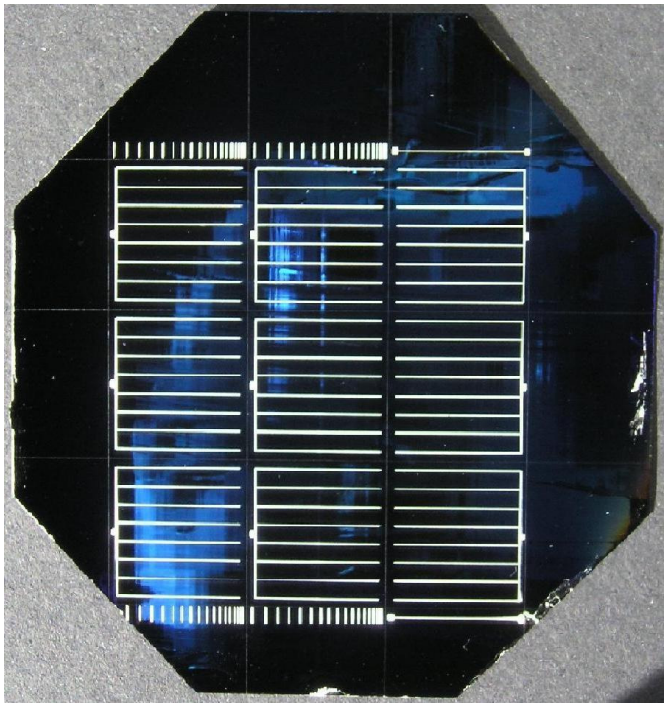

Figure 88: The image of a photovoltaic cell

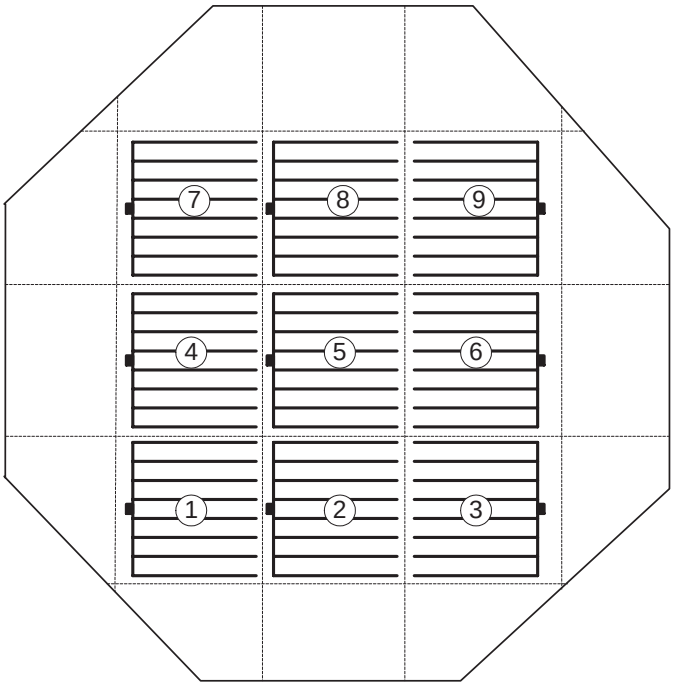

Figure 89: The layout of nine sub-cells on a photovoltaic cell. Grooves (dash lines) were cut between the sub-cells to separate them.

Table 14: The efficiency of the cast and EFG silicon

CAST										
No	Sub-cell Efficiency (%)									Avg♮ (%)
1	16.1	15.7	15.4	15.7	15.3	15.5	15.8	15.7	15.8	15.7
2	14.6	15.5	15.3	13.5	15.5	15.6	15.8	16.1	15.8	15.7
3	15.9	15.3	14.9	15.1	15.2	15.4	14.8	14.5	14.9	15.2
4	15.8	15.8	15.8	10.9	15.4	15.8	15.9	16.2	16.1	15.8
5	15.9	16.2	12.6	16.2	16.4	16.1	-	16.4	16.4	16.2
6	15.9	15.7	15.8	16.4	16.2	10.8	16.0	16.1	15.9	16.0
7	12.1	15.3	16.1	15.7	15.9	15.6	16.1	16.2	14.7	15.9
8	-	-	-	-	-	-	-	-	-	-
9	15.9	14.5	15.2	12.9	14.8	15.5	16.0	16.2	15.9	15.7
10	15.9	15.8	15.5	15.6	15.5	15.7	15.5	-	-	15.6

EFG										
No	Sub-cell Efficiency (%)									Avg♮ (%)
1	-	13.9	-	14.7	13.6	14.6	15.3	14.0	15.3	14.5
2	15.0	15.6	15.2	14.9	15.3	15.3	15.2	13.6	15.5	15.2
3	15.0	14.9	9.9	15.1	14.6	14.8	14.9	14.6	14.8	14.8
4	14.9	14.7	15.0	14.8	14.7	15.3	15.1	15.1	15.4	15.0
5	14.7	-	-	14.7	-	13.4	15.0	14.8	10.8	13.9
6	15.1	15.3	14.3	11.9	15.0	15.1	15.2	11.4	14.3	15.0
7*	-	-	-	-	-	-	-	-	-	-
8	15.3	15.7	-	15.2	15.3	-	12.1	-	-	15.4
9	-	-	-	-	-	-	-	-	-	-
10	14.6	15.2	14.5	15.2	15.4	14.8	14.7	14.2	15.0	14.9

Note: "-" efficiency is not available.

♮ Efficiency lower than 14.5% not count

∗ EFG 7 was broken.

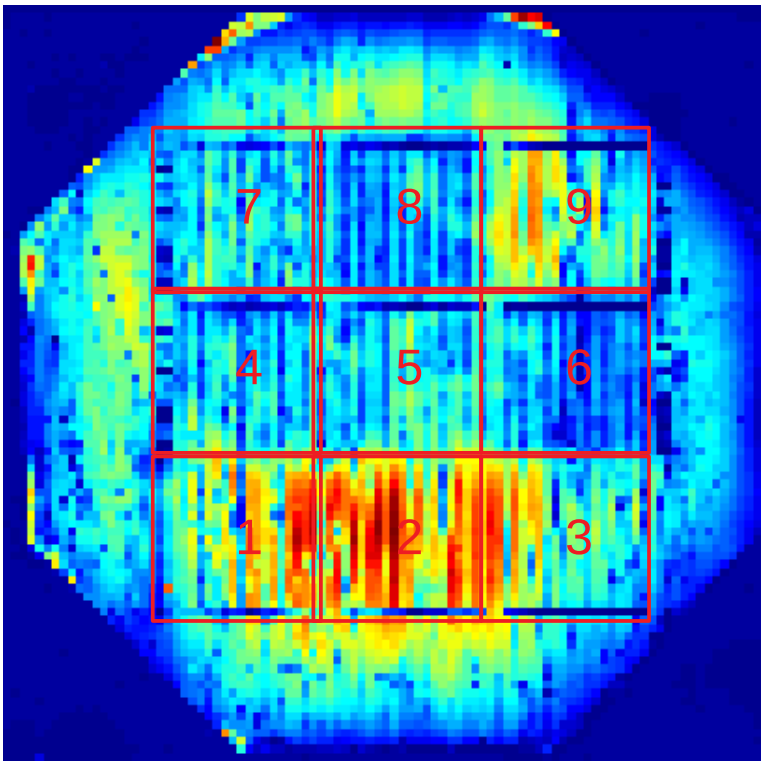

Figure 90: The PL image of a photovoltaic cell, the red squares show the position of the sub-cells

the figures. This correlation is also observed in the fit despite few exceptions, e.g. CAST 2, 5 and EFG 2, 10 for residual stress, EFG 6 for PL. More consistent correlation in the PL and efficiency was observed, while a positive trend in the residual stress and efficiency is obvious.

7.7 Conclusions

The magnitude of residual stress in EFG and ribbon samples is considerably higher than that in CZ and cast samples. The evolution of residual stresses and lifetime during processing was monitored. A correlation between the residual stress, PL and efficiency was found. The areas with high residual stress are correlated to those with high lifetime and high efficiency.

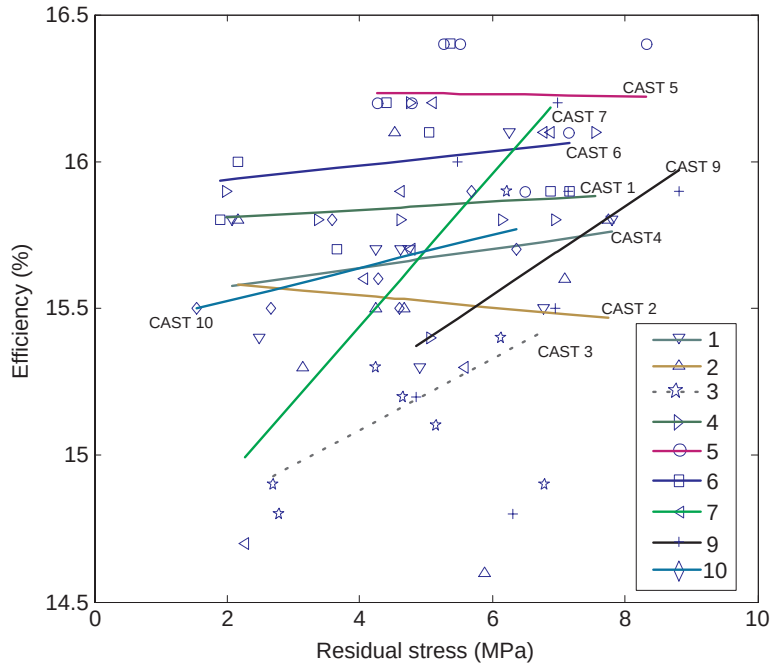

Figure 91: The correlation between the residual stress and efficiency for CAST silicon

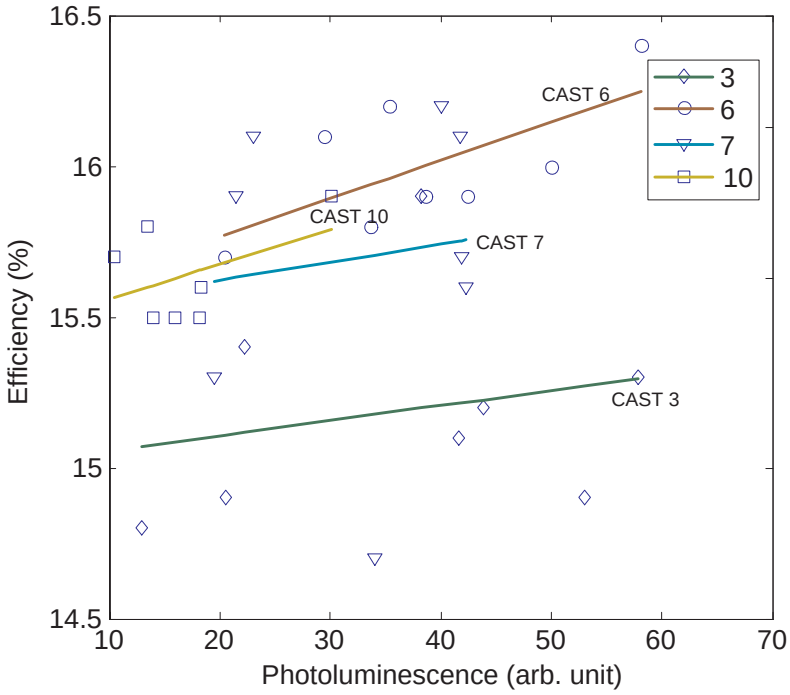

Figure 92: The correlation between the PL and efficiency for CAST silicon

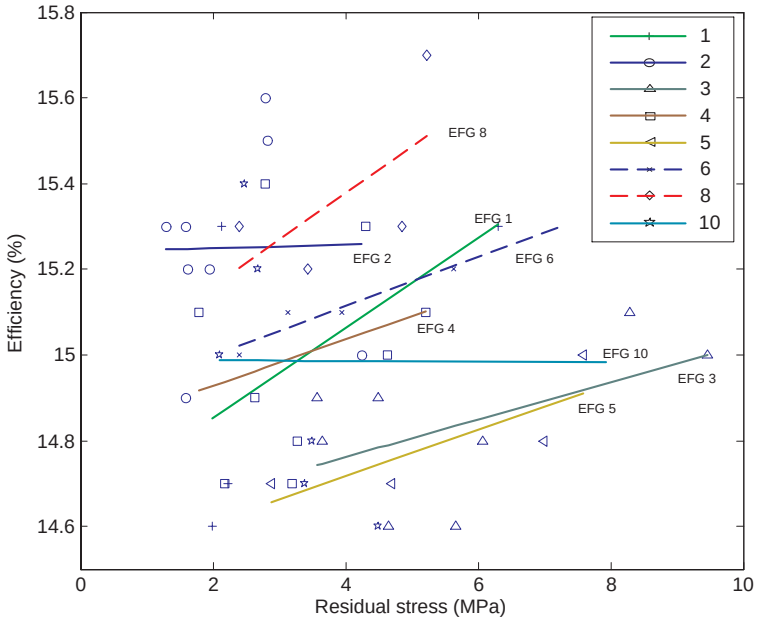

Figure 93: The correlation between the residual stress and efficiency for CAST silicon

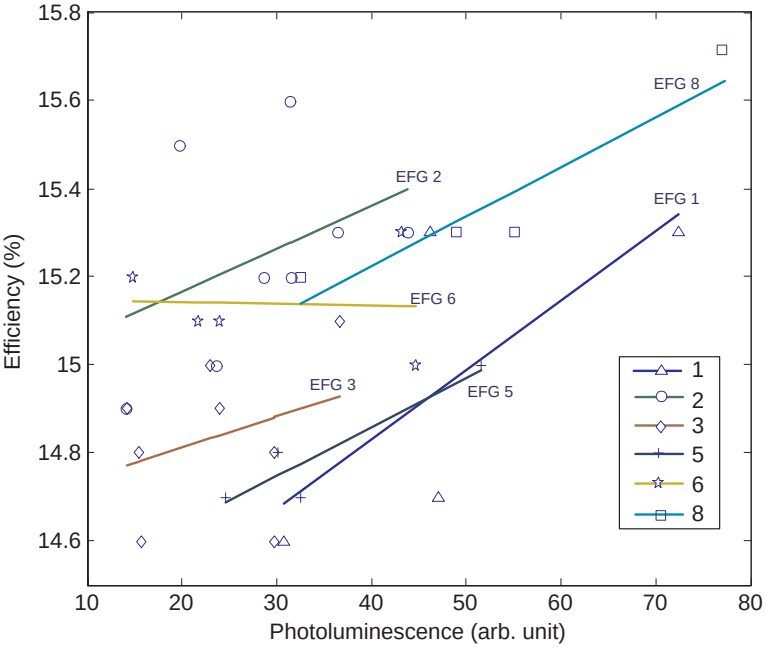

Figure 94: The correlation between the PL and efficiency for CAST silicon

CHAPTER VIII

CONCLUSIONS

The conclusions of this thesis may be summarized as follow:

1. The loss in light intensity and spatial resolution of the fringe multiplier was analyzed. An arrange was introduced to minimized the loss in spatial resolution in the four-point bending was introduced. The fringe multiplier was calibrated.

2. The phase-stepping technique was discussed. A new formula was introduced to extend the range of the isoclinics from $\left[-\frac{\pi}{4}, \frac{\pi}{4}\right]$ to $\left[-\frac{\pi}{2}, \frac{\pi}{2}\right]$, and retardation from $[0, \pi]$ to $[0, 2\pi]$, and eliminated the possibility of phase unwrapping of the residual stresses.

3. The systematic and random errors caused by the angular misalignment of the two waveplates, the analyzer and the image digitization were analyzed. The error in the isoclinic angle can be ignored except in the undefined regions, and the maximum error in stress is within 1.2 MPa.

4. The anisotropic stress-optic coefficient of the (001), (011) and (111) single crystal silicon is derived and calibrated using four-point bending, the coefficient of the (001) silicon was obtained as,

$$C_{(001)}(\theta) = C_{(011)}(\theta) = \frac{n_0^3}{2} \frac{1}{\sqrt{\frac{\sin^2 2\theta}{\pi_{44}^2} + \frac{\cos^2 2\theta}{(\pi_{11}-\pi_{12})^2}}}$$

   and the (111) silicon,

$$C_{(111)}(\theta) = \frac{n_0^3}{2} \frac{\pi_{11} - \pi_{12} + 2\pi_{44}}{3}$$

   The components of the stress-optic tensor were measured to be: $\pi_{11} - \pi_{12} = 9.88 \times 10^{-13}$ Pa^{-1}, $\pi_{44} = 6.50 \times 10^{-13}$ Pa^{-1}.

5. The stress-optic coefficients of the EFG and CAST silicon were calibrated. The coefficient of EFG silicon has the same profile as that of (001) CZ silicon with a magnitude

of 1.7 times bigger.

6. The pattern and statistical characteristics in the distribution of residual stresses were analyzed. The orientation of the residual stress of string ribbon and EFG silicon was found to be likely aligned along the crystal growth direction.

7. The residual stresses in EFG and string ribbon silicon have a high variation in spatial distribution. The average residual stress was found to be around 10 MPa, and the maximum 30 MPa.

8. The residual stresses in cast and CZ silicon are relatively uniform. The average residual stress was found to be around 5 MPa, and the maximum 15 MPa.

9. A spatial correlation between the residual stress, PL and efficiency was found for cast and EFG silicon. The areas with high residual stress are correlated to those with high lifetime and high efficiency.

10. The evolution of the residual stresses and photoluminescence of four major types of silicon was investigated in cell processing. The effects of phosphorus gettering, surface passivation and metal contact on the lifetime were observed.

REFERENCES

[1] R. L. Wallace, J. I. Hanoka, A. Rohatgi, and G. Crotty. Thin silicon string ribbon. *Solar Energy Materials and Solar Cells*, 48(1-4):179–186, 1997.

[2] L. C. Garone, C. V. Hari Rao, A. D. Morrison, T. Surek, and K. V. Ravi. Orientation dependence of defect structure in efg silicon ribbons. *Applied Physics Letters*, 29(8):511, 1976.

[3] Tieyu Zheng. *A Study of Residual Stresses in Thin Anisotropic (silicon) Plates*. Ph.d thesis, Georgia Institute of Technology, 2000.

[4] J. P. Kalejs. Modeling contributions in commercialization of silicon ribbon growth from the melt. *Journal of Crystal Growth*, 230(1-2):10–21, 2001.

[5] B. Chalmers. High-speed growth of sheet crystals. *Journal of Crystal Growth*, 70(1-2):3–10, 1984.

[6] C. H. Wu and J. C. Lambropoulos. Thermoelastic analysis of dislocation generation during edge-defined film-fed growth of polygonal shells. *Journal of Crystal Growth*, 155(1-2):38–46, 1995.

[7] J. P. Kalejs, B. H. Mackintosh, and T. Surek. High-speed efg of wide silicon ribbon. *Journal of Crystal Growth*, 50(1):175–192, 1980.

[8] J. C. Lambropoulos, J. W. Hutchinson, R. O. Bell, B. Chalmers, and J. P. Kalejs. Plastic-deformation influence on stress generated during silicon sheet growth at high speeds. *Journal of Crystal Growth*, 65(1-3):324–330, 1983.

[9] R. G. Seidensticker and R. H. Hopkins. Silicon ribbon growth by the dendritic web process. *Journal of Crystal Growth*, 50(1):221–235, 1980.

[10] K. Ramesh and S.K. Mangal. Data acquisition techniques in digital photoelasticity: a review. *Optics and lasers in engineering*, 30:53–75, 1998.

[11] E. A. Patterson. Digital photoelasticity: principles, practices and potential. *Strain*, 38:27–39, 2002.

[12] P. Doig and P.E.J. Flewitt. Non-destructive stress measurement using x-ray diffraction methods. *NDT International*, 11(3):127–131, 1978.

[13] S. Shin and H. Yano. Evaluation of error of x-ray residual stress measurement method. In Japan Soc. Instrum. & Control Eng, Tokyo, editor, *Recent Advances in Weighing Technology and Force Measurement. 10th International Conference of the IMEKO Technical Committee TC-3 on Measurement of Force and Mass*, Kobe, Japan, 1984.

[14] A. S. M. Y. Munsi, A. J. Waddell, and C. A. Walker. A method for determining x-ray elastic constants for the measurement of residual stress. *Strain*, 39(1):3–10, 2003.

[15] K. Y. Kim and W. Sachse. The theory of thermodynamic-acoustoelastic stress gauge. *Journal of Applied Physics*, 80(9):4934–4943, 1996.

[16] H. R. Dorfi, H. R. Busby, and M. Janssen. Acoustoelasticity: Ultrasonic stress field reconstruction. *Experimental Mechanics*, 36(4):325–332, 1996.

[17] A. T. Andonian and S. Danyluk. Non-destructive determination of residual-stresses in circular silicon-wafers. *Mechanics Research Communications*, 11(2):97–104, 1984.

[18] A. T. Andonian and S. Danyluk. Residual-stresses of thin, short rectangular-plates. *Journal of Materials Science*, 20(12):4459–4464, 1985.

[19] K. Ghaffari, B. Wang, S. Danyluk, M. Billone, and G. Pharr. Optical interferometric determination of in-plane residual stresses in sio2 films on silicon substrates. *Materials Evaluation*, 54(10):1167–1170, 1996.

[20] Y. Kwon, S. Danyluk, L. Bucciarelli, and J. P. Kalejs. Residual-stress measurement in silicon sheet by shadow moire interferometry. *Journal of Crystal Growth*, 82(1-2):221–227, 1987.

[21] H. W. Park and S. Danyluk. Residual-stress measurement in filament-evaporated aluminum films on single-crystal silicon-wafers. *Journal of Materials Science*, 26(1):23–27, 1991.

[22] David Brewster. On the communication of the structure of doubly refracting crystals to glass, muriate of soda, flour spar and other substances by mechanical compression and dilatation. *Philosophical Transactions of the Royal Society*, pages 156–178, 1816.

[23] E.G. Coker and L.N.G. Filon. *A Treatise on Photoelasticity*. Cambridge University Press, 1931.

[24] K. Ramesh. *Digital Photoelasticity Advanced Techniques and Applications*. Springer, 2000.

[25] A. J. Durelli and W. F. Riley. *Introduction to Photomechanics*. Prentice-Hall Inc., Englewood Cliffs, N.J., 1965.

[26] Daniel Post. Isochromatic fringe sharpening and fringe multiplication in photoelasticity. *Proc SESA*, XII(2):143–156, 1955.

[27] Daniel Post. Photoelastic-fringe multiplication-for tenfold increase in sensitivity. *Experimental Mechanics*, 10:305–312, 1970.

[28] A. F. C Brown and V. M. Hickson. Improvements in photoelastic technique obtained by the use of a photometric method. *British Journal of Applied Physics*, 1(2):39–44, 1950.

[29] M. M. Frocht, H Pih, and Landsberg D. The use of photometric devices in the solution of the general three-dimensional photoelastic problem. *Proc SESA*, 12(1):181–190, 1954.

[30] R. K. Muller and L. R. Saackel. Complete automatic-analysis of photo-elastic fringes. *Experimental Mechanics*, 19(7):245–251, 1979.

[31] Y. Seguchi, Y. Tomita, and M. Watanabe. Computer-aided fringe-pattern analyzer - case of photo-elastic fringe. *Experimental Mechanics*, 19(10):362–370, 1979.

[32] A. S. Voloshin and C. P. Burger. Half-fringe photoelasticity: A new approach to whole-filed stress analysis. *Experimental Mechanics*, 23(3):304–313, 1983.

[33] F. W. Hecker and B. Morche. Computer-aided measurement of relative retardations in plane photoelalsticity. *Experimental Stress Analysis*, pages 535–543, 1986.

[34] E. A. Patterson and Z. F. Wang. Towards full field automated photoelastic analysis of complex components. *Strain*, 27:49, 1991.

[35] E. A. Patterson. Automated photoelastic analysis. *Strain*, 24(1):15, 1988.

[36] E. A. Patterson, W. Ji, and Z. F. Wang. On image analysis for birefringence measurements in photoelasticity. *Optics and Lasers in Engineering*, 28(1):17–36, 1997.

[37] E. A. Patterson and Z. F. Wang. Simulatneous observation of phase-stepped images for automated photoelasticity. *Journal of Strain Analysis*, 33(1):1–15, 1997.

[38] J. Carazo-Alvarez, S. J. Haake, and E. A. Patterson. Completely automated photoelastic fringe analysis. *Optics and Lasers in Engineering*, 21:133–149, 1994.

[39] S. J. Haake, Z. F. Wang, and E. A. Patterson. Evaluation of full field automated photoelastic analysis based on phase stepping. *Experimental Techniques*, pages 19–25, 1993.

[40] W. Ji and E. A. Patterson. Simulation of errors in automated photoelasticity. *Experimental Mechanics*, 38(2):132–139, 1998.

[41] Z. F. Wang and E. A. Patterson. Using of phase-stepping with demodulation and fuzzy sets for birefringence measurement. *Optics and Lasers in Engineering*, 22:91–104, 1995.

[42] C. Buckberry and D. Towers. New approaches to the full-field analysis of photoelastic stress patterns. *Optics and Lasers in Engineering*, 24:415–428, 1996.

[43] Andrew D. Nurse. Full-field automated photoelasticity by use of a three-wavelength approach to phase stepping. *Applied Optics*, 36(23):5781–5786, 1997.

[44] M. J. Ekman and A. D. Nurse. Absolute determination of the isochromatic parameter by load-stepping photoelasticity. *Experimental Mechanics*, 38(3):189–195, 1998.

[45] K. Ramesh and D. K. Tamrakar. Improved determination of retardation in digital photoelasticity by load stepping. *Optics and Lasers in Engineering*, 33(6):387–400, 2000.

[46] Liu Tong, Chai Gin Boay, and Anand Asundi. Novel full-field automated photoelastic analysis technique. *Opt. Eng.*, 39(10):2689–2695, 2000.

[47] A. S. Redner. Photoelastic measurements by means of computer-assisted spectral-contents analysis. *Experimental Mechanics*, 1985.

[48] A. S. Voloshin and A. S. Redner. Automated measurement of birefringence: Development and experimental evaluation of the techniques. *Experimental Mechanics*, pages 252–257, 1989.

[49] S. J. Haake and E. A. Patterson. Photoelastic analysis of frozen stressed specimens using spectral-contents analysis. *Experimental Mechanics*, 32(3):266–272, 1992.

[50] A. Ajovalasit, S. Barone, and G. Petrucci. Towards rgb photoelasticity: full-field automated photoelasticity in white light. *Experimental Mechanics*, pages 193–199, 1995.

[51] K. Ramesh and S. S. Deshmukh. Three fringe photoelasticity - use of colour image processing hardware to automate ordering of isochromatics. *Strain*, 32(3):79–86, 1996.

[52] C. Quan, P. J. Bryanston-Cross, and T. R. Judge. Photoelasticity stress analysis using carrier fringe and fft techniques. *Optics and Lasers in Engineering*, 18:79–108, 1993.

[53] W.J. Bond and J. Andrus. Photographs of the stress field around edge dislocations. *Physical Review*, 101(3):1211–1212, 1956.

[54] A. A. Giardini. Piezobirefringence in silicon. *The American mineralogist*, 43:249–263, 1958.

[55] S.R. Lederhandler. Infrared studies of birefringence in silicon. *Journal of applied physics*, 30(11):1631–38, 1959.

[56] R. O. Denicola and R. N. Tauber. Effect of growth parameters on residual stress and dislocation density of czochralski-grown silicon crystals. *Journal of Applied Physics*, 42(11):4262, 1971.

[57] H. Kotake and Shin. Takasu. Quantitative measurement of stress in silicon by photoelasticity and its application. *J. Electrochem. Soc.*, 127(1):179–184, 1980.

[58] S. P. Wong, W.Y. Cheung, M.R.Sajan N.Ke, W.S.Guo, L.Huang, and Shounan Zhao. Ir photoelasticity study of stress distribution in silicon under thin film structures. *Materials Chemistry and Physics*, 51:157–162, 1997.

[59] R. W. Dixon. Photoelasticity properties of selected materials and their relevance for applications to acoustic light modulators and scanners. *Journal of Applied Physics*, 38(13):5149–5153, 1967.

[60] H. Kotake, K. Hirahara, and M. Watanabe. Quantitative photoelastic measurement of residual stress in lec grown gap crystals. *Journal of crystal growth*, 50:743–751, 1980.

[61] Tieyu Zheng and Steven Danyluk. Study of stresses in thin silicon wafers with near-infrared phase stepping photoelasticity. *J. Mater. Res*, 17(1):36–42, 2002.

[62] Tieyu Zheng and S. Danyluk. Nondestructive measurement of in plane residual stresses in thin silicon substrates by infrared transmission. *Materials Evaluation*, 59(10):1227–1233, 2001.

[63] V. G. Gorshkov, Y. K. Danileiko, V. V. Osiko, A. V. Sidorin, N. V. Veselovskaya, Y. V. Dankovskii, and B. L. Shklyar. Mechanical microstresses in dislocation-free floating-zone silicon monocrystals. *Physica Status Solidi a-Applied Research*, 106(2):363–369, 1988.

[64] H. D. Geiler, M. Wagner, H. Karge, M. Paulsen, and R. Schmolke. Photoelastic stress evaluation and defect monitoring in 300-mm-wafer manufacturing. *Materials Science in Semiconductor Processing*, 5(4-5):445–455, 2002.

[65] M. Yamada. Quantitative photoelastic measurement of residual strains in undoped semi-insulating gallium arsenide. *Appl. Phys. Lett.*, 47(4):365–367, 1985.

[66] T. Iwaki and T. Koizumi. Stress-optic law in a single crystal and its application to photo-anisotropic elasticity. *Experimental Mechanics*, 29(3):295–299, 1989.

[67] H. C. Liang, Y. X. Pan, S. N. Zhao, G. M. Qin, and K. K. Chin. Two-dimensional state of stress in a silicon wafer. *Journal of Applied Physics*, 71(6):2863–2870, 1992.

[68] P. S. Theocaris. *Matrix theory of photoelasticity*. Springer-Verlag, New York, 1979.

[69] J. F. Nye. *Physical properties of crystals*. Oxford, 1957.

[70] N. E. Dowling. *Mechanical behavior of materials*. Prentice Hall, 1998.

[71] S. Ostapenko, I Tarasov, J.P. Kalejs, and C. Haessler E-U Reisner. Defect monitoring using scanning photoluminescence spectroscoy in multicrystalline silicon wafers. *Semicond. Sci. Tecnol.*, 15:840–848, 2000.

[72] S. Ostapenko, A.U. Savchuk, G. Nowak, J. Lagowski, and L. Jastrzebski. Photoluminescence defect diagnostics in poly-si thin films. *Materials Science Forum*, 196-201(pt 4):1897–1902, 1995.

VITA

Shijiang He was born in Anqing, China on June 15, 1970. He got his degree of Bachelor of Science and Master of Engineering in Engineering Mechanics at Tsinghua University in Beijing, China in 1993 and 1996 respectively, and Master of Science in Electrical Engineering at Georgia Institute of Technology in 2004. He worked on mechanical design at the SINOPEC Beijing Design Institute of China for four years beginning in 1996. He plans to conduct the research in applied mechanics in design and manufacturing of microelectronic devices.